



**HAL**  
open science

## Surface uplift and topographic rejuvenation of a tectonically inactive range: Insights from the Anti-Atlas and the Siroua Massif (Morocco)

R. Clementucci, P. Ballato, Lionel Siame, M. Fox, R. Lanari, A. Sembroni, C. Faccenna, A. Yaaqoub, A. Essaifi

### ► To cite this version:

R. Clementucci, P. Ballato, Lionel Siame, M. Fox, R. Lanari, et al.. Surface uplift and topographic rejuvenation of a tectonically inactive range: Insights from the Anti-Atlas and the Siroua Massif (Morocco). *Tectonics*, 2023, 42 (2), pp.e2022TC007383. 10.1029/2022TC007383 . hal-03966926

**HAL Id: hal-03966926**

**<https://hal.science/hal-03966926v1>**

Submitted on 1 Feb 2023

**HAL** is a multi-disciplinary open access archive for the deposit and dissemination of scientific research documents, whether they are published or not. The documents may come from teaching and research institutions in France or abroad, or from public or private research centers.

L'archive ouverte pluridisciplinaire **HAL**, est destinée au dépôt et à la diffusion de documents scientifiques de niveau recherche, publiés ou non, émanant des établissements d'enseignement et de recherche français ou étrangers, des laboratoires publics ou privés.

1 Surface uplift and topographic rejuvenation of a tectonically inactive range: Insights  
2 from the Anti-Atlas and the Siroua Massif (Morocco)

3 Clementucci R.<sup>1,2\*</sup>, Ballato P.<sup>1</sup>, Siame L.<sup>2</sup>, Fox M.<sup>3</sup>, Lanari R.<sup>1,4</sup>, Sembroni A.<sup>1</sup>, Faccenna C.<sup>1,5</sup>,  
4 Yaaqoub A.<sup>6</sup>, Essaifi A.<sup>6</sup>

5 <sup>1</sup> *Dipartimento di Scienze, Università Roma Tre, Largo San Leonardo Murialdo 1, 00146 Rome, Italy.*

6 <sup>2</sup> *Aix-Marseille Univ., CNRS, IRD, INRAE, Collège de France, CEREGE, Aix-en Provence, France.*

7 <sup>3</sup> *Department of Earth Sciences, University College London, Gower Street, London, WC1E 6BT, United  
8 Kingdom.*

9 <sup>4</sup> *Dipartimento di scienze, Università di Firenze, Italia.*

10 <sup>5</sup> *GFZ-German Research Centre for Geosciences, Potsdam, Germany.*

11 <sup>6</sup> *Département de Géologie, FSSM, B.P. 2390, Université' Cadi Ayyad, Marrakech, Morocco.*

12 *Corresponding author: [romano.clementucci@uniroma3.it](mailto:romano.clementucci@uniroma3.it)*

13

14 **Key Points:**

- 15 - The transient state of the stream network and the high-standing erosional surface document a  
16 recent phase of topographic rejuvenation  
17 - Uplift started at ~14-10 Ma and increases from the western (0.5 km) to the central Anti-Atlas  
18 (1.1 km) and the Siroua Massif (1.5 km)  
19 - Regional surface uplift is most likely due to asthenospheric upwelling, locally combined  
20 (Siroua Massif) with magma injection and faulting

21

22 **Abstract**

23 The Atlas-Meseta intracontinental orographic system of Morocco experienced recent, large-scale  
24 surface uplift as documented by elevated late Miocene, shallow-water marine deposits exposed in the  
25 Middle Atlas Mountains. The Anti-Atlas Mountains do not present any stratigraphic records that  
26 document regional vertical movements, however, the presence of a high-standing, erosional surface,  
27 and the transient state of the river network, provides insights into the uplift history of the belt and the  
28 mechanisms that drove it. Here, we combine geomorphic and stream profiles analyses, celerity of  
29 knickpoints and linear inverse landscape modelling with available geological evidence, to decipher  
30 the spatial and temporal variations of surface uplift in the Anti-Atlas and the Siroua Massif. Our  
31 results highlight the presence of a transient landscape and document a long wave-length topographic  
32 swell (~ 100 x 600 km) with a maximum surface uplift of ~1500 m in the Siroua Massif and ~1100

33 m in the central Anti-Atlas most likely starting from ~14-10 Ma. Surface uplift occurred in association  
34 with the onset of late Miocene magmatism in the Siroua and Saghro Massif and contractional  
35 deformation in the High Atlas. Regional surface uplift was most likely due to deep-seated mechanism,  
36 such as asthenospheric upwelling. Additional processes such as magma injection and faulting  
37 contributed to the surface uplift of the Siroua Massif. Overall, our approach allows to quantitatively  
38 constrain the transient state of the landscape and the contribution of regional surface uplift on  
39 mountain building processes.

40

## 41 **1. Introduction**

42 The interplay between exogenic and endogenic processes controls the growth and decay of  
43 topography over diverse temporal and spatial scales. Topographic development is generated by  
44 different mechanisms, such as crustal shortening and thickening, magmatic addition, flexural  
45 rebound, and asthenospheric flow, where each process is associated with a typical wavelength ( $10^{-1}$   
46 to  $10^3$  km) and amplitude (10 to  $10^3$  m; *e.g.*, England and Molnar, 1990; De Celles et al., 2009;  
47 Roberts and White, 2010; Faccenna and Becker, 2020). Topographic decay results from geomorphic  
48 erosion, which is primarily controlled by climate, topographic gradients, and rock strength (*i.e.*,  
49 Jansen et al., 2010; Scharf et al., 2013; Clementucci et al., 2022). When topographic decay prevails,  
50 extensive low-gradient, low-topographic relief landscapes may form (Baldwin et al., 2003; Tucker  
51 and van der Beek, 2013). These geomorphic low-relief features can be also found at the summit of  
52 mountains areas (Miller et al., 2013; West et al., 2013; Calvet et al., 2015), where they have been  
53 interpreted to have formed either in situ at high elevation (*e.g.*, Yang et al., 2015; Fox et al., 2020),  
54 or to be part of a less elevated and extensive low-relief landscape that has undergone recent surface  
55 uplift (*e.g.*, Calvet et al., 2015; Olivetti et al., 2012; 2016; Whipple et al., 2017). In the case of surface  
56 uplift, such elevated paleo-topography, named relict landscape or paleo-surface, represents a transient  
57 geomorphic marker that provides a reference frame for quantifying the spatial distribution of surface  
58 uplift (Calvet et al., 2015; Fox, 2019). Thus, relict landscapes represent a unique opportunity to

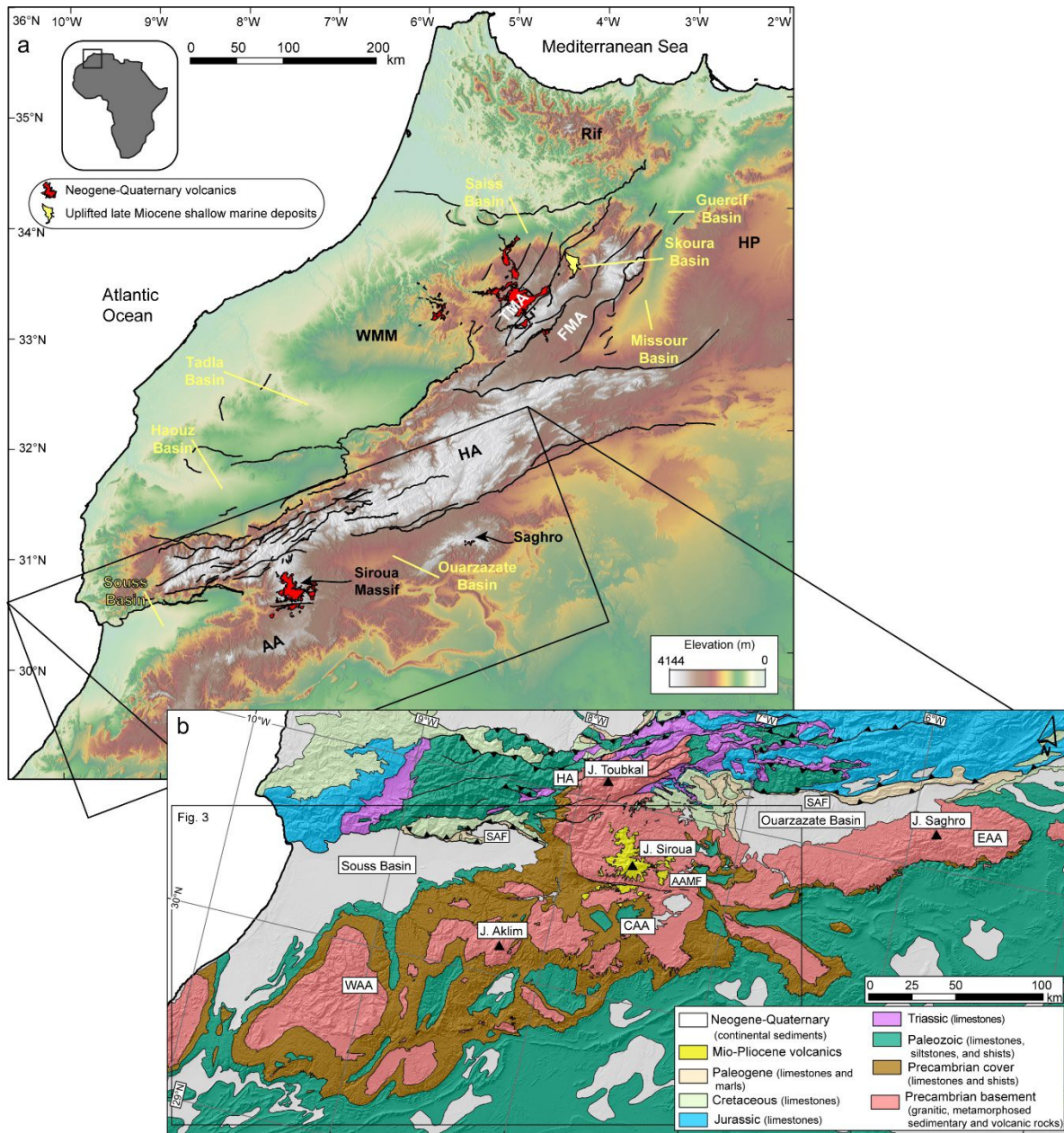
59 decipher the wavelength and the amplitude of surface uplift, and consequently the mechanisms that  
60 created such a topography, especially in areas devoid of stratigraphic constraints.

61 The Atlas-Meseta intracontinental orographic system of Morocco is composed of different morpho-  
62 structural domains that from north to south include: the Moroccan Meseta (Western Meseta and  
63 Eastern High Plateaus), the Middle Atlas, the High Atlas, the Siroua Massif, and the Anti-Atlas  
64 (Figure 1a). The High and Middle Atlas are the main active orogen (*e.g.*, Sebrier et al., 2006), while  
65 the other regions are characterized by a relatively high topography that formed without significant  
66 crustal deformation (Teixell et al., 2003; Frizon de Lamotte et al., 2009; Pastor et al., 2015). This  
67 configuration offers the opportunity to investigate rates, wavelength, magnitudes and causes of large-  
68 scale topographic growth.

69 In this study, we focus on the Anti-Atlas Mountains, a Variscan orogen characterized by a complex  
70 assemblage of intrusive, metamorphic, and sedimentary rocks. Similarly to the Appalachian, which  
71 represent the American counterpart of the Variscan orogens in Africa and Europe, the topography of  
72 the Anti-Atlas consists of a wide relict landscape composed of high-standing erosional surfaces  
73 mostly sculptured on basement rocks (Choubert, 1952; Malusà et al., 2007; Guimera et al., 2011;  
74 Clementucci et al., 2022). This basement has been slowly eroding at few tens of meters per million  
75 years since the latest Cretaceous as documented by low-temperature thermochronology (Lanari et al.,  
76 2020a; Clementucci et al., 2022). Overall, the occurrence of such a low-relief features at the  
77 maximum topography together with the lack of Cenozoic deformation, supports the idea that the Anti-  
78 Atlas experienced a relatively recent phase of surface uplift (Missenard et al., 2006). The causes of  
79 this topographic rejuvenation, however, are still poorly understood. Some authors suggested that  
80 uplift may be related to Cenozoic shortening (Giumera et al., 2011), whereas others proposed the  
81 occurrence of deep dynamic processes (Missenard et al., 2006; Sebrier et al., 2006; Frizon de Lamotte  
82 et al., 2009). In this context, the absence of tectonic activity, the steady protracted low denudation  
83 rates, and the occurrence of an elevated relict landscape offer the possibility to quantify the regional

84 surface uplift in the Anti-Atlas and the Siroua Massif and to investigate possible causal uplift  
85 mechanisms.

86 To achieve these goals, we combined quantitative analysis of regional and basin-scale topography  
87 with stream profiles analysis (knickpoints characterization, longitudinal profiles and  $\chi$ - $z$  plot) and  
88 recently published basin-wide denudation rates inferred from  $^{10}\text{Be}$  concentrations (Clementucci et al.,  
89 2022). Furthermore, we performed stream projections from the upper relict channel profiles and  
90 reconstructed the paleo-landscape to constrain the amount of relative base level fall following the  
91 increase in Cenozoic rock uplift rates. Finally, we constrained the timing of this geomorphic  
92 rejuvenation to the middle-late Miocene by applying a knickpoints celerity model. This approach  
93 provides a framework for discussing the contribution of large-scale, deep signals and shallower  
94 processes in generating the regional topographic relief in areas where large wavelength uplift occurs.  
95



96

97 **Figure 1.** (a) Topographic map of the Atlas-Meseta orographic system and his morpho-structural domains.  
 98 FMA: Folded Middle Atlas. TMA: Tabular Middle Atlas. HP: High Plateaus. WMM: Western Moroccan  
 99 Meseta. AA : Anti-Atlas. HA : High Atlas. (b) Simplified geological map of High and Anti-Atlas Mountains  
 100 based on the 1:1.000.000 geological map of Morocco (modified from Maroc Service Géologique, 1985). EAA:  
 101 Eastern Anti-Atlas, CAA: Central Anti-Atlas, WAA: Western Anti-Atlas, AAMF: Anti-Atlas Major Fault,  
 102 SAF: South Atlas Fault. The main faults and mountain peaks are shown with black lines and triangles,  
 103 respectively. The black lines with triangles indicate the thrust faults.

104

105

106

107

108 **2. Geological background**

## 109            2.1     **Geological setting**

110     The intracontinental Atlas-Meseta orographic system of Morocco is composed of two WSW-ENE  
111     oriented mountain belts, the High Atlas (HA) and the Anti-Atlas (AA), and two elevated regions with  
112     low-topographic relief, named Western and Eastern (or High Plateaus) Meseta, which are separated  
113     by the SW-NE striking Middle Atlas belt (Figure 1a, TMA and FMA). This system of mountain belts  
114     experienced a complex geologic history including multiple episodes of contractional deformation and  
115     rifting (Froitzheim et al., 1988; Hafid, 2000; Frizon de Lamotte et al. 2000; Domènech et al., 2015).  
116     Currently, active deformation is controlled by the plate convergence between Africa and Eurasia  
117     (Froitzheim et al., 1988; Hafid, 2000; Frizon de Lamotte et al. 2000; Gomez et al. 2000; Teixell et  
118     al., 2003; Lanari et al., 2020b).

119     With a few mountain peaks above 4 km of elevation, the HA is the highest domain of the Atlas system  
120     that strikes for approximately 600 km over a width of 50 to 100 km. The HA consists of a fold and  
121     thrust belt composed of Precambrian, Paleozoic, and Mesozoic rocks (Figure 1). Mesozoic rocks  
122     include mostly syn-rift (Jurassic and Triassic) and post-rift deposits (Cretaceous), related to the  
123     opening of a rift basin developed during the breakup of Africa (Arboleya et al., 2004; Baudon et al.,  
124     2009; Lanari et al., 2020b). Based on thermochronological and structural data the main exhumation  
125     episode started in the middle/late Miocene and led to 4-6 km of exhumation (Balestrieri et al., 2009;  
126     Barbero et al., 2007; Domènech, 2015; 2016; Ghorbal, 2009; Lanari et al., 2020a; 2020b; Leprêtre et  
127     al., 2018; Missenard et al., 2008).

128     The HA and AA belts are separated by the Souss and the Ouarzazate basins, which have been  
129     commonly interpreted as the southern Neogene foreland basins of the HA (Figure 1; Sebrier et al.,  
130     2006; Arboleya et al., 2008). The Souss Basin has an eastward wedging geometry and is characterized  
131     by a longitudinal, E-W oriented, drainage system flowing directly into the Atlantic Ocean (Figure  
132     2a). The basin extends for a length of more than 150 km and has a rather flat, low-topographic relief  
133     morphology that increases progressively toward the basin interior up to ~700 m of elevation. The

134 basin fill includes Pliocene to Quaternary fluvial, fluvio-lacustrine and aeolian sediments derived  
135 from the adjacent uplifting HA and AA belts (Hssaine and Bridgland, 2009).

136 The Ouarzazate Basin lies between 1200 and 1800 m of elevation and extends over a length of more  
137 than 150 km (Figure 1). The basin filling consists of a <1-km-thick-succession including Middle  
138 Eocene marine deposits unconformably overlain by Mio-Pliocene terrestrial sediments marking the  
139 development of endorheic conditions (Fraissinet et al. 1988; Gorler et al. 1988; El Harfi et al., 2001;  
140 Teson and Teixell 2006; Teson et al., 2010). The basin is currently drained by the Draa River a  
141 southward draining system that crosses the AA through a narrow bedrock gorge and then flows  
142 parallel to the AA before entering in the Atlantic Ocean (Figure 2a). The transition from endorheic to  
143 exoreic conditions most likely occurred in the Plio-Pleistocene, either through regressive erosion from  
144 the southern AA flank (Stablein, 1988) or lake overspill (Arboleya et al., 2008).

145 The Siroua Massif represents a strato-volcano covering an area of approximately of 500 km<sup>2</sup> and  
146 reaching maximum elevation of ~3300 m. Here, the Mio-Pliocene volcanic deposits directly overlie  
147 the Precambrian basement, which is characterized by an elongated, dome-like morphology with a  
148 low-topographic relief landscape (Missenard et al., 2008; Giumera et al. 2011).

149 The AA belt extends over approximately 600 km of length, has a width of 100 to 150 km, and rises  
150 ~2 km above sea level. The orogen was built through a series of collisional events starting from the  
151 Eburnean orogeny at around 2000 Ma (Ait Malek et al., 1998; Thomas et al., 2002; Walsh et al.,  
152 2002). Afterward, it experienced two main orogenic events: the Neoproterozoic Pan-African orogeny  
153 (Leblanc, 1975; Hefferan et al., 2000; Gasquet et al., 2008) with a subsequent extensional event  
154 during the Late Neoproterozoic (Piqué et al., 1999; Soulimani et al., 2003) and the late Carboniferous  
155 Variscan orogeny (Sebti et al., 2009; Soulimani et al., 2014; Sehart et al., 2018). Low-temperature  
156 thermochronology and stratigraphic data indicate that the AA was not subjected to major Mesozoic  
157 vertical movements, while denudation appears to have been rather uniform at rates of ~20 m/Myr  
158 since at least the late Cretaceous (Lanari et al., 2020a; Charton et al., 2021; Clementucci et al., 2022).

159 The basement is composed of magmatic, metamorphic, and sedimentary rocks assembled during the

160 Eburnean and Pan-African orogenesis. These rocks are widely exposed along the axial sectors of the  
161 range (Figures 1b and S1 in the supporting information) and are overlain by a late Precambrian and  
162 Paleozoic sedimentary sequence with a thickness of almost 10 km in the Western AA decreasing to  
163 less than 6 km in the eastern sectors of the belt (Piqué and Michard, 1989; Helg et al., 2004; Burkhard  
164 et al., 2006). This sedimentary cover was predominantly deposited in a shallow-water marine  
165 environment during the post Pan-African extensional event (Azizi Samir et al., 1990; Thomas et al.,  
166 2002; Soulaimani et al., 2003), and includes Lower Cambrian carbonates, siltstones, and marls as  
167 well as Middle Cambrian to Middle Devonian sandstones and shales. These strata were subsequently  
168 deformed during the Variscan orogeny and unconformably covered by marine (mainly Cretaceous)  
169 sediments (Figure 1a). The eastern Anti-Atlas includes another elevated (~2700 m) volcanic field, the  
170 Saghro Massif. (Figure 1a). This is composed of multiple late Miocene tuff cones which, likewise the  
171 Siroua Massif, overlie a wide erosional surface sculptured on the Precambrian basement.

172

## 173 **2.2 Geophysical and petrological data**

174 The peculiarity of the Atlas-Meseta orographic system is the lack of orogenic roots generated through  
175 crustal shortening and thickening processes that would isostatically support the modern topography.  
176 This applies to the HA (Beauchamp et al., 1999; Gomez et al., 2000; Teixell et al., 2003; Domènech  
177 et al., 2016; Fekkak et al., 2018; Lanari et al., 2020b) and the MA (Gomez et al., 1998; Arboleya et  
178 al., 2004; Pastor et al., 2015), where tectonic shortening has occurred during the Cenozoic, and to the  
179 tectonically inactive AA, Western and Eastern Meseta (Babault et al., 2008; Frizon de Lamotte et al.,  
180 2009; Pastor et al., 2015). Several geophysical and petrological studies indicate an anomalous  
181 thinning of the lithosphere with a shallow, hot asthenosphere beneath the entire Atlas-Meseta  
182 orographic system (El Azzouzi et al., 1999; Missenard et al., 2006; Duggen et al., 2009; Miller et al.,  
183 2015). This includes geophysical modelling of gravity data, S-received function (Ayarza et al., 2005;  
184 Missenard et al., 2006; Miller and Becker, 2014; Miller et al., 2015), heat flow measurements, deep  
185 electrical resistivity (Rimi et al., 1999; Zeyen et al., 2005) and seismic tomography (Seber et al.,

186 1996; Palomeras et al., 2014; Bezada et al., 2014). The shallow asthenosphere is thought to support  
187 the present-day topography of the Atlas-Meseta system, which should have been generated, at least  
188 in part, by deep-seated, mantle driven processes. For example, a maximum of 2000 m of residual  
189 topography has been estimated in the HA and MA considering a crustal thickness of ca. 35 km (Miller  
190 and Becker, 2014), while more than 1000 m of elevation has been attributed to dynamic topography  
191 (Frizon de Lamotte et al., 2009; Spieker et al., 2014).

192 Magmatic activity in the Siroua, Saghro and the MA Mountains presents an alkaline affinity  
193 indicating a partial melting of sublithospheric mantle caused by heating generated by asthenospheric  
194 flow (El Azzouzi et al., 1999; 2010; De Beer et al., 2000; Missenard et al., 2006). The geochemical  
195 signature and trace element patterns of the MA lavas are very similar to those observed in the Canary  
196 Islands, suggesting a possible link between the Canary mantle plume and continental intraplate  
197 volcanism in the Atlas-Meseta system (Duggen et al., 2009). Interestingly, magmatism occurred in  
198 two different pulses, in the Eocene and middle-late Miocene in association with renewed tectonic  
199 activity. A more recent phase of magmatism, however, has occurred in the MA and Western Meseta  
200 during the last 2 Ma, apparently without major acceleration in tectonic deformation (El Azzouzi et  
201 al., 2010; Missenard et al., 2012).

202

### 203 **3. Methods**

#### 204 **3.1. River profiles and knickpoints discretization**

205 River networks represent a powerful reconnaissance tool to investigate the impact of rock uplift and  
206 climate changes on landscape evolution (Hack, 1957; Kirby and Whipple, 2001; Wobus et al., 2006;  
207 Kirby and Whipple, 2012; Whittaker, 2012). This is possible because channel steepness and erosion  
208 rates along river profiles adjust to rock uplift, climatic conditions, and bedrock erodibility (Duvall et  
209 al., 2004; DiBiase and Whipple, 2011). Channel slopes along the stream commonly exhibit an inverse  
210 power-law scaling relationship with upstream contributing drainage area (Flint, 1974). Hence, the

211 stream power model describes the variation of channel elevation in time ( $dz/dt$ ) (Howard and Kerby,  
212 1993; Whipple and Tucker, 1999):

$$213 \quad \frac{dz}{dt} = U - KA^m S^n \quad (1)$$

214 where  $U$  is the rock uplift rate,  $K$  is the fluvial erodibility coefficient controlled by bedrock lithology,  
215 climate and sediment load,  $A$  is the upstream drainage area,  $S$  is the local channel slope and  $m$  and  $n$   
216 are constants that depend on basin hydrology, channel geometry and erosional processes (Howard,  
217 1994; Whipple and Tucker, 1999). Under steady-state conditions erosion and rock uplift rates ( $U$ ) are  
218 balanced (Willett and Brandon, 2002; Kirby and Whipple, 2012), and there is no change in elevation  
219 of the channel bed over time ( $dz/dt = 0$ ). Therefore, equation (1) can be rearranged as:

$$220 \quad S = \left(\frac{U}{K}\right)^{\frac{1}{n}} A^{-\left(\frac{m}{n}\right)} \quad (2)$$

221 where  $(U/K)^{1/n}$  and  $m/n$  are the channel steepness index ( $k_s$ ) is the concavity index ( $\theta$ ), respectively  
222 (Flint, 1974). The relationship in equation (2) is only valid above a critical upstream drainage area of  
223 0.1 to 5 km<sup>2</sup>, where fluvial processes dominate over debris flow processes (Montgomery and  
224 Fournelle, 1993; Stock and Dietrich, 2003; Wobus et al., 2006).  $k_s$  and  $\theta$  can be extracted from DEMs  
225 by a logarithmic regression of the local channel slope versus the contributing drainage area (Whipple,  
226 2004; Wobus et al., 2006; Table S1 in the supporting information) or through an integral approach  
227 (Perron and Royden, 2013; Mudd et al., 2014 see explanation below; Table S2 in the supplementary  
228 information).  $k_s$  is sensitive to spatial variations in bedrock erodibility, climate and rock uplift rate  
229 and hence represents a fundamental metric for geomorphic studies (Snyder et al., 2000; Wobus et al.,  
230 2006). Because small variations in the concavity index produce large variations in  $k_s$  and considering  
231 that DEM-noise can have a strong impact on  $\theta$  and consequently on  $k_s$ , we used a typical reference  
232 concavity index ( $\theta_{ref}$ ) of 0.45 (e.g., Wobus et al., 2006; Kirby and Whipple, 2012). The chosen  $\theta_{ref}$   
233 is the most used value in the literature to date (e.g., Kirby and Whipple, 2012) and falls in the range  
234 of  $\theta$  estimates for every stream segment upstream and downstream of non-lithological knickpoints of  
235 the Anti-Atlas (Snyder et al., 2000; Wobus et al., 2006; Tables S1 and S2 in the supporting

236 information). The use of a  $\theta_{ref}$  allows calculating the normalized channel steepness index ( $k_{sn} =$   
 237  $(U/K)^{1/n}$ ) and hence to effectively compare longitudinal profiles with greatly varying drainage areas  
 238 and infer relative variations in rock uplift rates. Specifically, in areas with similar climate and rock  
 239 strengths, rivers with higher  $k_{sn}$  values will reflect higher uplift rates (e.g., Olivetti et al., 2012; Miller  
 240 et al., 2013).

241 Furthermore, we performed a regional scale topographic and statistical analysis, using the integral  
 242 approach calculating  $\chi$  along the main river segments. The method is based on the transformation of  
 243 the horizontal coordinates of a river profile to the  $\chi$  reference frame assuming steady-state conditions  
 244 and spatially invariant uplift rates and bedrock erodibility (Perron and Royden, 2013):

$$245 \quad z(x) = z(x_b) + \left(\frac{U}{KA_0^m}\right)^{\frac{1}{n}} \int_{x_b}^x \left(\frac{A_0}{A(x')}\right)^{\frac{m}{n}} dx = z(x_b) + k_s A_0^{-\left(\frac{m}{n}\right)} \chi \quad (3)$$

$$246 \quad \chi = \int_{x_b}^x \left(\frac{A_0}{A(x')}\right)^{\frac{m}{n}} dx \quad (4)$$

247 where  $\chi$  is the independent variable of integral quantity in the upstream direction from a base level  $x_b$   
 248 to an observation point  $x$ ,  $z$  is the elevation along the channel,  $k_s$  (or  $k_{sn}$  assuming a reference  
 249 concavity) is the steepness index and  $A_0$  is the reference drainage area, usually assumed to be 1 km<sup>2</sup>  
 250 (Perron and Royden, 2013). To calculate  $\chi$ , a value of  $\theta$  must be specified. In results section we  
 251 always refer to  $\chi$  assuming  $\theta_{ref} = 0.45$  as specified above. However, by collapsing the tributaries to a  
 252 linear relationship in the  $\chi$ - $z$  plot, it is possible to estimate individual  $\theta$  of the selected stream  
 253 segments (Mudd et al., 2014). In this case, a linear regression of elevation against  $\chi$  permits  
 254 determination of  $k_{sn}$  for an equilibrated river for the upstream and downstream river segments of  
 255 transient river profiles (Perron and Royden, 2013; Smith et al., 2022). Finally, the results of  $k_{sn}$  (using  
 256  $\theta_{ref}$  of 0.45) and the optimized  $\theta$  for each river segments of the Anti-Atlas obtained through the log  
 257 slope -log area and the integral approach are reported in Tables S1 and S2 in the supporting  
 258 information, respectively. Importantly, the integral approach allows visualizing  $k_{sn}$  variation along  
 259 the stream segments and to discretize the knickpoints. Moreover, in the  $\chi$ - $z$  plot the slope is

260 proportional to the  $k_{sn}$ . In areas where erodibility and climate variability are marginal, the river  
261 network analysis can be used to infer and visualize the pattern of relative rock uplift rate across the  
262 region. Usually, a variation in rock uplift rate is identified by the presence of “transient knickpoints”  
263 which separate portions of the landscape eroding at different rates (Kirby and Whipple, 2012; Royden  
264 and Perron, 2013; Mudd et al., 2014). A detailed analysis of these features is fundamental to  
265 understand the state of a landscape. Distinguishing the nature of the knickpoints requires a detailed  
266 analysis of the geological and geomorphic characteristics (Kirby and Whipple, 2012). Transient and  
267 lithological knickpoints were differentiated by looking at: (1) their position and distribution in the  
268  $\chi$ - $z$  plot (*i.e.*, rivers that experienced a similar rock uplift history should cluster in the  $\chi$ - $z$  plot; Gallen  
269 and Wegmann, 2017; Figure S2 in the supporting information); (2) available geological maps (1:  
270 200.000, 100.000 and 50.000, Service Géologique du Maroc); and (3) satellite imagery on Google  
271 Earth.

272 A Shuttle Radar Topography Mission Digital Elevation Model (SRTM DEM, pixel size of 90 m) was  
273 used to perform the topographic and the river network analysis described above. All steps were  
274 conducted using ArcGIS tools, TopoToolbox (Schwanghart and Scherler, 2014), TAK (Forte and  
275 Whipple, 2019) and a series of MATLAB functions (Goren et al., 2014; Gallen, 2017; Smith et al.,  
276 2022).

277

### 278 **3.2. River projections 1D and 2D**

279 The magnitude of fluvial incision, associated with changes in rock uplift, can be estimated from the  
280 relict topography upstream of major non-lithological knickpoints (Berlin and Anderson, 2007;  
281 Schildgen et al., 2012; Gallen et al., 2013; Miller et al., 2013). In particular, the reconstructed river  
282 projection from the relict landscape permits determination of the paleo-base level and hence the  
283 magnitude of minimum incision/surface uplift and paleo-relief before the development of the  
284 knickpoints (Olivetti et al., 2016; Heidarzadeh et al., 2017; Fox et al., 2019). Particularly, the  
285 estimates represent the incision into a specific surface which may be undergoing continued erosion

286 itself. Therefore, incision may not represent total erosion but the difference between the erosion  
 287 across the low-relief landscape and that within the incising part of the landscape. We carry out two  
 288 types of river projections: a) one dimensional projections where the elevation only varies as function  
 289 of distance along a single channel and the model parameters are single values of surface uplift and  
 290 paleo-channel steepness; and b) two dimensional projections where elevation varies as a function of  
 291 space and the model parameters are maps of surface uplift and paleo-channel steepness. Both the  
 292 methods require a fixed value of  $\theta_{ref}$ , which has been assumed to be 0.45 as discussed in section 3.1.  
 293 The one dimensional projections were carried out in  $\chi$  space. To do this a linear model was regressed  
 294 through the  $\chi$ -elevation data from the relict part of the landscape. The intercept with y axis (i.e., where  
 295  $\chi=0$ ) provides the elevation of the paleo-base level. This approach relies on several assumptions: that  
 296 the paleo-river network has remained approximately the same through time; erosion rates across the  
 297 relict landscape have remained constant; the channel steepness in the paleo-landscape was spatially  
 298 uniform; and that the change in base level due to surface uplift is spatially uniform. The assumption  
 299 that the erosion rates have remained overall steady across the Anti-Atlas relict landscape is justified  
 300 by the close match between short and long-term erosion rates throughout the Cenozoic (i.e., erosional  
 301 steady-state; e.g., Willett and Brandon, 2002; Clementucci et al., 2022). However, there is no  
 302 guarantee that the projected rivers within the same catchment will predict the same amount of surface  
 303 uplift. This has the benefit of providing a test of the underlying assumptions, however, the resulting  
 304 landscape may be unrealistic because predicted elevations at confluences may be different.  
 305 A two-dimensional approach, proposed by Fox (2019), allows reconstructing the paleo-topography  
 306 ensuring tributaries and trunk streams share the same elevation at confluences. This approach was  
 307 extended by Fox et al. (2020) and Smith et al. (2022) to account for spatial variability in surface uplift.  
 308 The basis of this approach is that a discrete version of the stream power model can be written using  
 309 a series of nodes along the main trunk river:

$$310 \quad z_i - B.L. = \sum_{j=1}^i (\Delta\chi_j) u_j^* + S.U._i \quad (5)$$

311 where the  $i$ th pixel is the upstream of the  $j$ th pixel and the lowest most pixel has the elevation of B.L.  
312 (base level),  $S.U.i$  is the surface uplift that the relict landscape has experienced following fluvial  
313 dissection,  $u^*$  is the normalized rock uplift rate, which is proportional to the normalized channel  
314 steepness that is preserved across the relict landscape. This expression provides a prediction of  
315 elevation as a function of channel steepness and surface uplift. Provided both vary smoothly in space  
316 over long length scales, the elevation of pixels within the DEM can be used to recover these values  
317 using inverse methods. The results provide a reconstructed pre-incision landscape and allows  
318 quantifying the amount of surface uplift for each node (Smith et al., 2022). Maps of  $u^*$  and  $S.U.$  can  
319 be calculated to minimize the misfit between predicted and observed topography of the relict  
320 landscape and the roughness of the  $u^*$  and  $S.U.$  maps. In this case, the  $\chi$  values were calculated for  
321 the entire drainage network of the Anti-Atlas but only the upstream knickpoints on the relict landscape  
322 were used to estimate the  $u^*$  and  $S.U.$ . We used values of  $m = 0.45$ ,  $A_0 = 1 \text{ m}^2$ . Because the topographic  
323 reconstruction requires many more model parameters, smoothness constraints in the form of weighted  
324 negative Laplacian operators are required. We used weighting parameters for the  $S.U.$  parameters and  
325  $u^*$  ( $\lambda$  and  $\alpha$ , respectively) equal to 10 and the grid size to 5 km, for the inversion method. The main  
326 assumptions of the method are that the shape of the river network has remained constant in time, there  
327 was no major drainage reorganization, and the erodibility coefficient ( $K$ ) is considered constant.

328

### 329 **3.3. Knickpoint celerity model**

330 A celerity model was used to estimate the onset of knickpoints migration by using the stream model  
331 shown in equation (1) and considering plucking as the primary erosion mechanism ( $n = 1$ ; Whipple  
332 et al., 2000). The horizontal migration of knickpoints along the river profiles in response to a relative  
333 base level drop can be described as:

$$334 \quad \frac{dx}{dt} = KA^m \quad (6)$$

335 where,  $dx/dt$  is the knickpoint celerity,  $K$  is a dimensional coefficient of erosion (Whipple and Tucker,  
336 1999; Whipple, 2004),  $A$  is upstream drainage area and  $m$  is a non-dimensional parameter that  
337 depends on basin hydrology, channel geometry, and erosion process (Whipple and Tucker, 1999).  
338 Particularly, we used a dynamic time-step approach as described in Crosby and Whipple (2006) and  
339 Berlin and Anderson (2007). The misfit was the difference between the real knickpoint retreat  
340 distance and the modeled one.  $K$  and  $m$  were found by a brute-force search: the best values of  $K$  and  
341  $m$  resulted in the lowest sum of squares of the misfits ( $R^2$ ) over 100,000 iterations for each simulation  
342 (Table S3; Stock and Montgomery, 1999; Crosby and Whipple, 2006; Berlin and Anderson, 2007;  
343 Sembroni et al., 2016; Sembroni et al., 2020; Siravo et al., 2021). Specifically, we performed 100  
344 simulations and calculated the mean initiation time and standard deviation of these best-fit values.  
345 Then, to have a unique time value for each modeled knickpoint, we calculated the probability density  
346 functions (PDFs) as described in Siravo et al. (2021).

347 In this specific case,  $m$  is assumed to be the concavity value, given that  $m/n = \theta$  and considering that  
348  $n = 1$  as demonstrated by Clementucci et al., (2022). Because the used approach searches the  
349 parameters by minimizing the distance between the real and modelled position of knickpoints, we let  
350  $m$  vary linearly between 0 and 0.75. This range is motivated by the concavity values obtained from  
351 the stream profiles analysis reported in Tables S1 and S2 in the supporting information. Similarly,  
352 the erodibility parameter  $K$  was permitted to vary between  $10^{-7}$  and  $10^{-4}$  (Figure S4). This range of  $K$   
353 values results from a forced-origin linear regression in the plot  $k_{sn}$  versus denudation rates ( $E$ ), using  
354 the stream power incision model ( $K = E/k_{sn}^n$ ). In particular, by using basin-averaged  $k_{sn}$  values  
355 normalized for a  $\theta_{ref}$  of 0.45 and assuming  $n = 1$ , Clementucci et al. (2022) documented that  $K$  values  
356 in the Anti-Atlas are in the order of  $10^{-6}$ - $10^{-7}$ . These values represent the minimum  $K$  values of our  
357 search interval. For the maximum values we further calculate  $K$  by using the basin-averaged  $k_{sn}$   
358 normalized for a  $\theta_{ref}$  of 0.17. We used this  $\theta_{ref}$  because the axial zone of the Anti-Atlas is  
359 characterized by a high-standing landscape with mean concavity value of  $\sim 0.17$ , which is assumed to  
360 be the most reliable value of the non-rejuvenated landscape (Clementucci et al., 2022; Tables S1 in

361 the supporting information). For the initiation point of the knickpoint propagation, we considered the  
362 present-day river outlets.

363 Finally, we set the onset of knickpoints migration between 3.8 and 18.6 Ma. This temporal range was  
364 estimated by using the maximum excavation time required to erode the missing rock volume from  
365 the river catchments (Norton et al. 2008; Gallen et al., 2013; Siame et al., 2015). The excavation time  
366 is expressed as:

$$367 \quad T = \left(\frac{V}{A}\right) E^{-1} \quad (7)$$

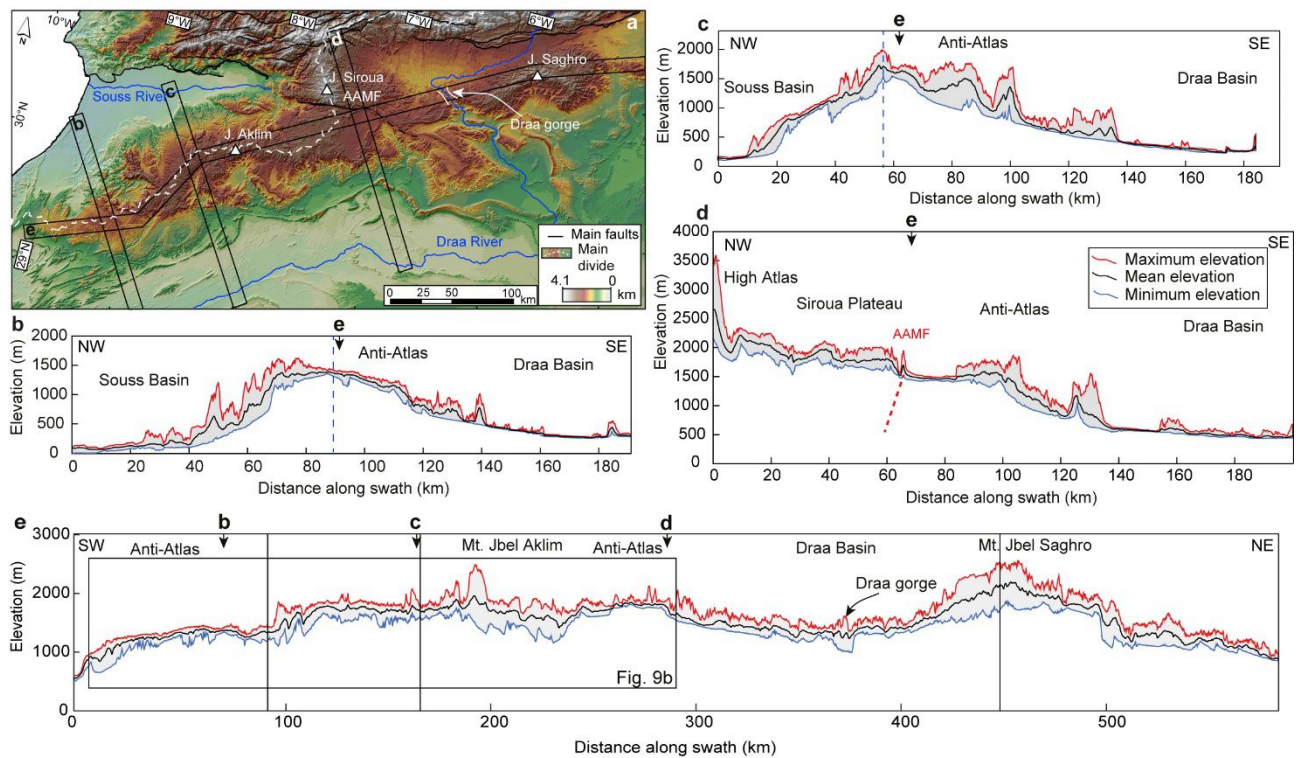
368 where  $T$  is the time required to erode the missing rock volume in the catchments,  $V$  is the rock volume,  
369  $A$  is the drainage area of the catchments and  $E$  is the basin-wide denudation rate.  $V$  can be estimated  
370 by the difference between a surface connecting the highest points in the current landscape and the  
371 current topography itself.

372

## 373 **4 Results**

374

### 375 **4.1 Topographic analysis**



376

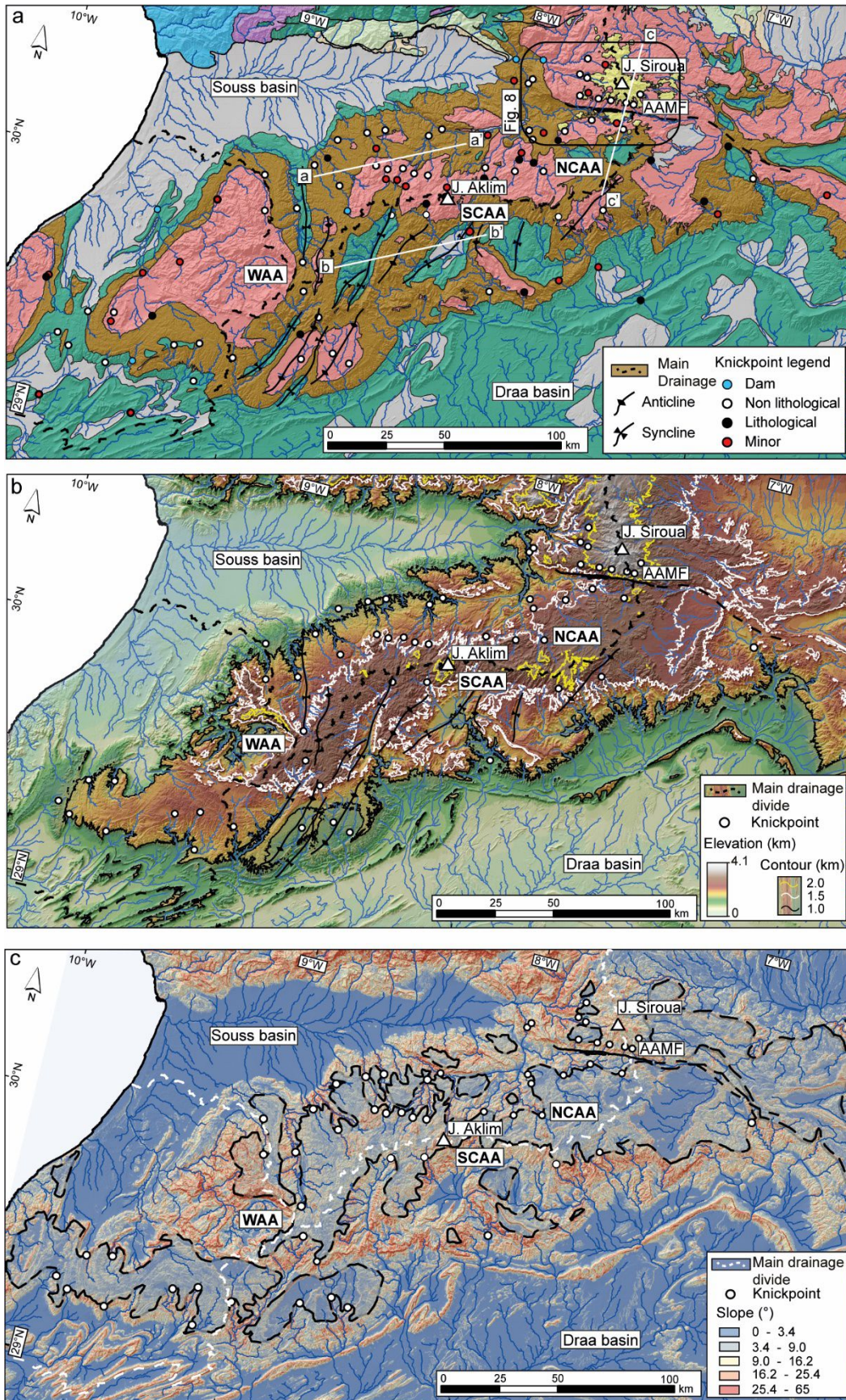
377

378 **Figure 2.** (a) Topographic map of the Anti-Atlas and the Siroua Massif (SRTM DEM database) with location  
 379 of the swath profiles. The dashed white line indicates the position of the main drainage divide. (b, c, d) are  
 380 swath profiles orthogonal to the main drainage divide of the Anti-Atlas, while (e) is parallel to the main  
 381 drainage divide. The dashed blue line indicates the position of main drainage divide on swath profiles b, c.

382

383 The AA is characterized by an extensive, high-standing (~2000 m), axial zone with low-topographic  
 384 relief delimited by steep and dissected flanks (Figure 2). The westernmost sectors of the belt have a  
 385 dome-shape geometry with a rather symmetric topography across the drainage divide (Figure 2b).  
 386 The central sectors of the western AA have an asymmetric topography with a gentle southern and a  
 387 steep northern flank grading toward the Draa and the Souss basins, respectively (Figure 2c). The  
 388 central AA has also a flat top but is bounded to the north by the Siroua plateau through a topographic  
 389 step in proximity of the Anti-Atlas Major Fault (AAMF; Figure 2d). The along-strike swath profile  
 390 highlights the geometry and the extent of the elevated axial surface, with a few mountain peaks (*e.g.*,  
 391 Mt. Jebel Aklim, 2531 m and Mt. Jebel Saghro, 2592 m) and deeply incised valley (the Draa gorge;  
 392 Figure 2a and 2e). The high-standing landscape is mostly composed of Paleozoic limestones and

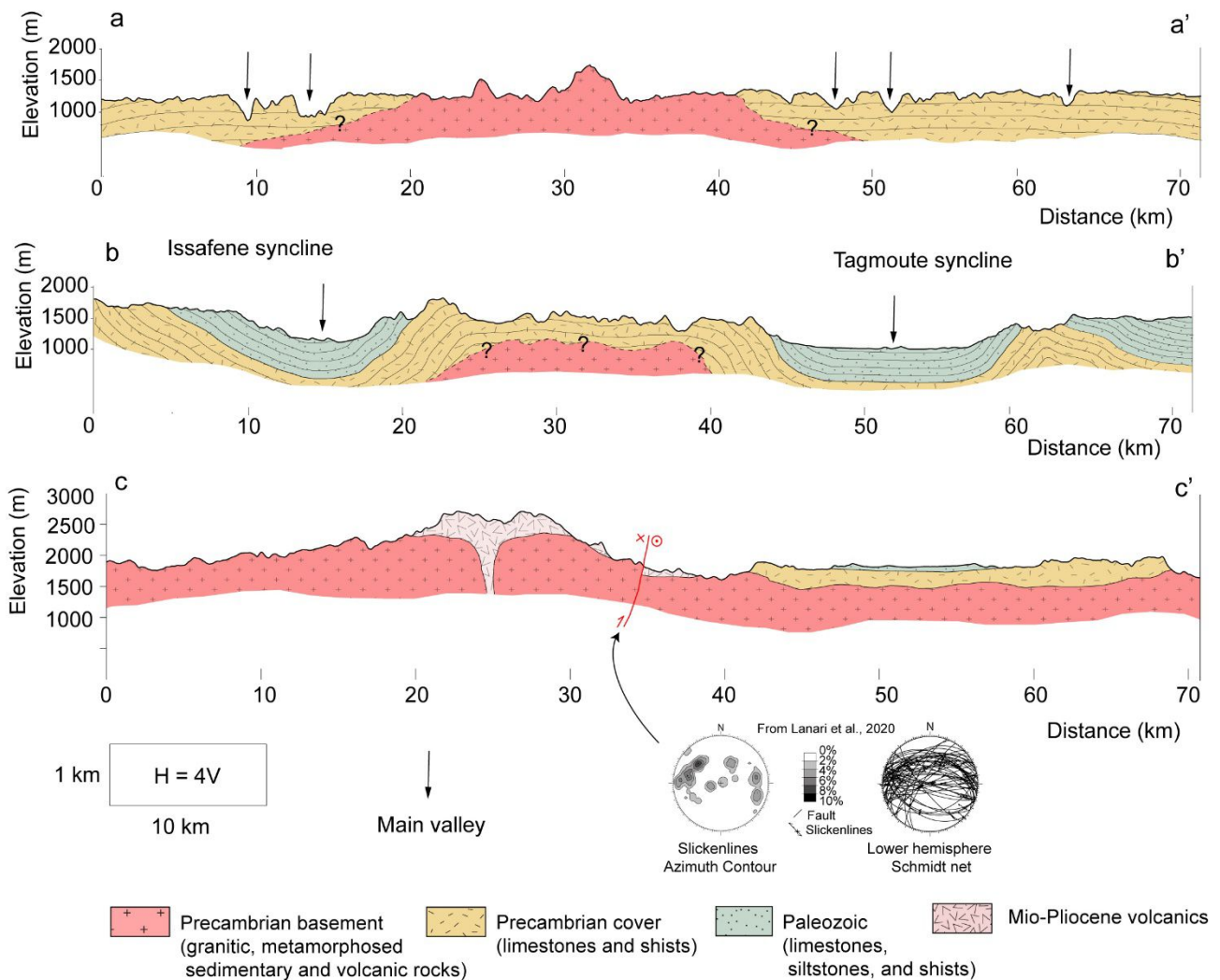
393 Precambrian basement rocks (Figure 3a) and is located upstream of non-lithological knickpoints.  
394 Downstream of these knickpoints, the topography is steeper and includes late Precambrian and  
395 Paleozoic sedimentary rocks (Figure 3). The northern flank of the belt has a slope that is sub-parallel  
396 to the bedding of late Precambrian carbonates and consists of narrow and deep valleys perpendicular  
397 to the bedding (Figure 4, profile a-a'). Conversely, the southern flank includes wide valleys mostly  
398 located along the core of the synclines with Paleozoic sediments (Soulaimani and Burkhard, 2008;  
399 Figure 4, profile b-b'). Finally, the swath profiles indicate that the high-standing, elevated surface  
400 plunges along the strike of the mountain belt (Figure 2e), and perpendicularly to it (Figure 2b, 2c).



401

402 **Figure 3.** (a) Geological map of the study area with a detailed analysis of the knickpoints for the northern flank  
 403 of the central Anti-Atlas (NCAA), western (WAA), and southern flank of central Anti-Atlas (SCAA) and the  
 404 Siroua Massif. The main fold axes are associated with the Variscan orogeny and are shown with black lines  
 405 (from Soulimani and Burkhard, 2008). (b) Topographic map (SRTM DEM database) of the study area with

406 the non-lithological knickpoints and the fold axes. The black, white, and yellow dashed lines demark the 1000,  
 407 1500 and 2000 m contours, respectively. (c) Slope map of the study area with non-lithological knickpoints.  
 408 The dashed line indicates the low-slope area of the axial zone of the Anti-Atlas. Location of the maps is shown  
 409 in figure 1b.



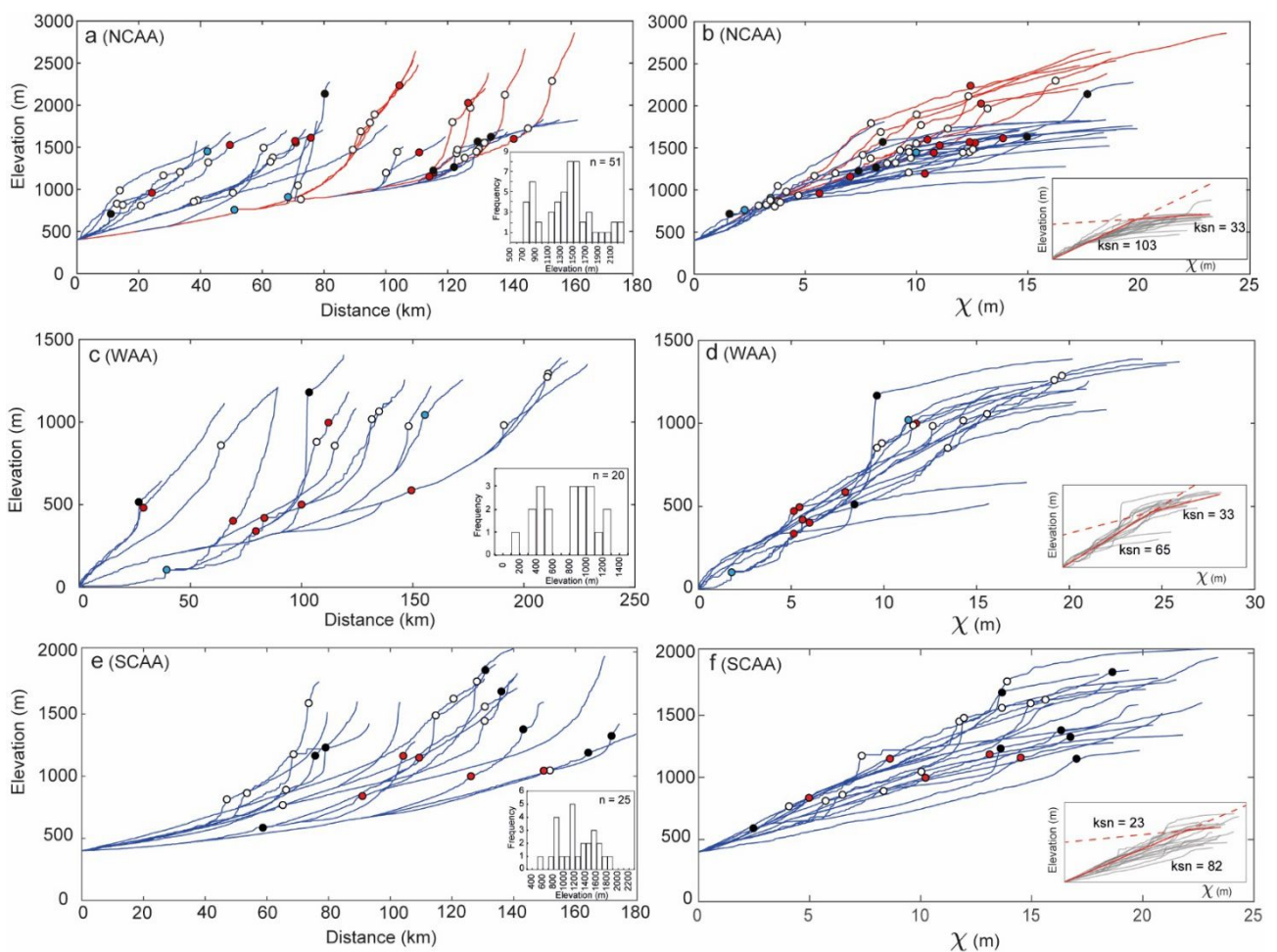
410  
 411 **Figure 4.** a-a' geological cross section of the northern flank of the Anti-Atlas. b-b' geological cross section of  
 412 the southern flank of Anti-Atlas. c-c' geological cross section in the Siroua Massif. Location of the cross-  
 413 sections is indicated in figure 3a.

414

## 415 4.2 River morphology

416 Seventeen stream profiles from the northern flank of the central Anti-Atlas (NCAA) together with  
 417 seventeen profiles from its southern flank (SCAA) and fourteen from the western side of the orogen  
 418 (WAA) were analysed individually. The NCAA is mostly characterized by transient longitudinal river  
 419 profiles. In particular, we recognized 51 knickpoints with two main patterns of non-lithological  
 420 knickpoints standing between 700 and 1000 m and 1300 and 1500 m of elevation and several minor

421 lithological knickpoints (Figures 3a, 3b and 5a). The two patterns of non-lithological knickpoints  
 422 cluster approximately at values of  $\chi$  of 3-5 and 9-11, respectively (Figure 5b). The steepest and  
 423 concave up segments of the NCAA rivers are downstream of the highest knickpoints (Figure 5a, 5b),  
 424 whereas, the upstream segments are mostly rectilinear, have a shallow gradient and contain minor  
 425 knickpoints (Figures 3a and 5a, 5b). Another minor group of knickpoints separating gentle upstream  
 426 river segments from steeper downstream portions is in the Siroua Massif, over 2000 m of elevation  
 427 (see red profiles in figure 5a and 5b), upstream of the Anti-Atlas Major Fault (AAMF, Figure 6).



428  
 429 **Figure 5.** Longitudinal river profiles and  $\chi$  plots with major knickpoints for (a-b) NCAA, (c-d) WAA, and (e-  
 430 f) SCAA. The rivers of NCAA and SCAA sectors are extracted from the bedrock-alluvial transition, which in  
 431 the study area is around 400 m. The knickpoints legend is in figure 3a. The red profiles indicate the rivers  
 432 flowing from the Siroua Massif. The inset plots in the  $\chi$  space show the mean regional  $k_{sn}$  values upstream and  
 433 downstream of the highest knickpoints. The inset histograms in the longitudinal profiles show the frequency  
 434 distribution of the elevation of the knickpoints.  
 435

436 The WAA sector presents also transient river profiles with approximately 20 knickpoints. Most of  
 437 the non-lithological knickpoints are located within a relatively narrow elevation band, of about 800

438 to 1100 m while the minor knickpoints are at about 400 to 500 m (Figure 5c, 5d). The steeper  
439 downstream portion of the major non-lithological knickpoints exhibit a concave-up geometry with a  
440 few minor knickpoints (Figure 5c, 5d). The upstream segments are mostly rectilinear with a typical  
441 equilibrium profile (straight segment in  $\chi$  space; Figure 5d). Here, the two patterns of knickpoints at  
442  $\sim 500$  m and  $\sim 1000$  m, occur approximately at  $\chi$  values of 5-6 and 10–15, respectively (Figure 5d).  
443 The SCAA sector is characterized by both, equilibrated and transient longitudinal river profiles and  
444 contain at least 25 knickpoints distributed across a wide range of elevation (Figure 5e). Most of the  
445 non-lithological knickpoints stand at about 800 to 1000 m of elevation and over 1500 m of elevation,  
446 while the lithological knickpoints are at an elevation range of 1000 to 1500 m (Figure 5e, 5f).  
447 Overall, most of the rivers are characterized by transient conditions with mean  $k_{sn}$  values of  $84 \pm 3.8$   
448 ( $\sigma = 19.7$ )  $m^{0.9}$  and  $30 \pm 2.9$  ( $\sigma = 14.8$ )  $m^{0.9}$ , and  $\theta$  values of  $0.58 \pm 0.04$  ( $\sigma = 0.22$ ) and  $0.17 \pm 0.03$  ( $\sigma$   
449  $= 0.18$ ) in the downstream and the upstream segments, respectively (Table 1 and Table S1 in the  
450 supporting information).

451 **Table 1**

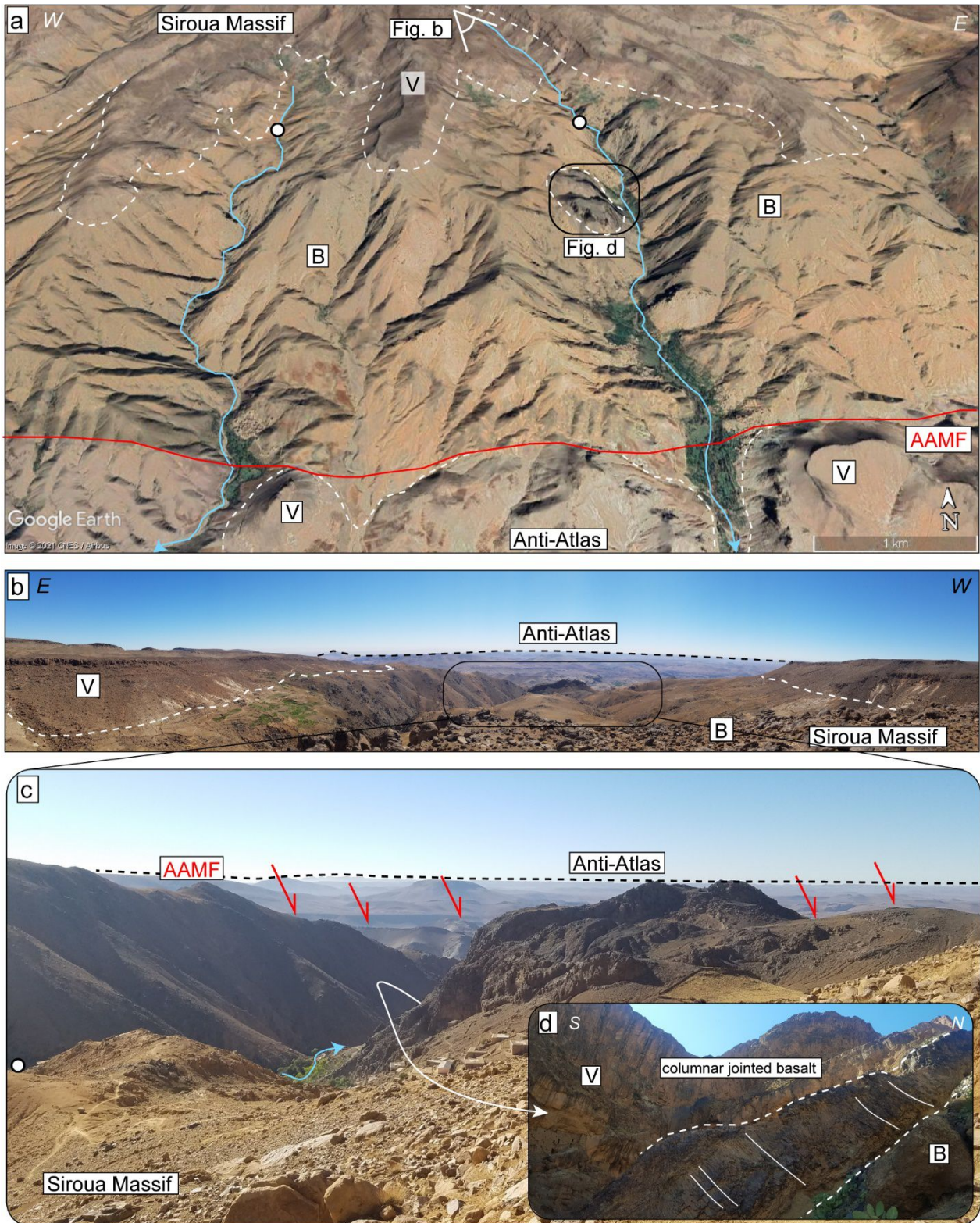
452 *Summary of  $k_{sn}$  and  $\theta$  values upstream and downstream of non-lithological knickpoints obtained through a*  
453 *linear regression of slope against drainage area on a log-log plot (see details in Table S1 of the supporting*  
454 *information).*

Sector		Stream parameters			
		Downstream		Upstream	
		$k_{sn}$ ( $m^{0.9}$ ) <sup>f</sup>	$\theta$ <sup>g</sup>	$k_{sn}$ ( $m^{0.9}$ )	$\theta$
NCAA <sup>a</sup>	mean <sup>d</sup>	$102.6 \pm 4.7$	$0.44 \pm 0.02$	$33.2 \pm 3.5$	$0.18 \pm 0.04$
	$\sigma$ <sup>e</sup>	14.8	0.07	11.1	0.14
SCAA <sup>b</sup>	mean	$82.2 \pm 2.7$	$0.57 \pm 0.03$	$22.7 \pm 5.1$	$0.17 \pm 0.07$
	$\sigma$	7.2	0.09	13.5	0.2
WAA <sup>c</sup>	mean	$65.07 \pm 3.1$	$0.75 \pm 0.1$	$33.23 \pm 6.1$	$0.14 \pm 0.07$
	$\sigma$	9.45	0.3	18.5	0.22
Tot	mean	$84.1 \pm 3.8$	$0.58 \pm 0.04$	$30.4 \pm 2.9$	$0.17 \pm 0.03$
	$\sigma$	19.7	0.22	14.8	0.18

455  
456 *Note.* <sup>a</sup> NCAA: rivers draining the northern flank of Anti-Atlas. <sup>b</sup> SCAA: rivers draining the southern flank of  
457 Anti-Atlas. <sup>c</sup> WAA: rivers draining the western flank of Anti-Atlas. <sup>d</sup> Mean and standard error values. <sup>e</sup>  
458 Standard deviation of the data. <sup>f</sup> Channel steepness calculated by using a reference concavity of 0.45. <sup>g</sup>  
459 Concavity value calculated by the slope of the line regressed through a log-log plot of channel slope vs.  
460 drainage area.

461  
462

463 The  $k_{sn}$  and  $\theta$  values obtained with the log S-log A method were compared with those estimated with  
464 the  $\chi$  method (Tables S1 and S2 in the supporting information).  $k_{sn}$  values lie mostly on the 1:1 trend  
465 (Figure S3a), while the  $\theta$  values show a higher dispersion (Figure S3b). Finally, the elevation and  
466 distance from the river mouth show a positive correlation with the drainage area of catchments (Figure  
467 S5b and S5c in the supporting information).



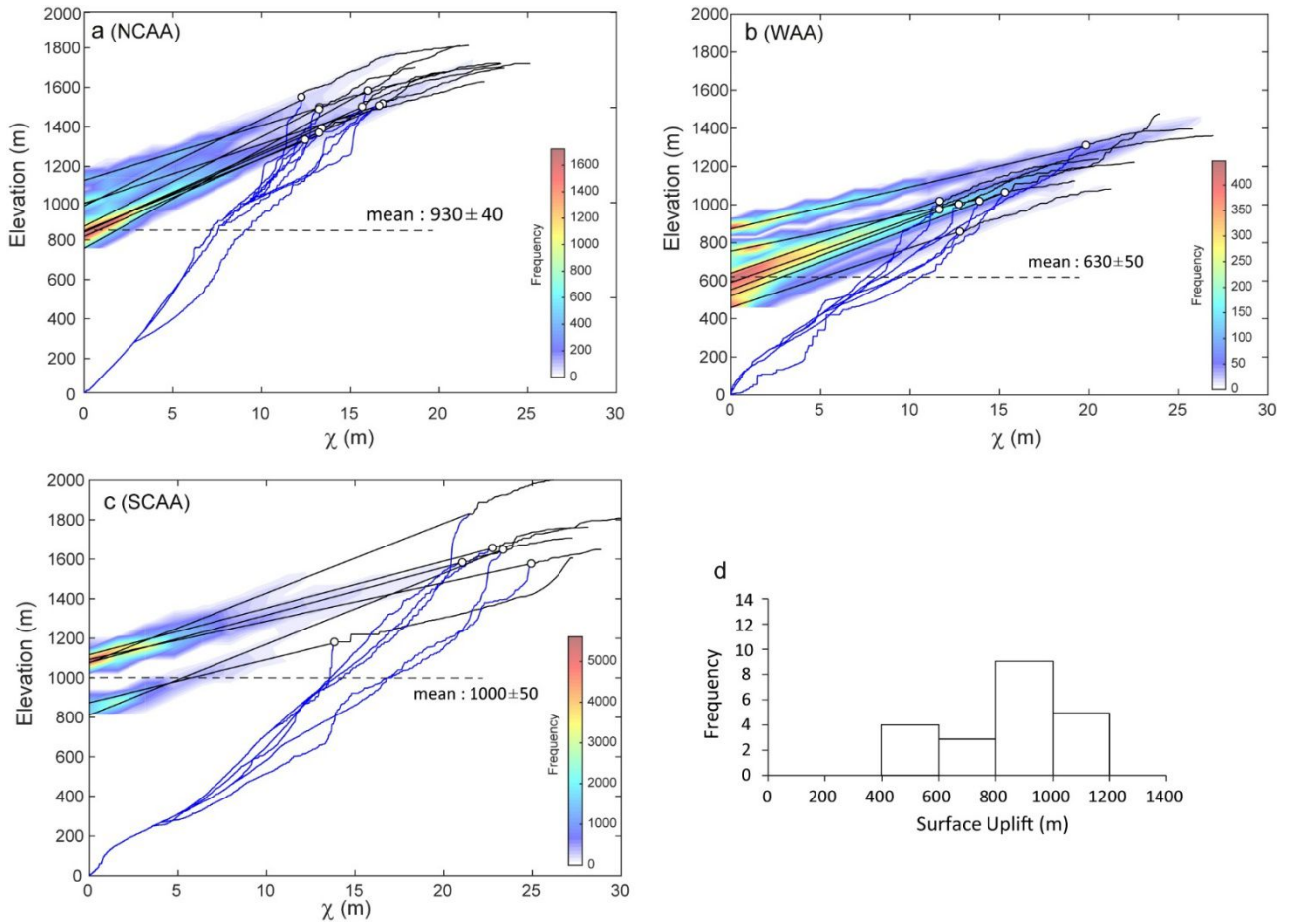
468

469 **Figure 6.** (a) Prospective Google Earth view of the southern flank of the Siroua Massif. Note the volcanic  
 470 edifice composed of lava flows demarked by the dashed white line (see V symbol) resting unconformably over  
 471 the Precambrian basement (see B symbol), the north-dipping Anti-Atlas Major Fault (AAMF), the non-  
 472 lithological knickpoints shown with a white dot, the deep incisions and the remanence of the lava flows  
 473 downstream of the non-lithological knickpoints. (b) Panoramic view from the Siroua Massif showing in the  
 474 background the summit erosional surface (i.e., relict landscape) of the Anti-Atlas (see dashed black line) and  
 475 in the foreground the contact between the basement (B) and the lava flows (V). (c) Detail of figure 6b showing  
 476 the basalt flow preserved in the deeply incised valley of figure 6a. (d) Field picture of the basalt of figure 6c  
 477 with high angle columnar joint (white lines) perpendicular to the valley bottom (dashed white lines).

478

## 479 4.3 Magnitude of fluvial incision

### 480 4.3.1 1D river projection



481

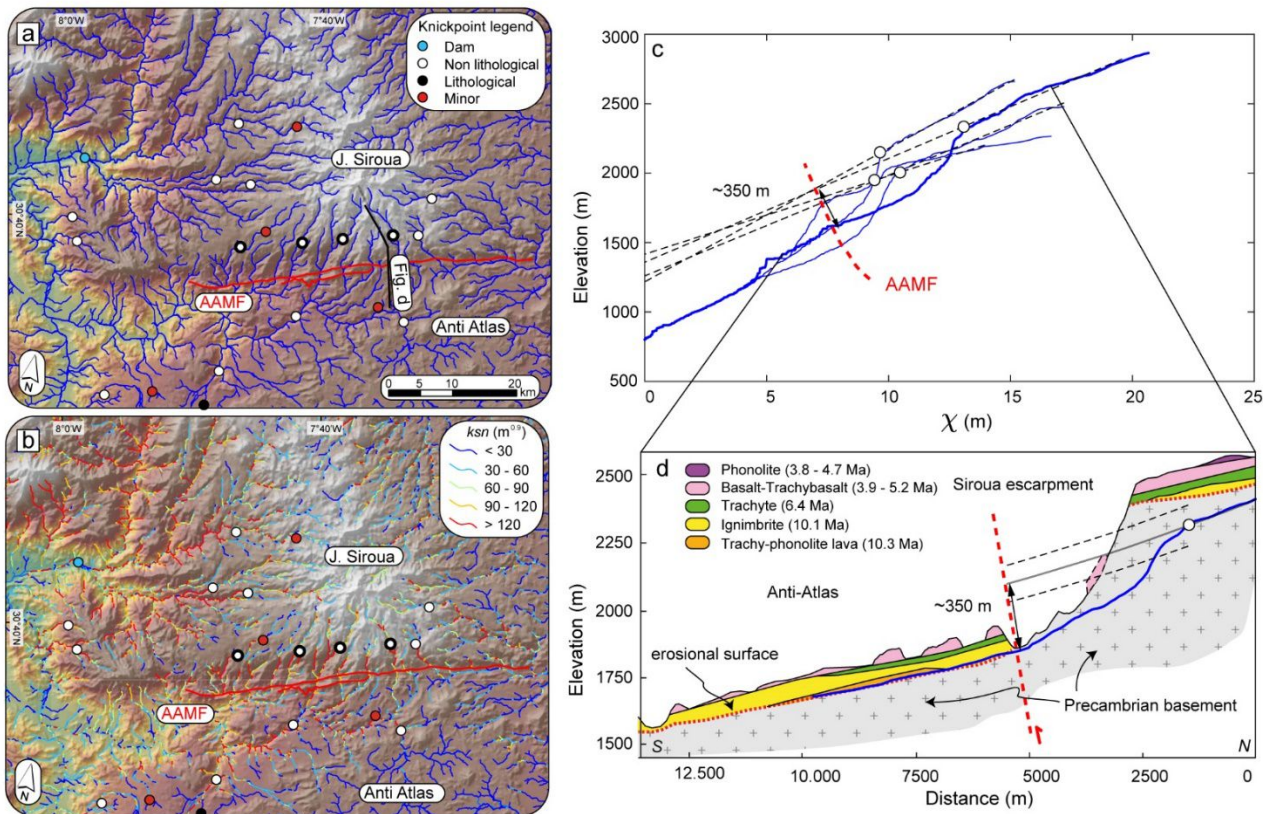
482 **Figure 7.** Modern longitudinal profiles and projections of the relict landscape (red segments) upstream of the  
483 highest knickpoints using  $\theta_{ref} = 0.45$  and the  $k_{sn}$  of the relict portion for the (a) NCAA, (b) WAA, and (c) SCAA  
484 sectors. Major knickpoints are marked with white circles. (d) Frequency diagrams of the magnitude of surface  
485 uplift for the different sectors.

486

487 The Souss and Draa outlets represent the present-day base level for the NCAA and SCAA rivers,  
488 respectively, whereas the WAA rivers flow directly into the Atlantic Ocean. To a first approximation  
489 we can consider that all rivers of the Anti-Atlas drained toward the Atlantic before the relative base  
490 level fall that initialized the most elevated non-lithological knickpoints (Figure 5). This because the  
491 opening of the South Atlantic Ocean had already occurred in the early Cretaceous (Torsvik et al.,  
492 2009) and hence much earlier than the Cenozoic topographic rejuvenation. Estimated values of fluvial  
493 incision for the NCAA based on 10 stream profiles range from 822 ( $2\sigma = 36$ ) to 1162 m ( $2\sigma = 18$ ),

494 with an average of  $930 \pm 42$  m ( $\sigma = 133$ ) (Figure 7 and Table S4). In the WAA sectors, 7 transient  
495 profiles yielded fluvial incision values ranging from 459 ( $2\sigma = 9$ ) to 872 m ( $2\sigma = 29$ ), with an average  
496 of  $630 \pm 54$  m ( $\sigma = 143$ ) (Figure 7 and Table S4). Finally, in the SCAA where most of the rivers are  
497 in equilibrium, the fluvial incision based on 6 stream profiles ranges from 811 ( $2\sigma = 117$ ) to 1117 m  
498 ( $2\sigma = 18$ ), with an average of  $1008 \pm 53$  m ( $\sigma = 130$ ) (Figure 7 and Table S4). Furthermore, this  
499 approach allows estimating the first-order paleo-topographic relief as the difference between the  
500 modern mean drainage divide elevation and the elevation of the outlet of the reconstructed river  
501 profiles. Our results indicate a mean elevation difference of 970, 890 and 750 m for the NCAA,  
502 SCAA, and WAA sectors, respectively (Table S4 in the supporting information).

503 In the Siroua Massif, rivers are characterized by strong disequilibrium profiles with high-standing  
504 non-lithological knickpoints lying at the margin of a low-topographic relief area and delimiting  
505 streams with high  $k_{sn}$  from those with low  $k_{sn}$  values (Figures 6a, 8a, 8b). The magnitude of fluvial  
506 incision along the Siroua escarpment was obtained by projecting the upstream portions of the rivers  
507 up to the Anti-Atlas Major Fault (AAMF; Figure 8c, 8d). This value is  $\sim 350$  m and represents only  
508 the amount of incision between the Siroua Massif and the central sector of AA.



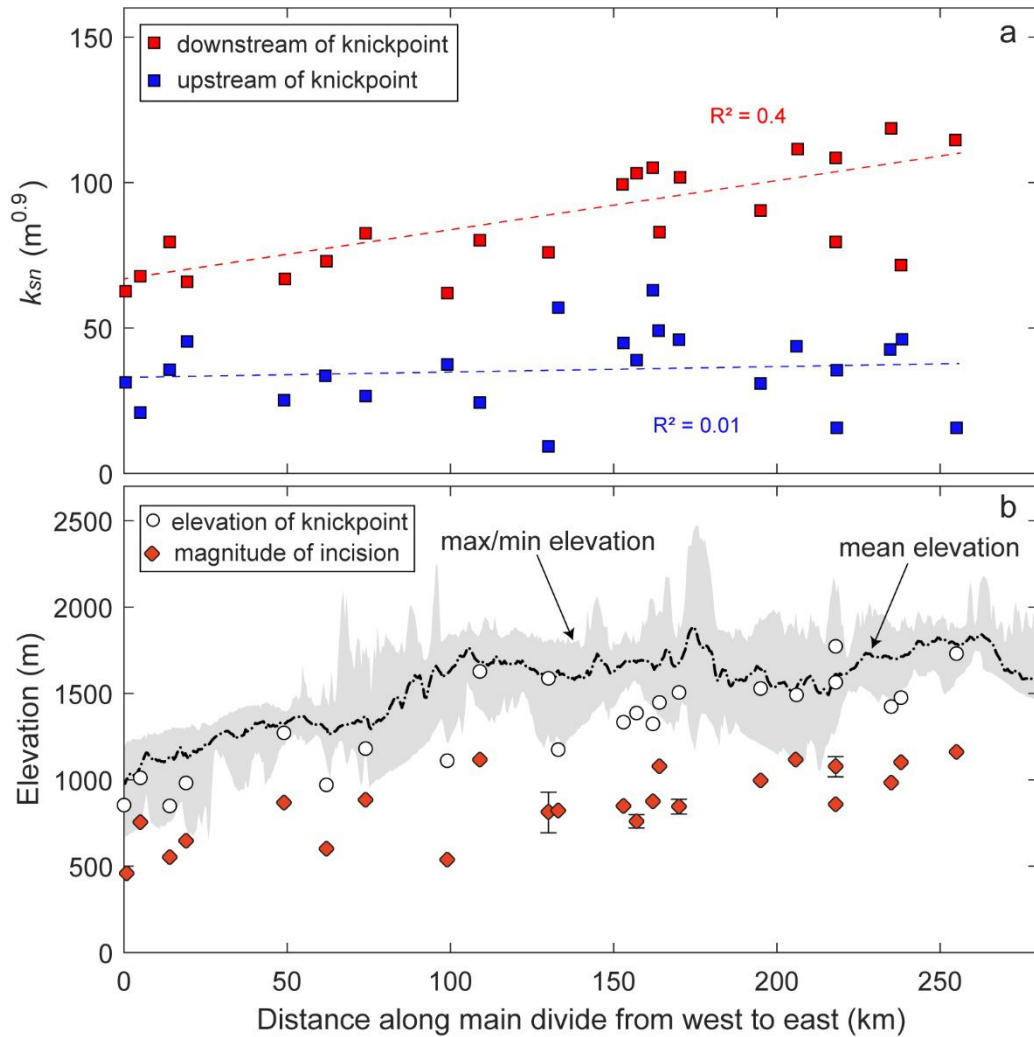
509

510 **Figure 8.** (a) Topographic map (SRTM DEM database) of study area with the main knickpoints. Bold blue  
 511 rivers and associated knickpoints (thick black circles) are projected in figure 8c. (b)  $k_{sn}$  map of the stream  
 512 network in the Siroua area. Location of the maps is shown in figure 3A. (c) Modern longitudinal profiles and  
 513 projections from the Siroua relict landscape (dashed black segments) upstream of the highest knickpoints using  
 514  $\theta_{ref} = 0.45$  and the  $k_{sn}$  of the relict portion. Note, the reconstructed river projections intersect each other  
 515 between 5 and 10 of  $\chi$ . (d) Geological profile of the Siroua escarpment (after De Beer et al., 2000). The minimum  
 516 value of incision is 350 m.

517

518 Overall, our projections document a progressive increase in the magnitude of fluvial incision and in  
 519 the elevation of the highest knickpoints from the WAA to the central sector of AA with a culmination  
 520 in the Siroua Massif (Figure 9b). This is also associated with a regional increase in  $k_{sn}$  values  
 521 downstream of the major knickpoints (red dots in figure 9a).

522



523

524 **Figure 9.** (a) Distance along the main drainage divide versus  $k_{sn}$  down and upstream of the non-lithological  
 525 knickpoints (data from Table S1). (b) Distance along the main drainage divide versus knickpoint elevation and  
 526 estimated surface uplift values. The location of the swath profile is indicated in figure 2d.

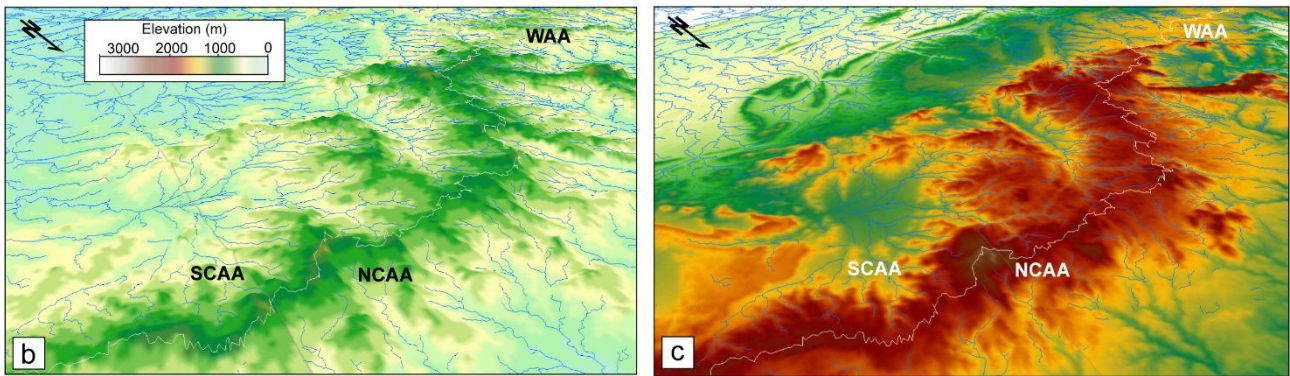
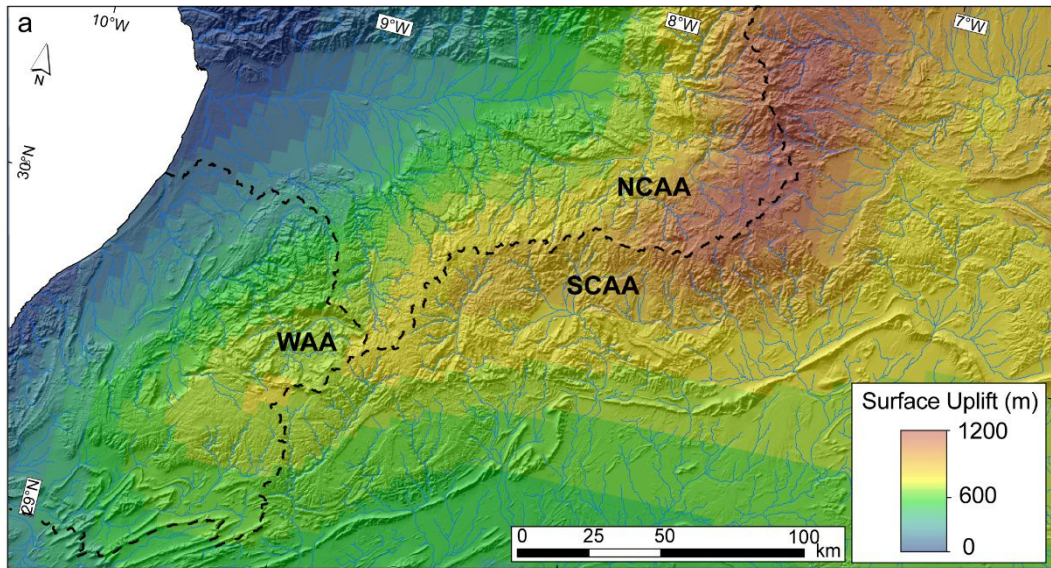
527

### 528 4.3.2 2D river projection

529 The 2D river projection method makes it possible to estimate the distribution of surface uplift (or  
 530 base level fall) and normalized rock uplift rates,  $u^*$  proportional to  $k_{sn}$ , as a function of the elevations  
 531 and the  $\chi$  values from the relict river network (in the portion of landscape demarcated by black  
 532 polygon in figure 3c). Due to the increased spatial variability provided by this approach, multiple  
 533 solutions which pass through the  $\chi$  and elevation data are expected, and results are non-unique.  
 534 Damping forces smooth maps providing a means to choose a preferred result. Here damping  
 535 parameters are chosen to ensure that results are consistent with the estimates obtained from projecting  
 536 the information preserved in the upper reaches of the transient river profiles. Results suggest an

537 incision associated with a base level fall in the order of ~1200 m in the Siroua Massif, that decreases  
538 gradually to ~500 m in the WAA (Figure 10a). The  $u^*$  values in the upstream relict landscape at the  
539 maximum elevation are rather uniform with major variations coinciding with the highest mountain  
540 peaks composed mostly of quartzites and metamorphosed conglomerates (Figures 1b and S6 in the  
541 supporting information). Finally, the reconstructed paleo-topography indicates a maximum elevation  
542 of ~1000 and ~500 m in the central sector of AA and the WAA, respectively before the onset of uplift  
543 (Figure 10b). These results are consistent with those obtained from the river projections but with a  
544 greater spatial resolution (Figure 10a, 10c). It should be noted that the fitted surface through the relict  
545 topography above the incised landscape is less constrained in the Souss, Draa basins and in the Siroua  
546 Massif. In the two basins, aggradation/deposition processes recorded by Plio-Quaternary sedimentary  
547 sequences (Hssaine and Bridgland, 2009) are not taken into consideration. Moreover, the maximum  
548 elevation obtained for the Siroua Massif represents a maximum estimate because the construction of  
549 the volcanic edifice may be coeval or younger than the timing of the fluvial incision, as testified by  
550 preserved lava flows along the Siroua escarpment (Figures 6d and 8d).

551



552

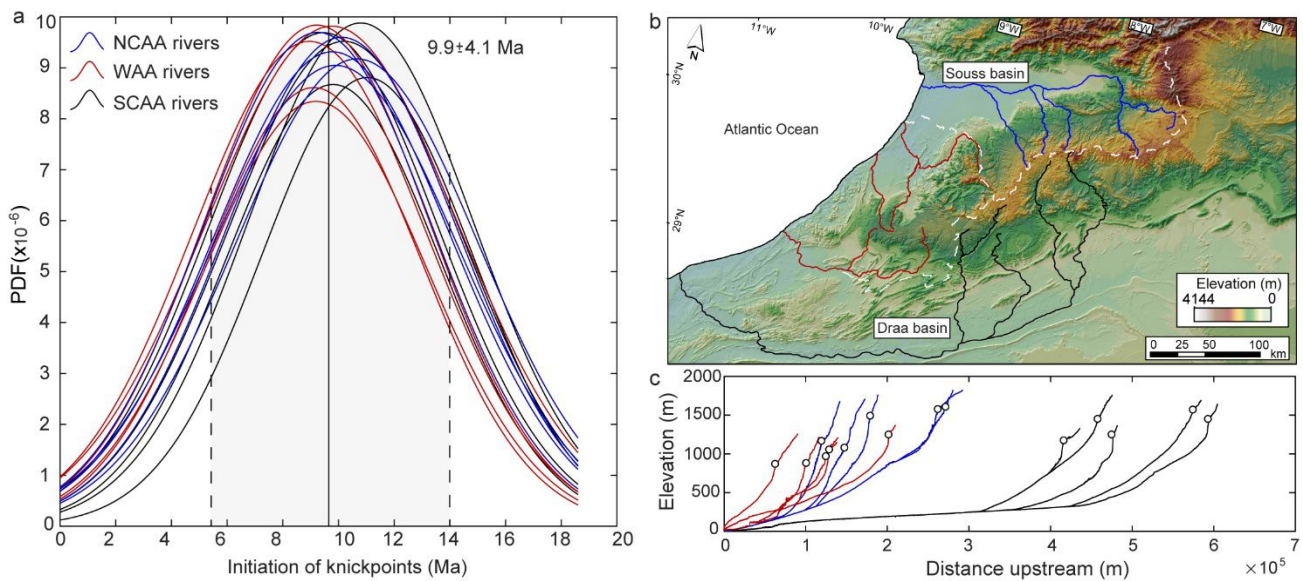
553 **Figure 10.** (a) Surface uplift (*S.U.*) map. The base level is defined at the relict landscape boundary; values of  
 554  $m = 0.45$  and  $A_0 = 1 \text{ m}^2$  were used to calculate  $\chi$  and  $u^*$  (Equation 5). (b) Paleo-topographic reconstruction of  
 555 the central and western Anti-Atlas. (c) Present-day topography of central and western Anti-Atlas.

556

#### 557 4.4 Timescales of knickpoint migration

558 The time the highest non-lithological knickpoints took to travel from the base level to their present-  
 559 day position is in the same range of that one required to erode the volume of rocks in a catchment  
 560 between a high-standing preserved landscape and the minimum topography (*e.g.*, Gallen et al., 2013;  
 561 Siame et al., 2015). This is called “excavation time” and is generally calculated assuming that erosion  
 562 took place at constant rates. This volume of removed material includes the downstream (adjusted)  
 563 and upstream portion (relict landscape) of the catchments, therefore the timing to remove it is higher  
 564 than the time required to remove materials only in the rejuvenated portion. Furthermore, denudation  
 565 rates derived from  $^{10}\text{Be}$  concentrations for the Anti-Atlas Mountains are representative mainly for the  
 566 relict landscape, as discussed in Clementucci et al. (2022). This because the quartz-bearing lithologies

567 are mostly exposed upstream of non-lithological knickpoints. Hence, denudation rates of 5.8 to 12.5  
 568 m/Myr (Table S5 and Figure S7) provide a maximum age for the onset of topographic relief  
 569 production in the relict landscape of the Anti-Atlas (8.8 to 18.6 Myr in Table S5 in the supporting  
 570 information). Conversely, the highest value of denudation represents a mixed value (21.3 m/Myr in  
 571 Table S5) from the Anti-Atlas relict and adjusted flanks, providing a minimum age  $\sim$ 3.8 Myr (Table  
 572 S5).



573  
 574 **Figure 11.** Initiation time of knickpoints propagation for the different sectors of the Anti-Atlas (NCAA, WAA,  
 575 SCAA). (a) Probability Density Function of the timing of knickpoint initiation. (b) DEM showing the modelled  
 576 rivers. (c) River longitudinal profiles and associated knickpoints of the modelled rivers. For further information  
 577 see also table S3 in the supporting information.

578

579 The results from the selected river profiles are very consistent and indicate an onset for the upstream  
 580 propagation of the base level fall at  $9.9 \pm 4.3$ ,  $9.2 \pm 4.1$  and  $10.4 \pm 4.0$  Myr for the NCAA, WAA and  
 581 SCAA sectors, respectively (averaged value  $9.9 \pm 4.1$  Myr; Figure 11 and Table S3).

582

## 583 5 Discussion

### 584 5.1 Significance of the transient topography

585 The strong variations in the normalized channel steepness indices, concavity values, topographic  
586 slope, elevation, and fluvial incision between the portions of the landscape downstream and upstream  
587 of highest non-lithological knickpoints (Figures 3 and 5) document the occurrence of a topographic  
588 dichotomy, which is typical of a landscape in a transient state of development. Specifically, the  
589 portion downstream of the highest knickpoints is eroding faster than the elevated relict landscape,  
590 which is has been eroding at low and fairly uniform erosion rates at least since the late Cretaceous  
591 (Clementucci et al., 2022). A transient topographic state could be attributed to several processes, such  
592 as drainage reorganization, climate change, eustatic sea level fall and tectonic uplift (Hancock and  
593 Kirwan, 2007; Kirby and Whipple, 2012; Miller et al., 2013, Ballato et al., 2015). Drainage  
594 reorganization does not appear to be the cause because of the limited evidence of knickpoints, and  
595 wind gaps formation related to river capture processes (Miller et al., 2013). An increase in erosion  
596 rates due to climate variations (*i.e.*, increase in precipitation rates) is also unlikely, because such a  
597 change would produce a decrease in the channel slopes rather than a steepening (Figure 5; Molnar et  
598 al., 2004; Wobus et al., 2010). At the same time a decrease in precipitation rates would produce  
599 sediment aggradation, in the downstream portions of non-lithological knickpoints and not stepper  
600 flanks (Lanari et al., 2022).

601 Consequently, the abrupt break in the river longitudinal profiles and  $\chi$ - $z$  plots at the highest non-  
602 lithological knickpoints and the position of the same knickpoints in the  $\chi$  space (Figures 5b, 5d, 5f,  
603 8a and S2) indicate that the two portions of the landscape erode at different rates (Schildgen et al.,  
604 2012; Miller et al., 2012; 2013; Olivetti et al., 2016). This is consistent with an increase in erosion  
605 and rock uplift rates propagating from the river outlet to the uppermost river segments (Miller et al.,  
606 2013; Gallen and Wegmann, 2017; Racano et al., 2021). Consequently, the highest knickpoints  
607 represent a response of the fluvial system to an increase in rock uplift rates and hence mark a phase  
608 of topographic rejuvenation, while the uplifted relict landscape records the previous erosional  
609 conditions predating such an increase. This implies that the magnitudes of fluvial incision represent  
610 minimum estimates of the total amount of surface uplift (*e.g.*, Kirby and Whipple, 2012). A similar

611 scenario has been described in the Appalachian Mountains (Miller et al., 2013; Gallen et al., 2013)  
612 and in other ancient orogens (Olivetti et al., 2012; Mandal et al., 2015; Calvet et al., 2015).  
613 The minor and non-lithological knickpoints located in the lower segments of the fluvial network, at  
614 700 to 1000 m and from 400 to 500 m in the NCAA, SCAA, and WAA sectors, respectively, can be  
615 attributed to a Quaternary climate forcing, eustatic sea-level changes or both (Molnar and England,  
616 1990; Crosby and Whipple, 2006; Hancock and Kirwan, 2007; Ballato et al., 2015). This pattern of  
617 knickpoints is spatially consistent and does not show any channel steepness variation across  
618 knickpoints in both longitudinal profiles and the  $\chi$ - $z$  plot (Figures 5b, 5d, 5f and S2) and hence cannot  
619 reflect changes in rock uplift rates.

620

## 621 **5.2 Topographic evolution of the Anti-Atlas**

622 A peculiarity of the Anti-Atlas topography is the occurrence of a low-relief topography at its  
623 maximum elevation plunging across and along strike over a wavelength of  $\sim 100$  km (Figure 2b, 2c)  
624 and  $\sim 600$  km (Figure 2e), respectively, which can be described as a topographic swell. It follows,  
625 that the high-standing relict landscape represents a warped geomorphic marker that can be used to  
626 document the spatial distribution of the recent increase in surface uplift rates. The along strike pattern  
627 of surface uplift ranges from  $\sim 500$  to 1100 m from the western to the central sector of AA (Figure 9),  
628 in agreement with the  $k_{sn}$  and elevation pattern of the most elevated non-lithological knickpoints. The  
629 paleo-landscape must have been characterized by a low-topographic relief with localized  $\sim 1000$ - to  
630 700-m-high mountain peaks in the central Anti-Atlas (NCAA, SCAA) and the WAA, respectively  
631 (Figure 10b and Table S4). These paleo-topographic heights correlate with high normalized channel  
632 steepness values observed for low erodibility lithologies, such as quartzite and meta-conglomerates  
633 (Figure S6; Clementucci et al., 2022).

634 The asymmetry of the AA flanks and the different locations of the highest knickpoints between the  
635 southern (SCAA) and northern flanks (NCAA) can be attributed to a faster knickpoints migration in  
636 the SCAA sector, as also suggested by the occurrence of quasi-equilibrium stream profiles (Figure

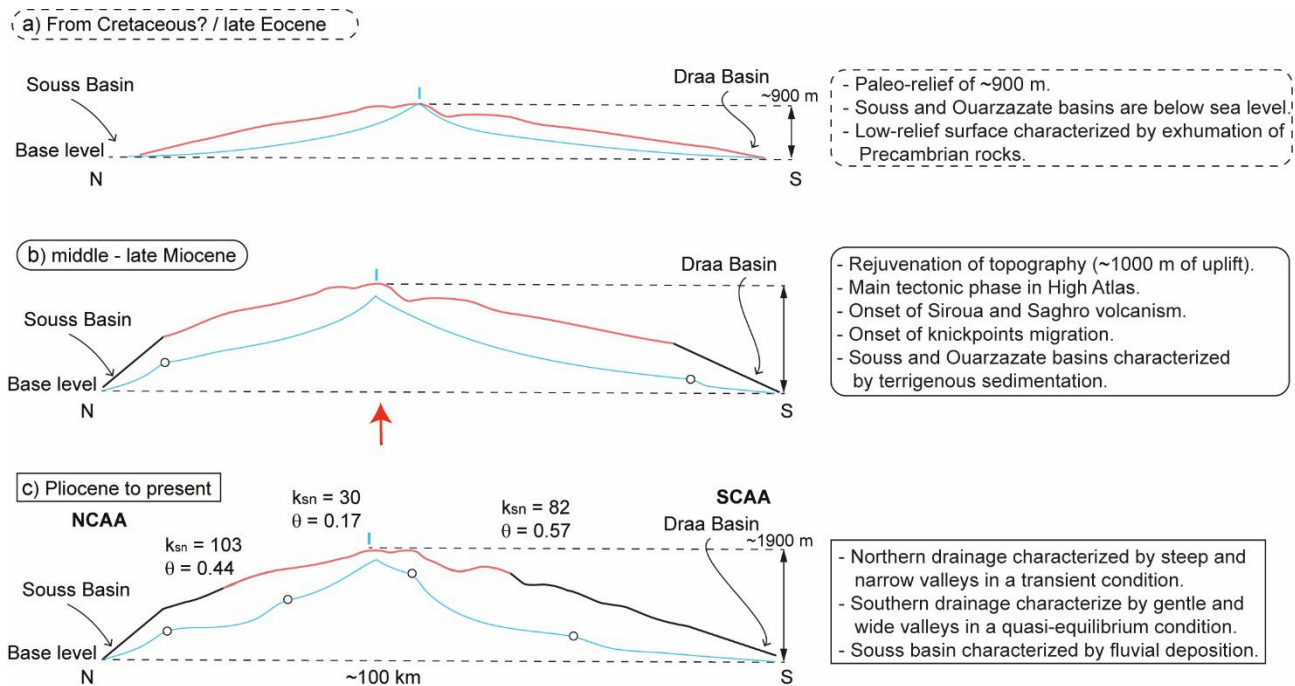
637 5e, 5f). Here, the presence of wide valleys sculptured on synclines within more erodible Paleozoic  
638 rocks (limestones, siltstones and shists) may have promoted an increase in the contributing drainage  
639 area and a faster knickpoint retreat (Figures 4b and S5b, S5c; Crosby and Whipple, 2006; Berlin and  
640 Anderson, 2007; Schwanghart and Scherler, 2020). Conversely, in the northern flank, the knickpoint'  
641 celerity is lower due to narrower and deeper valleys within less erodible late Precambrian carbonates  
642 (Figures 4a and 13c). This highlights the key role that rock strength plays in controlling the valley  
643 morphology, and in turn the location of genetically linked knickpoints (*e.g.*, Stokes et al., 2015).  
644 Importantly, for the NCAA and SCAA rivers, the migrating wave of transient erosion propagated for  
645 several kilometres within the Souss and Draa basins. These regions were likely characterized by  
646 erosional processes, before the onset of regional uplift (*e.g.*, Hssaine and Bridgland, 2009). This  
647 allows to dismiss a complex scenario with different erodibility parameters within the Neogene-  
648 Quaternary sediments in the basins. However, this would not represent an issue because the  
649 knickpoint would travel quickly in the mainstream of the Souss and Draa rivers due to the large  
650 drainage areas. The knickpoints propagation rate would have decreased one reached the upstream  
651 portions of the main mountain front (Crosby and Whipple, 2006; Schwanghart and Scherler, 2020).  
652 Hence, the time of residence in the Draa and Souss basins would be negligible. Finally, it should be  
653 noted that the occurrence of recent fluvial conglomerates, at high elevation in the major valleys of  
654 the northern flank (~700 m) and in the Souss alluvial plain, has been interpreted as an indication that  
655 uplift has decreased during the Quaternary (Lanari et al., 2022).

656

### 657 **5.3 Surface uplift history of Anti-Atlas**

658 The AA and surrounding basins (*e.g.*, Souss and Ouarzazate) were the southern shoulders of the  
659 Triassic-Jurassic rift (Lanari et al., 2020a) as documented by the absence of Mesozoic deposits older  
660 than Cretaceous and sediment provenance data (Domènech et al., 2018). During the Cenozoic, the  
661 Ouarzazate and Souss basins recorded marine sedimentation at least until the late Eocene, suggesting

662 that part of the study area must have been under sea level until 44 to 42 Ma (Figure 12a; El Harfi et  
 663 al., 2001; Teson et al., 2010; Hssaine and Bridgland, 2009).



664

665

666 **Figure 12.** Conceptual model depicting the Anti-Atlas topographic evolution across the central sector. (a)  
 667 Paleo-topography inferred until the late Eocene. (b) Topographic rejuvenation during the middle-late Miocene  
 668 associated with the initiation of river incision and knickpoints upstream propagation. (c) Present-day  
 669 configuration. At this stage, the first pattern of non-lithological knickpoints migrates upstream and a second  
 670 pattern lies a lower elevation. Pink and black lines describe the preserved relict and the rejuvenated landscape,  
 671 respectively. The blue line indicates the river profile.

672

673 In the AA, the presence of AHe cooling ages older than 70 Ma and consequently the low magnitude  
 674 of exhumation (< 2-3 km) over the same time interval suggests that the paleo-topography has been  
 675 developing at least since the late Cretaceous (Figure 12a; Gouiza et al., 2017; Lanari et al., 2020a;  
 676 Charton et al., 2021). Moreover, our observations and celerity calculations indicate that surface uplift  
 677 triggered the headward migration of the highest knickpoints starting from the middle-late Miocene  
 678 (Figures 11 and 13b). These new time constraints suggest average surface uplift rates ranging from  
 679 40 to 110 m/Myr (western sector) and from 70 to 180 m/Myr (central sector). These rates are based  
 680 on the celerity model (*i.e.*, the age of uplift initiation of  $9.9 \pm 4.1$  Ma) and hence are averaged over

681 time scales of 14 and 5.8 Ma, using the mean surface uplift values inferred from the river projections  
682 (Table S4).

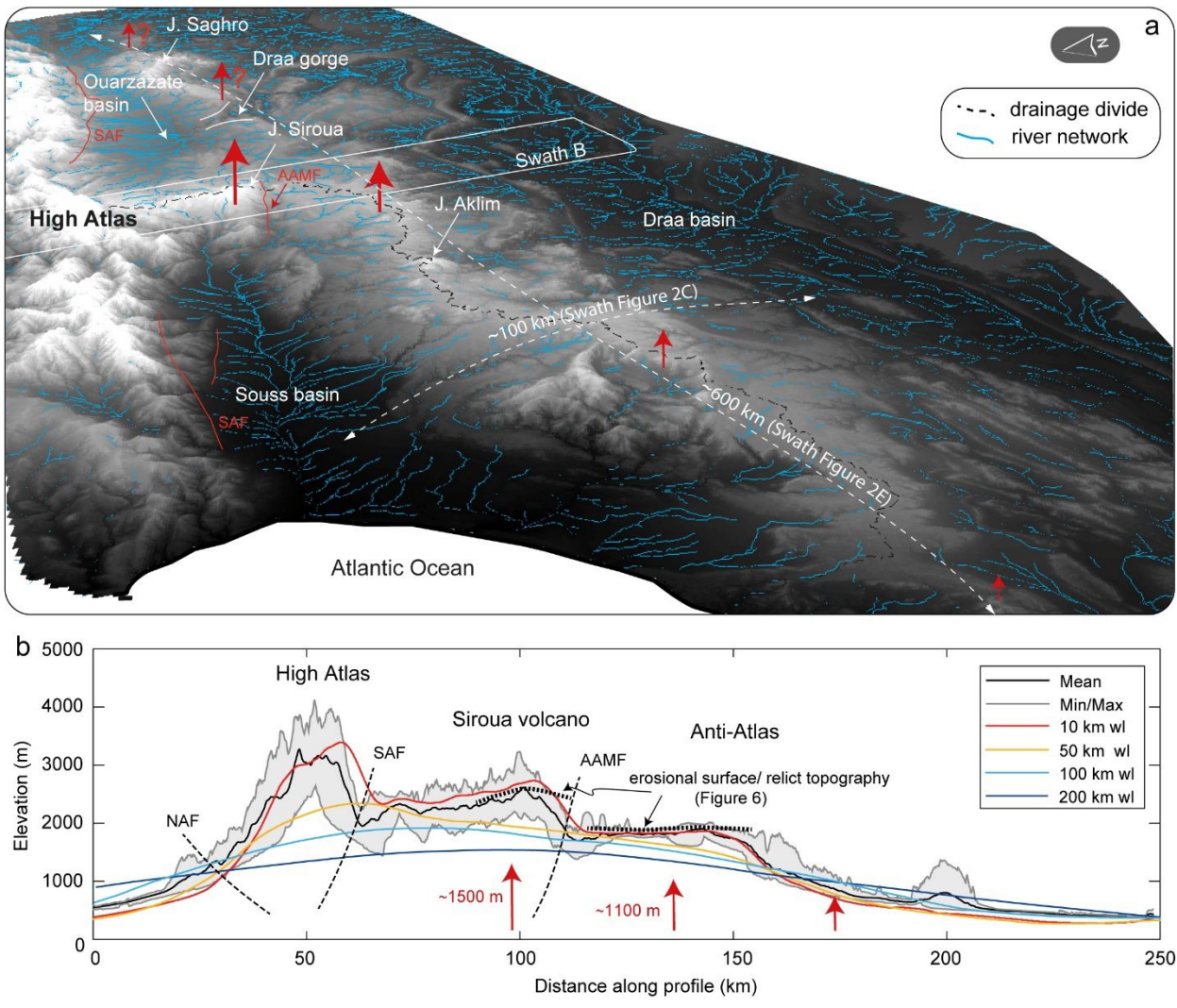
683 Downstream of non-lithological knickpoints, in the adjusted portion of the landscape, Clementucci et  
684 al., (2022) estimated Quaternary denudation rates of up to 50 m/Myr. These rates are consistent with  
685 the long-term rates inferred from the river projections averaged over the oldest age interval estimated  
686 from the celerity model (14-10 Ma). Uplift initiation at 14-10 Ma, would agree with the onset of  
687 volcanic activity in the Siroua Massif where more than 500 km<sup>2</sup> of crystalline basement are covered  
688 by 11-to 3-Myr-old lava flows (Figure 12b; Berrahma and Delaoye, 1989; Missenard et al., 2008).  
689 Moreover, this age estimates are consistent with the onset of clastic continental sedimentation in the  
690 Ouarzazate Basin during the Langhian (16-14 Ma) following an Oligocene to early Miocene  
691 sedimentary hiatus (El Harfi et al., 2001; Teson et al., 2010). Finally, the estimated time of  
692 topographic rejuvenation in the Anti-Atlas agrees with the onset of contractional deformation in the  
693 High Atlas Mountains, suggesting that there may a genetic link between the two events (Figure 12b;  
694 Lanari et al., 2020a). Overall, these observations suggest that the topographic rejuvenation started  
695 most likely at ~ 14-10 Ma.

696

#### 697 **5.4 Topographic evolution and surface uplift history of Siroua Massif**

698 The Siroua Massif is also characterized by a transient topography as documented by the high-standing  
699 basement representing the substratum of the Mio-Pliocene volcanic edifice (Figure 8; Missenard et  
700 al., 2008). Along the southern margin of the massif, this transient topography is delimited by a pattern  
701 of non-lithological knickpoints lying over 2000 m of elevation that on map view are subparallel to  
702 the AAMF and cluster along similar  $\chi$  values (Figure 8c). The projection of the stream profiles against  
703 the AAMF documents about 350 m of surface uplift in the hanging wall of the fault in response to  
704 fault activity (Figures 6a, 8c, 8d and 14). Furthermore, short- and long-term denudation rates,  
705 estimated from <sup>10</sup>Be cosmogenic concentration and eroded volcanic rocks from the Siroua Massif,

706 indicates averaged values of 40-50 m/Myr and 10-20 m/Myr in the adjusted topography downstream  
 707 and upstream of non-lithological knickpoints, respectively (Clementucci et al., 2022).



708  
 709 **Figure 13.** (a) Tridimensional view of the Anti-Atlas region. (b) Swath profile from north to south, showing  
 710 the local relief and maximum elevation of High Atlas, Siroua Massif and Anti-Atlas. wl: filtered topographic  
 711 windows. Note that the erosional surface of the Siroua Massif and the Anti-Atlas is standing at more than 2000  
 712 m and predated the onset of uplift in the Anti-Atlas and Siroua regions.

713  
 714 This suggests that the summit erosional surface of the AA must be the same surface underneath the  
 715 Siroua volcanic edifice that has been uplifted by the AAMF (Figures 8d and 14b). These conclusions  
 716 are also consistent with the occurrence of the same volcanic units at different elevations, in the  
 717 hanging wall and the footwall of the AAMF. Some of these lava flows are also exposed along the  
 718 steep landscape of the hanging wall of the AAMF downstream of the non-lithological knickpoints.

719 There, they present columnar jointed basalts orthogonal to the valley bottom, suggesting that the  
720 valley must have been a reference cooling surface at  $\sim 4$  Ma when the lava was emplaced (Figure 6d).  
721 Consequently, the transient fluvial incision associated with the activity of the AAMF must have  
722 started earlier than 4 Ma.

723 These data allow estimating the contribution of the different mechanisms that produced the modern  
724 elevation of  $\sim 3300$  m. Specifically the initial landscape could have been  $\sim 1000$  m of elevation, like  
725 the AA (see previous section), while the occurrence of basement rocks beneath the volcano at  $\sim 2500$   
726 m of elevation indicates that volcanic edifice contribute for  $\sim 800$  m high. By subtracting to the  
727 modern elevation, 1000 (paleo-topography) and 800 m (volcanic building), we can estimate a surface  
728 uplift for the Siroua Massif of  $\sim 1500$  m, where at least 350 meters result from the activity of the  
729 AAMF (Figure 13b). A fraction of this  $\sim 350$  m, however, may be associated with the injection of  
730 magma at depth as suggested by the dome-like geometry ( $\sim 50 \times 100$  km) of the basement beneath  
731 the Siroua volcano (Missenard et al., 2008). In conclusion, if we exclude the  $\sim 350$  m described above,  
732 the regional surface uplift in the Siroua Massif will be  $\sim 1150$  m in agreement with estimates from the  
733 central sectors of the Anti-Atlas.

734

## 735 **5.5 Causes of surface uplift and topographic expression of the Anti-Atlas and Siroua Massif**

736 The intracontinental orographic system of the Atlas Mountains represents a natural laboratory for  
737 studying the interaction between deep-seated, crustal, and surface processes. The amount of tectonic  
738 (crustal) shortening and thickening is limited and in the order of 12 to 35% in the central HA  
739 (Beauchamp et al., 1999; Gomez et al., 2000; Teixell et al., 2003; Domènech et al., 2016; Fekkak et  
740 al., 2018; Lanari et al., 2020b) and less than 10% in the MA (Gomez et al., 1998; Arboleya et al.,  
741 2004). Geophysical evidences, such as heat flow (Rimi et al., 1999; Teixell et al., 2005; Zeyen et al.,  
742 2005), gravity anomalies (Ayarza et al., 2005; Missenard et al., 2006), seismological constraints  
743 (Seber et al., 1996; Palomeras et al., 2013; Bezada et al., 2013; Miller and Becker, 2014; Spieker et  
744 al., 2014) and seismic reflection data (Ayarza et al., 2014) point toward an insufficient thickness of

745 the crust to explain the observed high topography and the anomalously thin lithosphere (~65 km).  
746 Geological and geomorphological constraints are consistent with these observations suggesting a  
747 contribution of deep-seated processes to the recent regional uplift (Babault et al., 2008;  
748 Benabdellouahed et al., 2017). Moreover, the late Miocene intraplate volcanism of the AA (Siroua  
749 and Saghro Massif) and MA is almost coeval with the main phase of regional uplift inferred in this  
750 study for the AA and from thermochronological data in the HA, indicating the occurrence of  
751 magmatism during mountain building processes (Berrahma & Delaloye, 1989; El Azzouzi et al.,  
752 1999; 2010).

753 The Atlas system displays short wavelength (10 – 50 km) topographic signals most likely linked to  
754 processes operating at crustal scale such as shortening (Teixell et al., 2003; Missenard et al., 2006;  
755 Faccenna and Becker, 2020) and long wavelength (> 100 km) signals associated with deeper  
756 processes (Figure 13b). Examples of the former and the latter include the HA Mountains and the  
757 Meseta, respectively, although multiple processes may concur to produce the observed topography  
758 (Teixell et al., 2003; Lanari et al., 2020a). Our study documents that the AA Mountains consists of a  
759 topographic swell that has an along- and across-strike wavelength of ~ 600 and 100 km, respectively  
760 and a maximum amplitude of ~1100 m (Figures 9b, 10a and 13). This is well underlined by the high-  
761 standing surface, which is warped along these two major directions (Figure 13a). The maximum  
762 values of surface uplift are observed in the central sector of the AA and appear to be slightly lower  
763 than those extracted from the adjacent Siroua Massif where surface uplift results from the sum of a  
764 long wavelength, regional uplift, and multiple crustal-scale signals such as faulting along the AAMF  
765 and possibly local magma injection. The occurrence of magma intrusions may be testified by the  
766 occurrence of a localized topographic bulge on the somital erosional surface of the Siroua that stands  
767 beneath the volcano. This would explain the short-wavelength topographic signal observed in figure  
768 13b (Missenard et al., 2008). Similar geomorphic expressions have been described in different  
769 settings where magma injection at variable depth in the crust generated a few hundred meters of uplift  
770 over different timescales (Singer et al., 2018; Townsend, 2022). This process could have also

771 occurred in the Saghro mountain peak of the eastern Anti-Atlas where a localized maximum  
772 topography associated with a few volcanic eruptions is observed (Figure 2e).

773 The long wavelength topographic swell (600 x 100 km) of the AA, however, still needs to be  
774 explained (Figure 13a). Tectonic uplift associated with faulting along a 600-km-long (along strike)  
775 crustal scale ramp appears to be unlikely because the AA domain has been tectonically quiescent  
776 throughout the entire Cenozoic (Frizon de Lamotte et al., 2009; Lanari et al., 2020a; Clementucci et  
777 al., 2022). Furthermore, to explain the ~100-km-long across strike wavelength, one would need a  
778 fault-bend-fold mechanisms with a deep flat rooted into the basement, a ramp, and a shallower flat  
779 accommodating at least 100 km of displacement. This appears to be quite unlikely, especially if one  
780 considers that the AA is a Variscan orogen and not an undisturbed sedimentary multi-layer that may  
781 have been detached along stratigraphic horizons. Furthermore, there are no evaporite layers in the pre  
782 Variscan sedimentary sequence that could accommodate such an amount of displacement, as  
783 observed in the adjacent HA (Lanari et al., 2020b). These observations suggest that the ~ 600 x 100  
784 km AA topographic swell could be only explained through deeper, mantle driven processes.

785 A major deep-seated mechanism, which has been invoked as main contributor in the construction of  
786 elevated orogenic plateaus is the delamination of the lithospheric mantle and possibly of the lower  
787 crust (*e.g.*, Garzzone et al., 2006; Hatzfeld and Molnar, 2010). This would change the density structure  
788 of lithosphere through the sinking of a relatively dense lithospheric mantle and the rise of a hotter and  
789 less dense asthenosphere. This hypothesis requires the occurrence of a previously thickened  
790 lithosphere, which does not appear to be the case for the AA where crustal shortening and thickening  
791 processes following the Variscan orogeny have been very limited (Burkhard et al., 2006). Moreover,  
792 the occurrence of a thickened lithosphere preceding mantle delamination would have produced  
793 subsidence and sedimentation before the onset of uplift (*e.g.*, DeCelles et al., 2009), and this is not  
794 supported by stratigraphic data, which suggest subaerial erosional conditions at least since the late  
795 Cretaceous (Gouiza et al., 2017; Charton et al., 2021). In intracontinental areas, another possible  
796 mechanism is the upwelling of asthenospheric mantle (Duggen et al., 2009; Faccenna et al., 2013;

797 Miller et al., 2013; Olivetti et al., 2016; Faccenna and Becker, 2020). Independently from the  
798 geodynamic setting and the main reasons for such a rise, the upward movement of hot asthenospheric  
799 mantle generates a deflection of the lithosphere in association with adiabatic melting and production  
800 of a magma with an alkaline signature (*e.g.*, Wilson and Downes, 1991; Gibson et al., 2006). This  
801 process will generate a strong positive free-air gravity anomaly (*e.g.*, McKenzie and Fairhead, 1997;  
802 Watts, 2001; Faccenna and Becker, 2020). This appears to be the case for the AA, where all  
803 observations are met (Berrahma and Delaloye, 1989; Spieker et al., 2014). Moreover, the wavelength  
804 recorded in the topography of the AA is compatible with other examples from the oceanic floor,  
805 where larger-scale swell signals have been observed (Hoggard et al., 2017; Cserepes et al., 2000).  
806 Tomography analysis also suggests mantle upwelling in NW Africa, which may be associated with  
807 plume activity recorded in the Atlantic Ocean in the Canary Islands (Duggen et al., 2009; Civiero et  
808 al., 2019). In conclusion, our topographic analysis indicates that the topography of the Anti-Atlas  
809 appears to be consistent with asthenospheric upwelling processes although the cause of these deep-  
810 seated mechanism and the possible genetic link with the Canary Islands remain still poorly  
811 understood.

812

### 813 **Conclusion**

814 Our study allows characterizing modern and past topography of the Anti-Atlas Mountains and  
815 inferring its surface uplift history. Specifically, it provides new constrains for deciphering the  
816 complex history of topographic growth resulting from the interplay between shallower and deep-  
817 seated processes. Here, we show that:

818 1) The landscape is in a transient state and exhibits a main pattern of elevated non-lithological  
819 knickpoints that mark a regional transition, from high to low values of topographic and channel  
820 metrics. The topography upstream of the non-lithological knickpoints can be described as an erosional  
821 surface (relict landscape) that plunges along and across strike. Our paleo-topographic reconstruction

822 suggests that such an erosional surface formed a subdued topography with a few local peaks in the  
823 order of  $\sim 1000$  m of elevation that started to develop from the late Cretaceous.

824 2) The magnitude of surface uplift increases along-strike from the western Anti-Atlas (500 m) to the  
825 central Anti-Atlas (1100 m) and the Siroua Massif (1500 m), where the latter represents a main Mio-  
826 Pliocene regional volcanic centre. Geometrically, the surface uplift can be described as  $\sim 600 \times 100$   
827 km swell. The initiation of knickpoints migration marks the onset of topographic rejuvenation and is  
828 estimated to be middle-late Miocene ( $9.9 \pm 4.1$  Ma). This is consistent with the middle-late Miocene  
829 initiation of a main tectonic phase in the High Atlas and with volcanism in the Siroua and the Saghro  
830 Massifs. Our data indicate that surface uplift occurred at rates ranging from 40-110 m/Myr to 70-180  
831 m/Myr (averaged over time scales of 14 and 5.8 Ma) from the western to the central Anti-Atlas. The  
832 lower range of uplift rates seems to be more likely because it agrees with rates derived from available  
833  $^{10}\text{Be}$  erosion rates. This observation, together with the aforementioned geological evidence, suggests  
834 that the initiation of surface uplift (i.e., the topographic rejuvenation) in the Anti-Atlas and the Siroua  
835 Massif occurred most likely at 14-10 Ma.

836 3) Surface uplift in the Siroua Massif is higher than in the Anti-Atlas because it results from the  
837 contribution of different processes, such as the long-wavelength regional component (i.e., the  
838 topographic swell;  $\sim 1150$  m), the growth of a volcanic edifice ( $\sim 800$  m), faulting along the Anti-  
839 Atlas Major Fault ( $\sim 350$  m) and possibly magma injection processes which cannot be easily  
840 quantified.

841 4) The long wavelength ( $\sim 600 \times 100$  km) topographic swell documented through the topographic  
842 analysis can be explained by upwelling of hot asthenosphere, which is also responsible for the  
843 generation of magmatism in the Siroua and Saghro Massif. Although the genesis of such a rise is  
844 unknown, it appears to be the only feasible mechanisms.

845

846 **Acknowledgments**

847 This study is part of the PhD thesis of RC at the University of Roma Tre (PhD Cycle XXXIV). It was  
848 supported by the PhD School of Roma Tre and grant “Vinci 2020” awarded to RC (Number: C2-  
849 1403). PB was supported by the MIUR (Ministry of Education University and Research), Excellence  
850 Department Initiative, Art. 1, com. 314-337, Law 232/2016. The ASTER (CEREGE, Aix-en-  
851 Provence) AMS national facility, is supported by the INSU/CNRS, and the IRD. We thank P-H Blard,  
852 S. Willett and T. Schildgen for revising this manuscript as a chapter of the PhD Thesis of the RC, to  
853 L. Benedetti, M. Della Seta, P. Molin and O. Bellier for providing valuable comments during the PhD  
854 defence of RC. The Supporting Information is available online (<https://osf.io/fnvke/>).

855

## 856 References

- 857 Ait Malek, H. A., Gasquet, D., Bertrand, J. M., & Leterrier, J. (1998). Géochronologie U-Pb sur zircon de  
858 granitoïdes éburnéens et panafricains dans les boutonnières protérozoïques d'Igherm, du Kerdous et  
859 du Bas Drâa (Anti-Atlas occidental, Maroc). *Comptes Rendus de l'Académie des Sciences-Series IIA-*  
860 *Earth and Planetary Science*, 327(12), 819-826. [https://doi.org/10.1016/S1251-8050\(99\)80056-1](https://doi.org/10.1016/S1251-8050(99)80056-1)
- 861 Arboleya, M. L., Teixell, A., Charroud, M., & Julivert, M. (2004). A structural transect through the High and  
862 Middle Atlas of Morocco. *Journal of African Earth Sciences*, 39(3-5), 319-327.  
863 <https://doi.org/10.1016/j.jafrearsci.2004.07.036>
- 864 Arboleya, M.-L., Babault, J., Owen, L. A., Teixell, A., & Finkel, R. C. (2008). Timing and nature of  
865 Quaternary fluvial incision in the Ouarzazate foreland basin, Morocco. *Journal of the Geological*  
866 *Society*, 165(6), 1059-1073. <https://doi.org/10.1144/0016-76492007-151>
- 867 Ayarza, P., Alvarez-Lobato, F., Teixell, A., Arboleya, M. L., Teson, E., Julivert, M., & Charroud, M. (2005).  
868 Crustal structure under the central High Atlas Mountains (Morocco) from geological and gravity  
869 data. *Tectonophysics*, 400(1-4), 67-84. <https://doi.org/10.1016/j.tecto.2005.02.009>
- 870 Azizi Samir, M. R., Ferrandini, J., & Tane, J. L. (1990). Tectonique et volcanisme tardi-Pan Africains (580-  
871 560 Ma) dans l'Anti-Atlas Central (Maroc): interprétation géodynamique à l'échelle du NW de  
872 l'Afrique. *Journal of African Earth Sciences*, 10(3), 549-563. [https://doi.org/10.1016/0899-](https://doi.org/10.1016/0899-5362(90)90105-N)  
873 [5362\(90\)90105-N](https://doi.org/10.1016/0899-5362(90)90105-N)

- 874 Babault, J., Teixell, A., Arboleya, M. L., & Charroud, M. (2008). A Late Cenozoic age for long-wavelength  
875 surface uplift of the Atlas Mountains of Morocco. *Terra nova*, 20(2), 102-107.  
876 <https://doi.org/10.1111/j.1365-3121.2008.00794.x>
- 877 Baldwin, J. A., Whipple, K. X., & Tucker, G. E. (2003). Implications of the shear stress river incision model  
878 for the timescale of postorogenic decay of topography. *Journal of Geophysical Research: Solid*  
879 *Earth*, 108(B3). <https://doi.org/10.1029/2001JB000550>.
- 880 Balestrieri, M. L., Moratti, G., Bigazzi, G., & Algouti, A. (2009). Neogene exhumation of the Marrakech  
881 High Atlas (Morocco) recorded by apatite fission - track analysis. *Terra Nova*, 21(2), 75-82.  
882 <https://doi.org/10.1111/j.1365-3121.2008.00857.x>
- 883 Ballato, P., Landgraf, A., Schildgen, T. F., Stockli, D. F., Fox, M., Ghassemi, M. R., Kirby, E., & Strecker,  
884 M. R. (2015). The growth of a mountain belt forced by base-level fall: Tectonics and surface  
885 processes during the evolution of the Alborz Mountains, N Iran. *Earth and Planetary Science*  
886 *Letters*, 425, 204-218. <https://doi.org/10.1016/j.epsl.2015.05.051>
- 887 Barbero, L., Teixell, A., Arboleya, M. L., del Río, P., Reiners, P. W., & Bougadir, B. (2007). Jurassic - to -  
888 present thermal history of the central High Atlas (Morocco) assessed by low - temperature  
889 thermochronology. *Terra Nova*, 19(1), 58-64. <https://doi.org/10.1111/j.1365-3121.2006.00715.x>
- 890 Baudon, C., Fabuel - Perez, I., & Redfern, J. (2009). Structural style and evolution of a Late Triassic rift  
891 basin in the central High Atlas, Morocco: Controls on sediment deposition. *Geological Journal*,  
892 44(6), 677-691. <https://doi.org/10.1002/gj.1195>
- 893 Beauchamp, W., Allmendinger, R. W., Barazangi, M., Demnati, A., El Alji, M., & Dahmani, M. (1999).  
894 Inversion tectonics and the evolution of the High Atlas Mountains, Morocco, based on a geological -  
895 geophysical transect. *Tectonics*, 18(2), 163-184. <https://doi.org/10.1029/1998TC900015>
- 896 Benabdellouahed, M., Klingelhoefer, F., Gutscher, M. A., Rabineau, M., Biari, Y., Hafid, M., Duarte J. C.,  
897 Schnabel M., Baltzer A., Pedoja K., Le Roy P., Reichert C., & Sahabi, M. (2017). Recent uplift of  
898 the Atlantic Atlas (offshore West Morocco): Tectonic arch and submarine  
899 terraces. *Tectonophysics*, 706, 46-58. <https://doi.org/10.1016/j.tecto.2017.03.024>

900 Berlin, M. M., & Anderson, R. S. (2007). Modeling of knickpoint retreat on the Roan Plateau, western  
901 Colorado. *Journal of Geophysical Research: Earth Surface*, 112(F3).  
902 <https://doi.org/10.1029/2006JF000553>

903 Berrahma, M., & Delaloye, M. (1989). Données géochronologiques nouvelles sur le massif volcanique du  
904 Siroua (Anti-Atlas, Maroc). *Journal of African Earth Sciences (and the Middle East)*, 9(3-4), 651-  
905 656. [https://doi.org/10.1016/0899-5362\(89\)90049-3](https://doi.org/10.1016/0899-5362(89)90049-3).

906 Berrahma, M. (1995). Etudes pétrologiques des laves récentes du massif du Siroua (Anti-Atlas, Maroc). Éd.  
907 du Service Géologique du Maroc.

908 Bezada, M. J., Humphreys, E. D., Davila, J. M., Carbonell, R., Harnafi, M., Palomeras, I., & Levander, A.  
909 (2014). Piecewise delamination of Moroccan lithosphere from beneath the Atlas  
910 Mountains. *Geochemistry, Geophysics, Geosystems*, 15(4), 975-985.  
911 <https://doi.org/10.1002/2013GC005059>

912 Burkhard, M., Caritg, S., Helg, U., Robert-Charrue, C., & Soulimani, A. (2006). Tectonics of the anti-Atlas  
913 of Morocco. *Comptes Rendus Geoscience*, 338(1-2), 11-24.  
914 <https://doi.org/10.1016/j.crte.2005.11.012>.

915 Calvet, M., Gunnell, Y., & Farines, B. (2015). Flat-topped mountain ranges: Their global distribution and  
916 value for understanding the evolution of mountain topography. *Geomorphology*, 241, 255-291.  
917 <https://doi.org/10.1016/j.geomorph.2015.04.015>

918 Charton, R., Bertotti, G., Arnould, A. D., Storms, J. E., & Redfern, J. (2021). Low-temperature  
919 thermochronology as a control on vertical movements for semi-quantitative source-to-sink analysis:  
920 A case study for the Permian to Neogene of Morocco and surroundings. *Basin Research*, 33(2),  
921 1337-1383. <https://doi.org/10.1111/bre.12517>

922 Choubert, G. (1952). Histoire géologique du domaine de l'Anti-Atlas. *Notes et Mém. Serv. Géol. Maroc*,  
923 (100), 77-172.

924 Civiero, C., Custódio, S., Rawlinson, N., Strak, V., Silveira, G., Arroucau, P., & Corela, C. (2019). Thermal  
925 nature of mantle upwellings below the Ibero-western Maghreb region inferred from teleseismic  
926 tomography. *Journal of Geophysical Research: Solid Earth*, 124(2), 1781-1801.  
927 <https://doi.org/10.1029/2018JB016531>

928 Clementucci, R., Ballato, P., Siame, L. L., Faccenna, C., Yaaqoub, A., Essaifi, A., Leanni, L., & Guillou, V.  
929 (2022). Lithological control on topographic relief evolution in a slow tectonic setting (Anti-Atlas,  
930 Morocco). *Earth and Planetary Science Letters*, 596, 117788.  
931 <https://doi.org/10.1016/j.epsl.2022.117788>.

932 Crosby, B. T., & Whipple, K. X. (2006). Knickpoint initiation and distribution within fluvial networks: 236  
933 waterfalls in the Waipaoa River, North Island, New Zealand. *Geomorphology*, 82(1-2), 16-38.  
934 <https://doi.org/10.1016/j.geomorph.2005.08.023>

935 Cserepes, L., Christensen, U. R., & Ribe, N. M. (2000). Geoid height versus topography for a plume model  
936 of the Hawaiian swell. *Earth and Planetary Science Letters*, 178(1-2), 29-38.  
937 [https://doi.org/10.1016/S0012-821X\(00\)00065-0](https://doi.org/10.1016/S0012-821X(00)00065-0)

938 De Beer, C. H., Chevallier, L. P., De Kock, G. S., Gresse, P. G., & Thomas, R. J. (2000). Mémoire explicatif  
939 de la carte géologique du Maroc au 1/50 000, Feuille Sirwa. *Notes Mem. Serv. Geol. Maroc*, 395, 86.

940 DeCelles, P. G., Ducea, M. N., Kapp, P., & Zandt, G. (2009). Cyclicality in Cordilleran orogenic  
941 systems. *Nature Geoscience*, 2(4), 251-257. <https://doi.org/10.1038/ngeo469>

942 DiBiase, R. A., & Whipple, K. X. (2011). The influence of erosion thresholds and runoff variability on the  
943 relationships among topography, climate, and erosion rate. *Journal of Geophysical Research: Earth*  
944 *Surface*, 116(F4). <http://dx.doi.org/10.1029/2011JF002095>.

945 Domènech, M., Teixell, A., Babault, J., & Arboleya, M. L. (2015). The inverted Triassic rift of the  
946 Marrakech High Atlas: A reappraisal of basin geometries and faulting histories. *Tectonophysics*, 663,  
947 177-191. <https://doi.org/10.1016/j.tecto.2015.03.017>

948 Domènech, M., Teixell, A., & Stockli, D. F. (2016). Magnitude of rift - related burial and orogenic  
949 contraction in the Marrakech High Atlas revealed by zircon (U - Th)/He thermochronology and  
950 thermal modeling. *Tectonics*, 35(11), 2609-2635. <https://doi.org/10.1002/2016TC004283>

951 Domènech, M., Stockli, D. F., & Teixell, A. (2018). Detrital zircon U-Pb provenance and palaeogeography  
952 of Triassic rift basins in the Marrakech High Atlas. *Terra Nova*, 30(4), 310-318.  
953 <https://doi.org/10.1111/ter.12340>

954 Duggen, S., Hoernle, K. A., Hauff, F., Kluegel, A., Bouabdellah, M., & Thirlwall, M. F. (2009). Flow of  
955 Canary mantle plume material through a subcontinental lithospheric corridor beneath Africa to the  
956 Mediterranean. *Geology*, 37(3), 283-286. <https://doi.org/10.1130/G25426A.1>

957 Duvall, A., Kirby, E., & Burbank, D. (2004). Tectonic and lithologic controls on bedrock channel profiles  
958 and processes in coastal California. *Journal of Geophysical Research: Earth Surface*, 109(F3).  
959 <https://doi.org/10.1029/2003JF000086>

960 El Azzouzi, M., Bellon, H., Maury, R. C., Pique, A., Cotten, J., Griffiths, J. B., ... & Hernandez, J. (1999).  
961 Evolution of the sources of Moroccan volcanism during the Neogene. *Comptes Rendus de l'Academie*  
962 *des Sciences. Serie 2, Sciences de la Terre et des Planetes*, 95-102.

963 El Azzouzi, M. H., Maury, R. C., Bellon, H., Youbi, N., Cotten, J., & Kharbouch, F. (2010). Petrology and  
964 K-Ar chronology of the Neogene-quaternary Middle Atlas basaltic province, Morocco. *Bulletin de la*  
965 *société géologique de France*, 181(3), 243-257. <https://doi.org/10.2113/gssgfbull.181.3.243>

966 El Harfi, A., Lang, J., Salomon, J., & Chellai, E. H. (2001). Cenozoic sedimentary dynamics of the  
967 ouarzazate foreland basin (Central High Atlas Mountains, Morocco). *International Journal of Earth*  
968 *Sciences*, 90, 393-411. <https://doi.org/10.1007/s005310000115>

969 England, P., & Molnar, P. (1990). Surface uplift, uplift of rocks, and exhumation of rocks. *Geology*, 18(12),  
970 1173-1177. [https://doi.org/10.1130/0091-7613\(1990\)018<1173:SUUORA>2.3.CO;2](https://doi.org/10.1130/0091-7613(1990)018<1173:SUUORA>2.3.CO;2)

971 Faccenna, C., Becker, T. W., Conrad, C. P., & Husson, L. (2013). Mountain building and mantle  
972 dynamics. *Tectonics*, 32(1), 80-93. <https://doi.org/10.1029/2012TC003176>

973 Faccenna, C., & Becker, T. W. (2020). Topographic expressions of mantle dynamics in the  
974 Mediterranean. *Earth-Science Reviews*, 103327. <https://doi.org/10.1016/j.earscirev.2020.103327>

975 Fekkak, A., Ouanaïmi, H., Michard, A., Soulaïmani, A., Ettachfini, E. M., Berrada, I., et al. (2018). Thick -  
976 skinned tectonics in a Late Cretaceous - Neogene intracontinental belt (High Atlas Mountains,  
977 Morocco): The flat - ramp fault control on basement shortening and cover folding. *Journal of African*  
978 *Earth Sciences*, 140, 169-188. <https://doi.org/10.1016/j.jafrearsci.2018.01.008>

979 Flint, J. J. (1974). Stream gradient as a function of order, magnitude, and discharge. *Water Resources*  
980 *Research*, 10, 969-973.

- 981 Forte, A. M., & Whipple, K. X. (2019). Short communication: The Topographic Analysis Kit (TAK) for  
982 TopoToolbox, *Earth Surface Dynamics*, 7, 87–95. <https://doi.org/10.5194/esurf-7-87-2019>.
- 983 Fox, M. (2019). A linear inverse method to reconstruct paleo-topography. *Geomorphology*, 337, 151-164.  
984 <https://doi.org/10.1016/j.geomorph.2019.03.034>
- 985 Fox, M., & Carter, A. (2020). How continuous are the “Relict” landscapes of Southeastern Tibet?. *Frontiers*  
986 *in Earth Science*, 8(587597). <https://doi.org/10.3389/feart.2020.587597>
- 987 Fraissinet, C., El Zouine, M., Morel, J. L., Poisson, A., Andrieux, J., & Faure-Muret, A. (1988). Structural  
988 evolution of the southern and northern central High Atlas in Paleogene and Mio-Pliocene times.  
989 In *The Atlas System of Morocco* (pp. 273-291). Springer, Berlin, Heidelberg.
- 990 Frizon de Lamotte, D., Saint Bezar, B., Bracène, R., & Mercier, E. (2000). The two main steps of the Atlas  
991 building and geodynamics of the western Mediterranean. *Tectonics*, 19, 740-761.  
992 <https://doi.org/10.1029/2000TC900003>
- 993 Frizon de Lamotte, D., Leturmy, P., Missenard, Y., Khomsi, S., Ruiz, G., Saddiqi, O., Guillocheau F., &  
994 Michard A. (2009). Mesozoic and Cenozoic vertical movements in the Atlas system (Algeria,  
995 Morocco, Tunisia). An overview: *Tectonophysics*. 475, 9-28.  
996 <https://doi.org/10.1016/j.tecto.2008.10.024>.
- 997 Froitzheim, N., Stets, J., & Wurster, P. (1988). Aspects of western High Atlas tectonics. In *The Atlas System*  
998 *of Morocco*, (pp. 219-244). Berlin: Springer.
- 999 Gallen, S. F., Wegmann, K. W., & Bohnenstiehl, D. R. (2013). Miocene rejuvenation of topographic relief in  
1000 the southern Appalachians. *GSA Today*, 23(2), 4-10. <https://doi.org/10.1130/GSATG163A.1>.
- 1001 Gallen, S. F., & Wegmann, K. W. (2017). River profile response to normal fault growth and linkage: An  
1002 example from the Hellenic forearc of south-central Crete, Greece. *Earth Surface Dynamics*, 5(1),  
1003 161-186. <https://doi.org/10.5194/esurf-5-161-2017>
- 1004 Gallen, S. F. (2018). Lithologic controls on landscape dynamics and aquatic species evolution in post-  
1005 orogenic mountains. *Earth and Planetary Science Letters*, 493, 150-160.  
1006 <https://doi.org/10.1016/j.epsl.2018.04.029>.

1007 Garzione, C. N., Molnar, P., Libarkin, J. C., & MacFadden, B. J. (2006). Rapid late Miocene rise of the  
1008 Bolivian Altiplano: Evidence for removal of mantle lithosphere. *Earth and Planetary Science*  
1009 *Letters*, 241(3-4), 543-556. <https://doi.org/10.1016/j.epsl.2005.11.026>

1010 Gasquet, D., Ennih, N., Liégeois, J. P., Soullaimani, A., & Michard, A. (2008). The pan-african belt.  
1011 In *Continental evolution: the geology of Morocco* (pp. 33-64). Springer, Berlin, Heidelberg.  
1012 [https://doi.org/10.1007/978-3-540-77076-3\\_2](https://doi.org/10.1007/978-3-540-77076-3_2)

1013 Ghorbal, B., Bertotti, G., Foeken, J., & Andriessen, P. (2008). Unexpected Jurassic to Neogene vertical  
1014 movements in 'stable' parts of NW Africa revealed by low temperature geochronology. *Terra*  
1015 *Nova*, 20(5), 355-363. <https://doi.org/10.1111/j.1365-3121.2008.00828.x>

1016 Gibson, S. A., Thompson, R. N., & Day, J. A. (2006). Timescales and mechanisms of plume–lithosphere  
1017 interactions:  $^{40}\text{Ar}/^{39}\text{Ar}$  geochronology and geochemistry of alkaline igneous rocks from the Paraná–  
1018 Etendeka large igneous province. *Earth and Planetary Science Letters*, 251(1-2), 1-17.  
1019 <https://doi.org/10.1016/j.epsl.2006.08.004>

1020 Gomez, F., Allmendinger, R., Barazangi, M., Er-Raji, A., & Dahmani, M. (1998). Crustal shortening and  
1021 vertical strain partitioning in the Middle Atlas Mountains of Morocco. *Tectonics*, 17(4), 520-533.  
1022 <https://doi.org/10.1029/98TC01439>

1023 Gomez, F., Beauchamp, W., & Barazangi, M. (2000). Role of the Atlas Mountains (northwest Africa) within  
1024 the African - Eurasian plate-boundary zone. *Geology*, 28(9), 775-778. [https://doi.org/10.1130/0091-7613\(2000\)28<775:ROTAMN>2.0.CO;2](https://doi.org/10.1130/0091-7613(2000)28<775:ROTAMN>2.0.CO;2)

1025

1026 Goren, L., Fox, M., & Willett, S. D. (2014). Tectonics from fluvial topography using formal linear inversion:  
1027 Theory and applications to the Inyo Mountains, California. *Journal of Geophysical Research: Earth*  
1028 *Surface*, 119(8), 1651-1681. <https://doi.org/10.1002/2014JF003079>

1029 Görler, K., Helmdach, F.-F., Gaemers, P., Heiig, K., Hinsch, W., Mdler, K., et al. (1988). The uplift of the  
1030 central High Atlas as deduced from Neogene continental sediments of the Ouarzazate province,  
1031 Morocco. In *The Atlas System of Morocco*, (pp. 359-404). Berlin: Springer.  
1032 <https://doi.org/10.1007/s00531-016-1325-0>

- 1033 Gouiza, M., Charton, R., Bertotti, G., Andriessen, P., & Storms, J. E. A. (2017). Post-Variscan evolution of  
1034 the Anti-Atlas belt of Morocco constrained from low-temperature geochronology. *International*  
1035 *Journal of Earth Sciences*, 106(2), 593-616.
- 1036 Guimerà, J., Arboleya, M. L., & Teixell, A. (2011). Structural control on present-day topography of a  
1037 basement massif: the Central and Eastern Anti-Atlas (Morocco). *Geologica Acta: an international*  
1038 *earth science journal*, 9(1), 55-65. <https://doi.org/10.1344/105.00.0001643>.
- 1039 Hack, J. T. (1957). *Studies of longitudinal stream profiles in Virginia and Maryland* (Vol. 294). US  
1040 Government Printing Office.
- 1041 Hafid, M. (2000). Triassic - early Liassic extensional systems and their Tertiary inversion, Essaouira Basin  
1042 (Morocco). *Marine and Petroleum Geology*, 17, 409-429. [https://doi.org/10.1016/S0264 -](https://doi.org/10.1016/S0264-8172(98)00081-6)  
1043 [8172\(98\)00081 - 6](https://doi.org/10.1016/S0264-8172(98)00081-6)
- 1044 Hancock, G., & Kirwan, M. (2007). Summit erosion rates deduced from <sup>10</sup>Be: Implications for relief  
1045 production in the central Appalachians. *Geology*, 35(1), 89-92. <https://doi.org/10.1130/G23147A.1>
- 1046 Harkins, N., Kirby, E., Heimsath, A., Robinson, R., & Reiser, U. (2007). Transient fluvial incision in the  
1047 headwaters of the Yellow River, northeastern Tibet, China. *Journal of Geophysical Research: Earth*  
1048 *Surface*, 112(F3). <https://doi.org/10.1029/2006JF000570>
- 1049 Hatzfeld, D., & Molnar, P. (2010). Comparisons of the kinematics and deep structures of the Zagros and  
1050 Himalaya and of the Iranian and Tibetan plateaus and geodynamic implications. *Reviews of*  
1051 *Geophysics*, 48(2). <https://doi.org/10.1029/2009RG000304>
- 1052 Hefferan, K. P., Admou, H., Karson, J. A., & Saquaque, A. (2000). Anti-atlas (Morocco) role in  
1053 neoproterozoic western Gondwana reconstruction. *Precambrian Research*, 103(1-2), 89-96.  
1054 [https://doi.org/10.1016/S0301-9268\(00\)00078-4](https://doi.org/10.1016/S0301-9268(00)00078-4)
- 1055 Heidarzadeh, G., Ballato, P., Hassanzadeh, J., Ghassemi, M. R., & Strecker, M. R. (2017). Lake overflow  
1056 and onset of fluvial incision in the Iranian Plateau: Insights from the Mianeh Basin. *Earth and*  
1057 *Planetary Science Letters*, 469, 135-147. <https://doi.org/10.1016/j.epsl.2017.04.019>
- 1058 Helg, U., Burkhard, M., Caritg, S., & Robert-Charrue, C. (2004). Folding and inversion tectonics in the anti-  
1059 Atlas of Morocco. *Tectonics*, 23(4). <https://doi.org/10.1029/2003TC001576>

1060 Hoggard, M. J., Winterbourne, J., Czarnota, K., & White, N. (2017). Oceanic residual depth measurements,  
1061 the plate cooling model, and global dynamic topography. *Journal of Geophysical Research: Solid*  
1062 *Earth*, 122(3), 2328-2372. <https://doi.org/10.1002/2016JB013457>.

1063 Hollard, H., Choubert, G., Bronner, G., Marchand, J., Sougy, J. (1985). Carte géologique du Maroc, scale 1:  
1064 1,000,000. *Serv. Carte géol. Maroc*. 260(2).

1065 Howard, A. D., & Kerby, G. (1983). Channel changes in badlands. *Geological Society of America*  
1066 *Bulletin*, 94(6), 739-752. [http://dx.doi.org/10.1130/0016-7606\(1983\)94<739:CCIB>2.0.CO;2](http://dx.doi.org/10.1130/0016-7606(1983)94<739:CCIB>2.0.CO;2).

1067 Howard, A. D. (1994). A detachment-limited model of drainage basin evolution. *Water resources*  
1068 *research*, 30(7), 2261-2285. <https://doi.org/10.1029/94WR00757>

1069 Hssaine, A. A., & Bridgland, D. (2009). Pliocene-Quaternary fluvial and aeolian records in the Souss Basin,  
1070 southwest Morocco: A geomorphological model. *Global and Planetary Change*, 68, 288-296.  
1071 <https://doi.org/10.1016/j.gloplacha.2009.03.002>

1072 Jansen, J. D., Codilean, A. T., Bishop, P., & Hoey, T. B. (2010). Scale dependence of lithological control on  
1073 topography: Bedrock channel geometry and catchment morphometry in western Scotland. *The*  
1074 *Journal of geology*, 118(3), 223-246. <https://doi.org/10.1086/651273>.

1075 Kirby, E., & Whipple, K. (2001). Quantifying differential rock-uplift rates via stream profile  
1076 analysis. *Geology*, 29(5), 415-418. [https://doi.org/10.1130/0091-](https://doi.org/10.1130/0091-7613(2001)029<0415:QDRURV>2.0.CO;2)  
1077 [7613\(2001\)029<0415:QDRURV>2.0.CO;2](https://doi.org/10.1130/0091-7613(2001)029<0415:QDRURV>2.0.CO;2).

1078 Kirby, E., & Whipple, K. X. (2012). Expression of active tectonics in erosional landscapes. *Journal of*  
1079 *Structural Geology*, 44, 54-75. <https://doi.org/10.1016/j.jsg.2012.07.009>.

1080 Lanari, R., Fellin, M. G., Faccenna, C., Balestrieri, M. L., Pazzaglia, F. J., Youbi, N., & Maden, C. (2020a).  
1081 Exhumation and surface evolution of the western high atlas and surrounding regions as constrained  
1082 by low-temperature thermochronology. *Tectonics*, 39(3), e2019TC005562.  
1083 <https://doi.org/10.1029/2019TC005562>

1084 Lanari, R., Faccenna, C., Fellin, M. G., Essaifi, A., Nahid, A., Medina, F., & Youbi, N. (2020b). Tectonic  
1085 evolution of the western high Atlas of Morocco: oblique convergence, reactivation, and  
1086 transpression. *Tectonics*, 39(3), e2019TC005563. <https://doi.org/10.1029/2019TC005563>

- 1087 Lanari, R., Reitano, R., Giachetta, E., Pazzaglia, F. J., Clementucci, R., Faccenna, C., & Fellin, M. G.  
1088 (2022). Is the Anti-Atlas of Morocco still uplifting?. *J. Afr. Earth. Sci.*, 188, 104481.  
1089 <https://doi.org/10.1016/j.jafrearsci.2022.104481>
- 1090 Leblanc, M. (1975). Ophiolites précambriennes et gites arseniés de cobalt: Bou Azzer (Maroc). *These*  
1091 *Doctorat d'Etat, Faculte des Science Paris VI, Memoires Centre Geologique et Geophysique.*
- 1092 Leprêtre, R., Missenard, Y., Barbarand, J., Gautheron, C., Jouvie, I., & Saddiqi, O. (2018). Polyphased  
1093 inversions of an intracontinental rift: Case study of the Marrakech High Atlas, Morocco. *Tectonics*,  
1094 37(3), 818-841. <https://doi.org/10.1002/2017TC004693>
- 1095 Malusa, M. G., Polino, R., Feroni, A. C., Ellero, A., Ottria, G., Baidder, L., & Musumeci, G. (2007). Post-  
1096 Variscan tectonics in eastern anti-atlas (Morocco). *Terra Nova*, 19(6), 481-489.  
1097 <https://doi.org/10.1111/j.1365-3121.2007.00775.x>
- 1098 Mandal, S. K., Lupker, M., Burg, J. P., Valla, P. G., Haghypour, N., & Christl, M. (2015). Spatial variability  
1099 of 10Be-derived erosion rates across the southern Peninsular Indian escarpment: A key to landscape  
1100 evolution across passive margins. *Earth and Planetary Science Letters*, 425, 154-167.  
1101 <https://doi.org/10.1016/j.epsl.2015.05.050>.
- 1102 McKenzie, D., & Fairhead, D. (1997). Estimates of the effective elastic thickness of the continental  
1103 lithosphere from Bouguer and free air gravity anomalies. *Journal of Geophysical Research: Solid*  
1104 *Earth*, 102(B12), 27523-27552. <https://doi.org/10.1029/97JB02481>.
- 1105 Miller, S. R., Baldwin, S. L., & Fitzgerald, P. G. (2012). Transient fluvial incision and active surface uplift in  
1106 the Woodlark Rift of eastern Papua New Guinea. *Lithosphere*, 4(2), 131-149.  
1107 <https://doi.org/10.1130/L135.1>
- 1108 Miller, S. R., Sak, P. B., Kirby, E., & Bierman, P. R. (2013). Neogene rejuvenation of central Appalachian  
1109 topography: Evidence for differential rock uplift from stream profiles and erosion rates. *Earth and*  
1110 *Planetary Science Letters*, 369, 1-12. <https://doi.org/10.1016/j.epsl.2013.04.007>
- 1111 Miller, M. S., & Becker, T. W. (2014). Reactivated lithospheric-scale discontinuities localize dynamic uplift  
1112 of the Moroccan Atlas Mountains. *Geology*, 42(1), 35-38. <https://doi.org/10.1130/G34959.1>.

- 1113 Miller, M. S., O'Driscoll, L. J., Butcher, A. J., & Thomas, C. (2015). Imaging Canary Island hotspot material  
1114 beneath the lithosphere of Morocco and southern Spain. *Earth and Planetary Science Letters*, 431,  
1115 186-194. <https://doi.org/10.1016/j.epsl.2015.09.026>
- 1116 Missenard, Y., Zeyen, H., Frizon de Lamotte, D., Leturmy, P., Petit, C., Sébrier, M., & Saddiqi, O. (2006).  
1117 Crustal versus asthenospheric origin of relief of the Atlas Mountains of Morocco. *Journal of*  
1118 *Geophysical Research: Solid Earth*, 111(B3). <https://doi.org/10.1029/2005JB003708>
- 1119 Missenard, Y., Saddiqi, O., Barbarand, J., Leturmy, P., Ruiz, G., El Haimer, F. Z., & Frizon de Lamotte, D.  
1120 (2008). Cenozoic denudation in the Marrakech High Atlas, Morocco: insight from apatite fission-  
1121 track thermochronology. *Terra Nova*, 20(3), 221-228. [https://doi.org/10.1111/j.1365-](https://doi.org/10.1111/j.1365-3121.2008.00810.x)  
1122 [3121.2008.00810.x](https://doi.org/10.1111/j.1365-3121.2008.00810.x).
- 1123 Missenard, Y., & Cadoux, A. (2012). Can Moroccan Atlas lithospheric thinning and volcanism be induced  
1124 by Edge-Driven Convection?. *Terra Nova*, 24(1), 27-33. [https://doi.org/10.1111/j.1365-](https://doi.org/10.1111/j.1365-3121.2011.01033.x)  
1125 [3121.2011.01033.x](https://doi.org/10.1111/j.1365-3121.2011.01033.x)
- 1126 Molnar, P., & England, P. (1990). Late Cenozoic uplift of mountain ranges and global climate change:  
1127 chicken or egg?. *Nature*, 346(6279), 29-34. <https://doi.org/10.1038/346029a0>
- 1128 Molnar, P. (2004). Late Cenozoic increase in accumulation rates of terrestrial sediment: How might climate  
1129 change have affected erosion rates?. *Annu. Rev. Earth Planet. Sci.*, 32, 67-89.  
1130 <https://doi.org/10.1146/annurev.earth.32.091003.143456>
- 1131 Montgomery, D. R., & Foufoula-Georgiou, E. (1993). Channel network source representation using digital  
1132 elevation models. *Water Resources Research*, 29(12), 3925-3934.  
1133 <https://doi.org/10.1029/93WR02463>
- 1134 Mudd, S. M., Attal, M., Milodowski, D. T., Grieve, S. W., & Valters, D. A. (2014). A statistical framework  
1135 to quantify spatial variation in channel gradients using the integral method of channel profile  
1136 analysis. *Journal of Geophysical Research: Earth Surface*, 119(2), 138-152.  
1137 <https://doi.org/10.1002/2013JF002981>
- 1138 Norton, K. P., von Blanckenburg, F., Schlunegger, F., Schwab, M., & Kubik, P. W. (2008). Cosmogenic  
1139 nuclide-based investigation of spatial erosion and hillslope channel coupling in the transient foreland

1140 of the Swiss Alps. *Geomorphology*, 95(3-4), 474-486.  
1141 <https://doi.org/10.1016/j.geomorph.2007.07.013>

1142 Olivetti, V., Cyr, A. J., Molin, P., Faccenna, C., & Granger, D. E. (2012). Uplift history of the Sila Massif,  
1143 southern Italy, deciphered from cosmogenic <sup>10</sup>Be erosion rates and river longitudinal profile  
1144 analysis. *Tectonics*, 31(3). <https://doi.org/10.1029/2011TC003037>

1145 Olivetti, V., Godard, V., Bellier, O., & ASTER team. (2016). Cenozoic rejuvenation events of Massif  
1146 Central topography (France): Insights from cosmogenic denudation rates and river profiles. *Earth  
1147 and Planetary Science Letters*, 444, 179-191. <https://doi.org/10.1016/j.epsl.2016.03.049>

1148 Palomeras, I., Thurner, S., Levander, A., Liu, K., Villaseñor, A., Carbonell, R., & Harnafi, M. (2014). Finite-  
1149 frequency Rayleigh wave tomography of the western Mediterranean: Mapping its lithospheric  
1150 structure. *Geochemistry, Geophysics, Geosystems*, 15(1), 140-160.  
1151 <https://doi.org/10.1002/2013GC004861>

1152 Pastor, A., Babault, J., Owen, L. A., Teixell, A., & Arboleya, M. L. (2015). Extracting dynamic topography  
1153 from river profiles and cosmogenic nuclide geochronology in the Middle Atlas and the High Plateaus  
1154 of Morocco. *Tectonophysics*, 663, 95-109. <https://doi.org/10.1016/j.tecto.2015.06.007>

1155 Perron, J. T., & Royden, L. (2013). An integral approach to bedrock river profile analysis. *Earth Surface  
1156 Processes and Landforms*, 38(6), 570-576. <https://doi.org/10.1002/esp.3302>.

1157 Piqué, A., & Michard, A. (1989). Moroccan Hercynides; a synopsis; the Paleozoic sedimentary and tectonic  
1158 evolution at the northern margin of West Africa. *American Journal of science*, 289(3), 286-330.  
1159 <https://doi.org/10.2475/ajs.289.3.286>

1160 Piqué, A., Bouabdelli, M., Soulaïmani, A., Youbi, N., & Illiani, M. (1999). Les conglomérats du PIII  
1161 (Protérozoïque terminal) de l'Anti-Atlas (Sud du Maroc): Molasses tardi-Panafricaines, ou marq n  
1162 rifting fini-Protérozoïque. *Comptes Rendus Académie Sciences Paris*, 328, 409-414.

1163 Racano, S., Schildgen, T. F., Cosentino, D., & Miller, S. R. (2021). Temporal and spatial variations in rock  
1164 uplift from river-profile inversions at the Central Anatolian Plateau southern margin. *Journal of  
1165 Geophysical Research: Earth Surface*, 126(8), e2020JF006027.  
1166 <https://doi.org/10.1029/2020JF006027>

- 1167 Rimi, A. (1999). Mantle heat flow and geotherms for the main geologic domains in Morocco. *International*  
1168 *Journal of Earth Sciences*, 88(3), 458-466. <https://doi.org/10.1007/s005310050278>
- 1169 Roberts, G. G., & White, N. (2010). Estimating uplift rate histories from river profiles using African  
1170 examples. *Journal of Geophysical Research: Solid Earth*, 115(B2).  
1171 <https://doi.org/10.1029/2009JB006692>
- 1172 Royden, L., & Taylor Perron, J. (2013). Solutions of the stream power equation and application to the  
1173 evolution of river longitudinal profiles. *Journal of Geophysical Research: Earth Surface*, 118(2),  
1174 497-518. <https://doi.org/10.1002/jgrf.20031>
- 1175 Safran, E. B., Bierman, P. R., Aalto, R., Dunne, T., Whipple, K. X., & Caffee, M. (2005). Erosion rates  
1176 driven by channel network incision in the Bolivian Andes. *Earth Surface Processes and Landforms:*  
1177 *The Journal of the British Geomorphological Research Group*, 30(8), 1007-1024.  
1178 <https://doi.org/10.1002/esp.1259>.
- 1179 Scharf, T. E., Codilean, A. T., De Wit, M., Jansen, J. D., & Kubik, P. W. (2013). Strong rocks sustain ancient  
1180 postorogenic topography in southern Africa. *Geology*, 41(3), 331-334.  
1181 <https://doi.org/10.1130/G33806.1>.
- 1182 Schildgen, T. F., Cosentino, D., Bookhagen, B., Niedermann, S., Yıldırım, C., Echtler, H., ... & Strecker, M.  
1183 R. (2012). Multi-phased uplift of the southern margin of the Central Anatolian plateau, Turkey: A  
1184 record of tectonic and upper mantle processes. *Earth and Planetary Science Letters*, 317, 85-95.  
1185 <https://doi.org/10.1016/j.epsl.2011.12.003>
- 1186 Schwanghart, W., & Scherler, D. (2014). TopoToolbox 2—MATLAB-based software for topographic  
1187 analysis and modeling in Earth surface sciences. *Earth Surface Dynamics*, 2(1), 1-7.  
1188 <https://doi.org/10.5194/esurf-2-1-2014>.
- 1189 Schwanghart, W., & Scherler, D. (2020). Divide mobility controls knickpoint migration on the Roan Plateau  
1190 (Colorado, USA). *Geology*, 48(7), 698-702. <https://doi.org/10.1130/G47054.1>
- 1191 Seber, D., Barazangi, M., Tadili, B. A., Ramdani, M., Ibenbrahim, A., & Ben Sari, D. (1996). Three-  
1192 dimensional upper mantle structure beneath the intraplate Atlas and interplate Rif mountains of  
1193 Morocco. *Journal of Geophysical Research: Solid Earth*, 101(B2), 3125-3138.  
1194 <https://doi.org/10.1029/95JB03112>

- 1195 Sébrier, M., Siame, L., Zouine, E. M., Winter, T., Missenard, Y., & Leturmy, P. (2006). Active tectonics in  
1196 the moroccan high atlas. *Comptes Rendus Geoscience*, 338(1-2), 65-79.  
1197 <https://doi.org/10.1016/j.crte.2005.12.001>.
- 1198 Sebti, S., Saddiqi, O., El Haimer, F. Z., Michard, A., Ruiz, G., Bousquet, R., Baidder, L., & de Lamotte, D.  
1199 F. (2009). Vertical movements at the fringe of the West African Craton: First zircon fission track  
1200 datings from the Anti-Atlas Precambrian basement, Morocco. *Comptes Rendus Geoscience*, 341(1),  
1201 71-77. <https://doi.org/10.1016/j.crte.2008.11.006>
- 1202 Sehrt, M., Glasmacher, U. A., Stockli, D. F., Jabour, H., & Kluth, O. (2018). The southern Moroccan passive  
1203 continental margin: An example of differentiated long-term landscape evolution in  
1204 Gondwana. *Gondwana Research*, 53, 129-144. <https://doi.org/10.1016/j.gr.2017.03.013>
- 1205 Sembroni, A., Molin, P., Pazzaglia, F. J., Faccenna, C., & Abebe, B. (2016). Evolution of continental-scale  
1206 drainage in response to mantle dynamics and surface processes: An example from the Ethiopian  
1207 Highlands. *Geomorphology*, 261, 12-29. <https://doi.org/10.1016/j.geomorph.2016.02.022>
- 1208 Sembroni, A., Molin, P., Soligo, M., Tuccimei, P., Anzalone, E., Billi, A., Franchini, S., Rinaldi, M., &  
1209 Tarchini, L. (2020). The uplift of the Adriatic flank of the Apennines since the Middle Pleistocene:  
1210 New insights from the Tronto River basin and the Acquasanta Terme Travertine (central Italy).  
1211 *Geomorphology*, 352, 106990. <https://doi.org/10.1016/j.geomorph.2019.106990>.
- 1212 Siame, L. L., Sébrier, M., Bellier, O., Bourlès, D., Costa, C., Ahumada, E. A., Gardini, C.E., & Cisneros, H.  
1213 (2015). Active basement uplift of Sierra Pie de Palo (Northwestern Argentina): rates and inception  
1214 from  $^{10}\text{Be}$  cosmogenic nuclide concentrations. *Tectonics*, 34(6), 1129-1153.  
1215 <https://doi.org/10.1002/2014TC003771>
- 1216 Singer, B. S., Le Mével, H., Licciardi, J. M., Córdova, L., Tikoff, B., Garibaldi, N., ... & Feigl, K. L. (2018).  
1217 Geomorphic expression of rapid Holocene silicic magma reservoir growth beneath Laguna del  
1218 Maule, Chile. *Science advances*, 4(6), eaat1513. <https://doi.org/10.1126/sciadv.aat1513>
- 1219 Siravo, G., Molin, P., Sembroni, A., Fellin, M. G., & Faccenna, C. (2021). Tectonically driven drainage  
1220 reorganization in the Eastern Cordillera, Colombia. *Geomorphology*, 389, 107847.  
1221 <https://doi.org/10.1016/j.geomorph.2021.107847>

- 1222 Smith, A. G., Fox, M., Schwanghart, W., & Carter, A. (2022). Comparing methods for calculating channel  
1223 steepness index. *Earth-Science Reviews*, 103970. <https://doi.org/10.1016/j.earscirev.2022.103970>
- 1224 Snyder, N. P., Whipple, K. X., Tucker, G. E., & Merritts, D. J. (2000). Landscape response to tectonic  
1225 forcing: Digital elevation model analysis of stream profiles in the Mendocino triple junction region,  
1226 northern California. *Geological Society of America Bulletin*, 112(8), 1250-1263.  
1227 [https://doi.org/10.1130/0016-7606\(2000\)112<1250:LRTTFD>2.0.CO;2](https://doi.org/10.1130/0016-7606(2000)112<1250:LRTTFD>2.0.CO;2)
- 1228 Soulaïmani, A., Bouabdelli, M., & Piqué, A. (2003). L'extension continentale au Néo-Protérozoïque  
1229 supérieur-Cambrien inférieur dans l'Anti-Atlas (Maroc). *Bulletin de la Société géologique de France*.
- 1230 Soulaïmani, A., & Burkhard, M. (2008). The Anti-Atlas chain (Morocco): the southern margin of the  
1231 Variscan belt along the edge of the West African Craton. *Geological Society, London, Special  
1232 Publications*, 297(1), 433-452. <https://doi.org/10.1144/SP297.20>
- 1233 Soulaïmani, A., Michard, A., Ouanaïmi, H., Baidder, L., Raddi, Y., Saddiqi, O., & Rjimati, E. C. (2014).  
1234 Late Ediacaran–Cambrian structures and their reactivation during the Variscan and Alpine cycles in  
1235 the Anti-Atlas (Morocco). *Journal of African Earth Sciences*, 98, 94-112.  
1236 <https://doi.org/10.1016/j.jafrearsci.2014.04.025>.
- 1237 Spieker, K., Wölbern, I., Thomas, C., Harnafi, M., & El Moudnib, L. (2014). Crustal and upper-mantle  
1238 structure beneath the western Atlas Mountains in SW Morocco derived from receiver  
1239 functions. *Geophysical Journal International*, 198(3), 1474-1485. <https://doi.org/10.1093/gji/ggu216>
- 1240 Stäblein, G. (1988). Geomorphological aspects of the Quaternary evolution of the Ouarzazate Basin,  
1241 southern Morocco. In *The Atlas System of Morocco* (pp. 433-444). Springer, Berlin, Heidelberg.  
1242 DOI: <https://doi.org/10.1007/BFb0011603>
- 1243 Stock, J. D., & Montgomery, D. R. (1999). Geologic constraints on bedrock river incision using the stream  
1244 power law. *Journal of Geophysical Research: Solid Earth*, 104(B3), 4983-4993.  
1245 <https://doi.org/10.1029/98JB02139>.
- 1246 Stock, J., & Dietrich, W. E. (2003). Valley incision by debris flows: Evidence of a topographic  
1247 signature. *Water Resources Research*, 39(4). <https://doi.org/10.1029/2001WR001057>
- 1248 Teixell, A., Arboleya, M. L., Julivert, M., & Charroud, M. (2003). Tectonic shortening and topography in the  
1249 central High Atlas (Morocco). *Tectonics*, 22(5). <https://doi.org/10.1029/2002TC001460>

1250 Teson, E., & Teixell, A. (2006). Sequence of thrusting and syntectonic sedimentation in the eastern Sub-  
1251 Atlas thrust belt (Dades and Mgoun valleys, Morocco). *International Journal of Earth*  
1252 *Sciences*, 97(1), 103-113. <https://doi.org/10.1007/s00531-006-0151-1>

1253 Tesón, E., Pueyo, E. L., Teixell, A., Barnolas, A., Agustí, J., & Furió, M. (2010). Magnetostratigraphy of the  
1254 Ouarzazate Basin: Implications for the timing of deformation and mountain building in the High  
1255 Atlas Mountains of Morocco. *Geodinamica Acta*, 23(4), 151-165. [https://doi.org/10.3166/ga.23.151-](https://doi.org/10.3166/ga.23.151-165)  
1256 [165](https://doi.org/10.3166/ga.23.151-165)

1257 Thomas, R. J., Chevallier, L. P., Gresse, P. G., Harmer, R. E., Eglington, B. M., Armstrong, R. A., de Beer,  
1258 C.H., Martini, J. E. J., Kock, G. S., Macey, P. H., & Ingram, B. A. (2002). Precambrian evolution of  
1259 the Sirwa window, Anti-Atlas orogen, Morocco. *Precambrian Research*, 118(1-2), 1-57.  
1260 [https://doi.org/10.1016/S0301-9268\(02\)00075-X](https://doi.org/10.1016/S0301-9268(02)00075-X)

1261 Torsvik, T. H., Rouse, S., Labails, C., & Smethurst, M. A. (2009). A new scheme for the opening of the  
1262 South Atlantic Ocean and the dissection of an Aptian salt basin. *Geophysical Journal*  
1263 *International*, 177(3), 1315-1333. <https://doi.org/10.1111/j.1365-246X.2009.04137.x>

1264 Townsend, M. (2022). Linking surface deformation to thermal and mechanical magma chamber  
1265 processes. *Earth and Planetary Science Letters*, 577, 117272.  
1266 <https://doi.org/10.1016/j.epsl.2021.117272>

1267 Tucker, G. E., & van Der Beek, P. (2013). A model for post-orogenic development of a mountain range and  
1268 its foreland. *Basin Research*, 25(3), 241-259. <https://doi.org/10.1111/j.1365-2117.2012.00559.x>

1269 Walsh, G. J., Aleinikoff, J. N., Benziane, F., Yazidi, A., & Armstrong, T. R. (2002). U–Pb zircon  
1270 geochronology of the Paleoproterozoic Tagragra de Tata inlier and its Neoproterozoic cover, western  
1271 Anti-Atlas, Morocco. *Precambrian Research*, 117(1-2), 1-20. [https://doi.org/10.1016/S0301-](https://doi.org/10.1016/S0301-9268(02)00044-X)  
1272 [9268\(02\)00044-X](https://doi.org/10.1016/S0301-9268(02)00044-X)

1273 [Watts, A. B. \(2001\). \*Isostasy and Flexure of the Lithosphere\*. Cambridge University Press.](https://doi.org/10.1016/S0301-9268(02)00044-X)

1274 West, A. J., Fox, M., Walker, R. T., Carter, A., Harris, T., Watts, A. B., & Gantulga, B. (2013). Links  
1275 between climate, erosion, uplift, and topography during intracontinental mountain building of the  
1276 Hangay Dome, Mongolia. *Geochemistry, Geophysics, Geosystems*, 14(12), 5171-5193.  
1277 <https://doi.org/10.1002/2013GC004859>

- 1278 Whipple, K. X., & Tucker, G. E. (1999). Dynamics of the stream-power river incision model: Implications  
1279 for height limits of mountain ranges, landscape response timescales, and research needs. *Journal of*  
1280 *Geophysical Research: Solid Earth*, 104(B8), 17661-17674. <https://doi.org/10.1029/1999JB900120>.
- 1281 Whipple, K. X., DiBiase, R. A., Ouimet, W. B., & Forte, A. M. (2017). Preservation or piracy: Diagnosing  
1282 low-relief, high-elevation surface formation mechanisms. *Geology*, 45(1), 91-94.  
1283 <https://doi.org/10.1130/G38490.1>
- 1284 Whittaker, A. C. (2012). How do landscapes record tectonics and climate?. *Lithosphere*, 4(2), 160-164.  
1285 <https://doi.org/10.1130/RF.L003.1>
- 1286 Willett, S. D., & Brandon, M. T. (2002). On steady states in mountain belts. *Geology*, 30(2), 175-178.  
1287 [https://doi.org/10.1130/0091-7613\(2002\)030<0175:OSSIMB>2.0.CO;2](https://doi.org/10.1130/0091-7613(2002)030<0175:OSSIMB>2.0.CO;2)
- 1288 Wilson, M., & Downes, H. (1991). Tertiary—Quaternary extension-related alkaline magmatism in western  
1289 and central Europe. *Journal of Petrology*, 32(4), 811-849. <https://doi.org/10.1093/petrology/32.4.811>
- 1290 Wobus, C., Whipple, K. X., Kirby, E., Snyder, N., Johnson, J., Spyropolou, K., Crosby, B., & Sheehan, D.  
1291 (2006). Tectonics from topography: Procedures, promise, and pitfalls. *Special papers-Geological*  
1292 *Society of America*, 398, 55. [https://doi.org/10.1130/2006.2398\(04\)](https://doi.org/10.1130/2006.2398(04))
- 1293 Wobus, C. W., Tucker, G. E., & Anderson, R. S. (2010). Does climate change create distinctive patterns of  
1294 landscape incision?. *Journal of Geophysical Research: Earth Surface*, 115(F4).  
1295 <https://doi.org/10.1029/2009JF001562>
- 1296 Yang, R., Willett, S. D., & Goren, L. (2015). In situ low-relief landscape formation as a result of river  
1297 network disruption. *Nature*, 520(7548), 526-529. <https://doi.org/10.1038/nature14354>
- 1298 Zeyen, H., Ayarza, P., Fernández, M., & Rimi, A. (2005). Lithospheric structure under the western African-  
1299 European plate boundary: A transect across the Atlas Mountains and the Gulf of Cadiz. *Tectonics*,  
1300 24(2). <https://doi.org/10.1029/2004TC001639>

***Tectonics***1#2 Supporting Information for**Surface uplift and topographic rejuvenation of a tectonically inactive range: Insights from Anti-Atlas and Siroua Massif (Morocco)**

Clementucci R.<sup>1,2</sup>, Ballato P.<sup>1</sup>, Siame L.<sup>2</sup>, Fox M.<sup>3</sup>, Lanari R.<sup>1,4</sup>, Sembroni A.<sup>1</sup>, Faccenna C.<sup>1,5</sup>, Yaaqoub A.<sup>6</sup>, Essaifi A.<sup>6</sup>

<sup>1</sup> Dipartimento di Scienze, Università Roma Tre, Largo San Leonardo Murialdo 1, 00146 Rome, Italy.

<sup>2</sup> Aix-Marseille Univ., CNRS, IRD, INRAE, Collège de France, CEREGE, Aix-en Provence, France.

<sup>3</sup> Department of Earth Sciences, University College London, Gower Street, London, WC1E 6BT, United Kingdom.

<sup>4</sup> Dipartimento di scienze, Università di Firenze, Italia.

<sup>5</sup> GFZ-German Research Centre for Geosciences, Potsdam, Germany.

<sup>6</sup> Département de Géologie, FSSM, B.P. 2390, Université Cadi Ayyad, Marrakech, Morocco.

**Contents of this file**

Figures S1 to S7

**Introduction**

The supporting information provided in this file (named 1#2) are complemented by additional tables reported in another supporting file (named 2#2). The data reported here comprise:

- Figures S1 and S2 provide a conceptual framework for the distribution of knickpoints in the Anti-Atlas and for the interpretation of the knickpoints in the river longitudinal profiles and the  $\chi$  versus elevation plot.
- Figure S3 and S5 report additional data concerning the knickpoint and river profile analysis presented in the main text.
- Figure S4 provides estimates of the erodibility parameters, used to constraint the knickpoints celerity model.

- Figure S6 provide the normalized channel steepness map to constraints the linear inverse model (2D river projection).
- Figure S7 provide the information about the cosmogenic nuclides data from Clementucci et al., 2022.

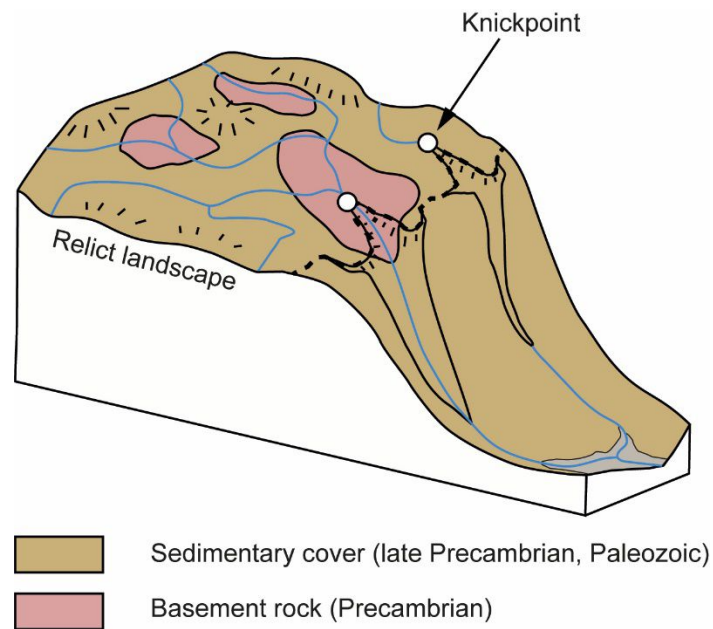


**Figure S1.** Cartoon of the Anti-Atlas topography. The major lithological contrast is between crystalline/ metamorphic Precambrian rock and late Precambrian/ Paleozoic sedimentary cover.

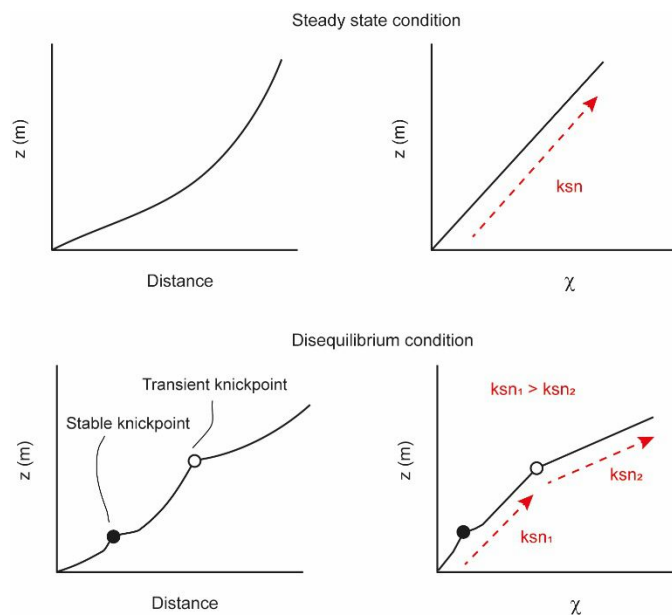


**Figure S2.** The simplified sketch of longitudinal river profiles (to the left) and  $\chi$ -plot (to the right) in a steady-state condition and disequilibrium state. In a steady-state condition, the river can be well explained by a single value of  $k_{sn}$ , thus a straight line in a  $\chi$  space (top). In a disequilibrium condition, the river is characterized by knickpoints. The transient knickpoints show an abrupt break in the  $\chi$ -plot reflected the variation of rock uplift. Whereas the stable knickpoints (lithological, dam, landslide, local heterogeneities, or climate related) is not characterized by  $k_{sn}$  variation in along the profile.

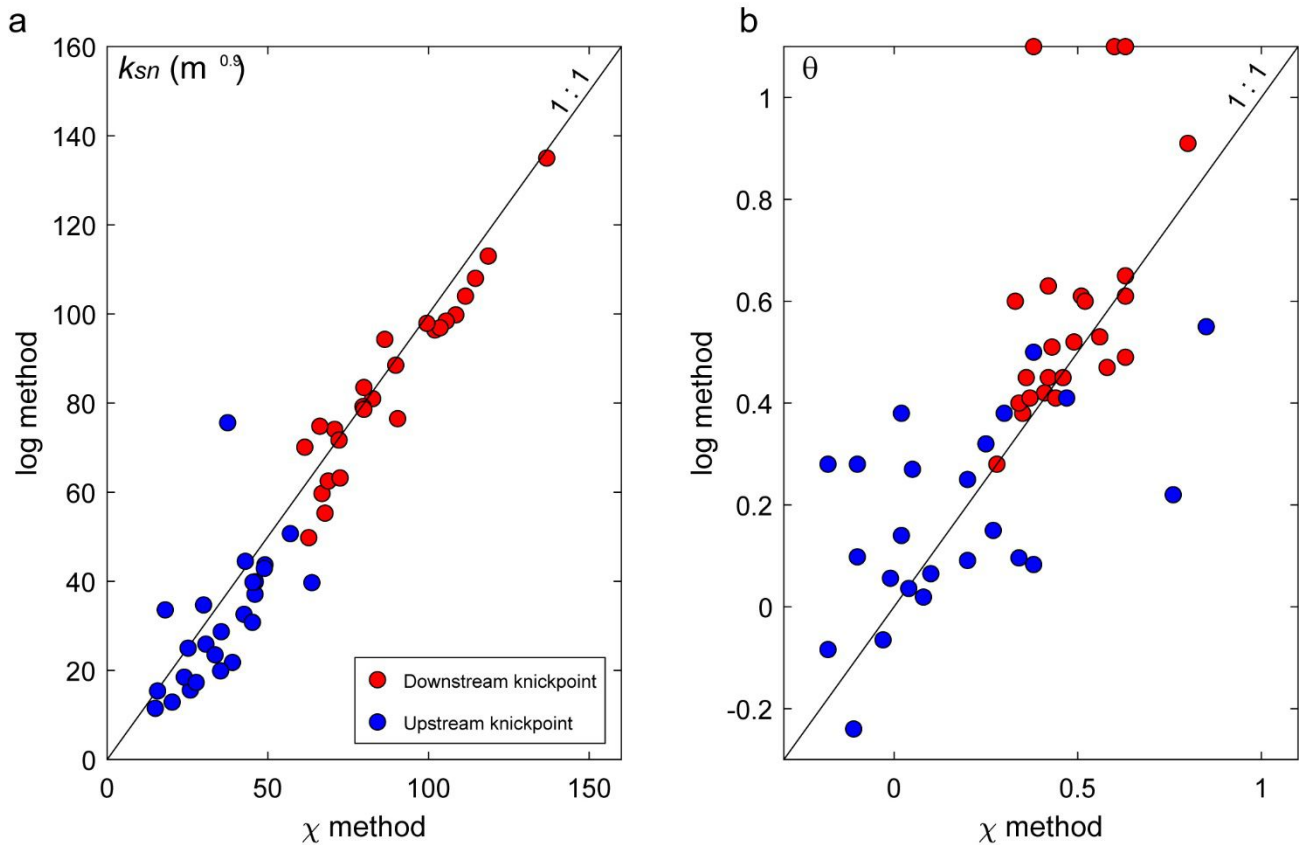


**Figure S3.** Comparison normalized channel steepness ( $k_{sn}$ ) and concavity values ( $\theta$ ) using the logS-logA method and integration method ( $\chi$ ). Note the  $k_{sn}$  values approximately follow the 1:1 line (plot to left), whereas the concavity values are more scattered (plot to right).

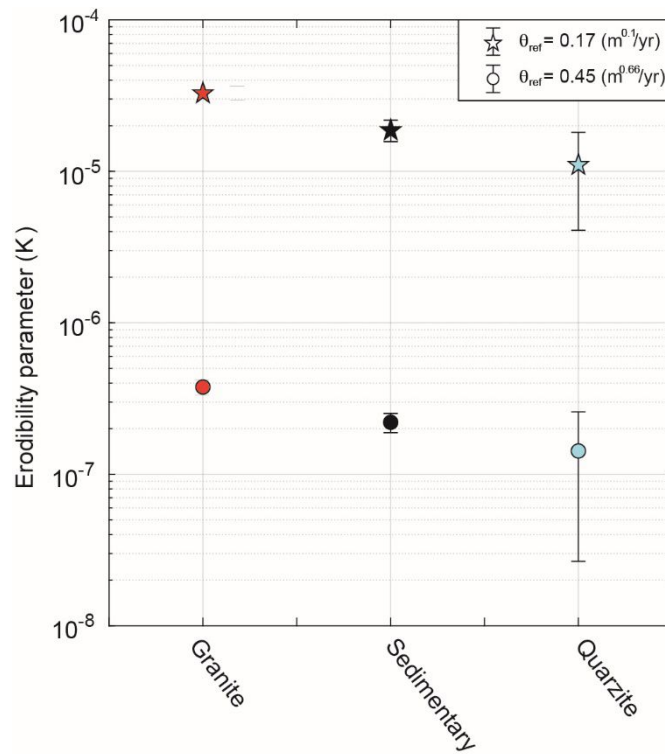


**Figure S4.** Rock-type versus erodibility parameter. Erodibility values were estimate from the forced linear regression between basin-wide denudation rates and basin-averaged  $k_{sn}$  using  $\theta_{ref}$  of 0.45 and 0.17 (mean value of concavity relative to uplifted relict landscape, Table S1), assuming  $n = 1$ .

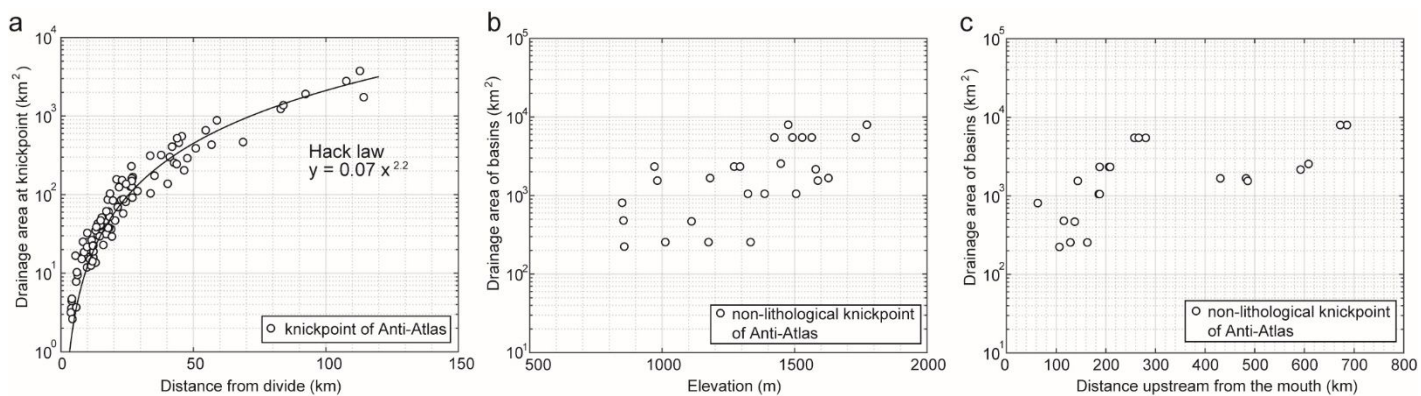


**Figure S5.** (a) Distance from divide versus upstream area at knickpoints location. Best-fit regression confirm the power law relation of Hack law for knickpoints in the study area. (b) Elevation of knickpoints versus drainage area of basins calculating at 500 m of elevation. (c) Distance from mouth of knickpoints versus drainage area of basins calculating at 500 m of elevation.

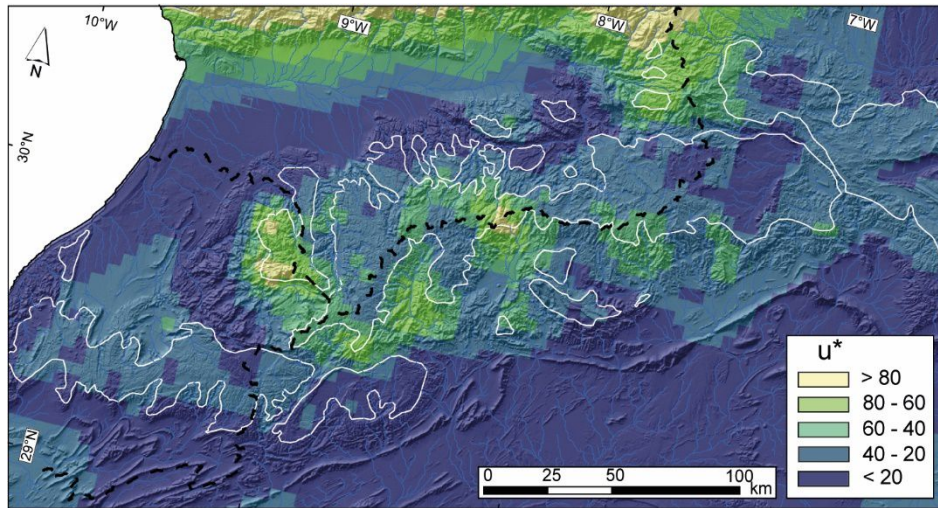


**Figure S6.** Normalized rock uplift rate ( $u^*$  or  $k_{sn}$ , using  $\theta_{ref} = 0.45$ ) map relative to the high-standing relict landscape (white polygons).

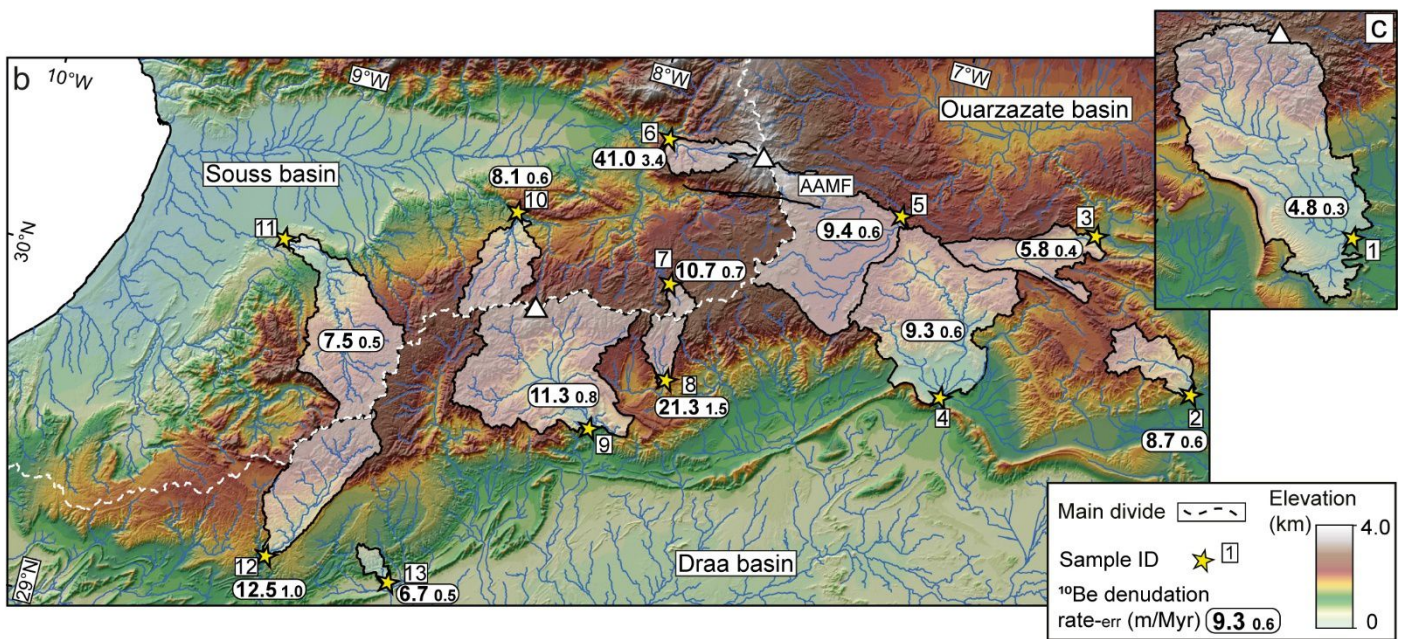
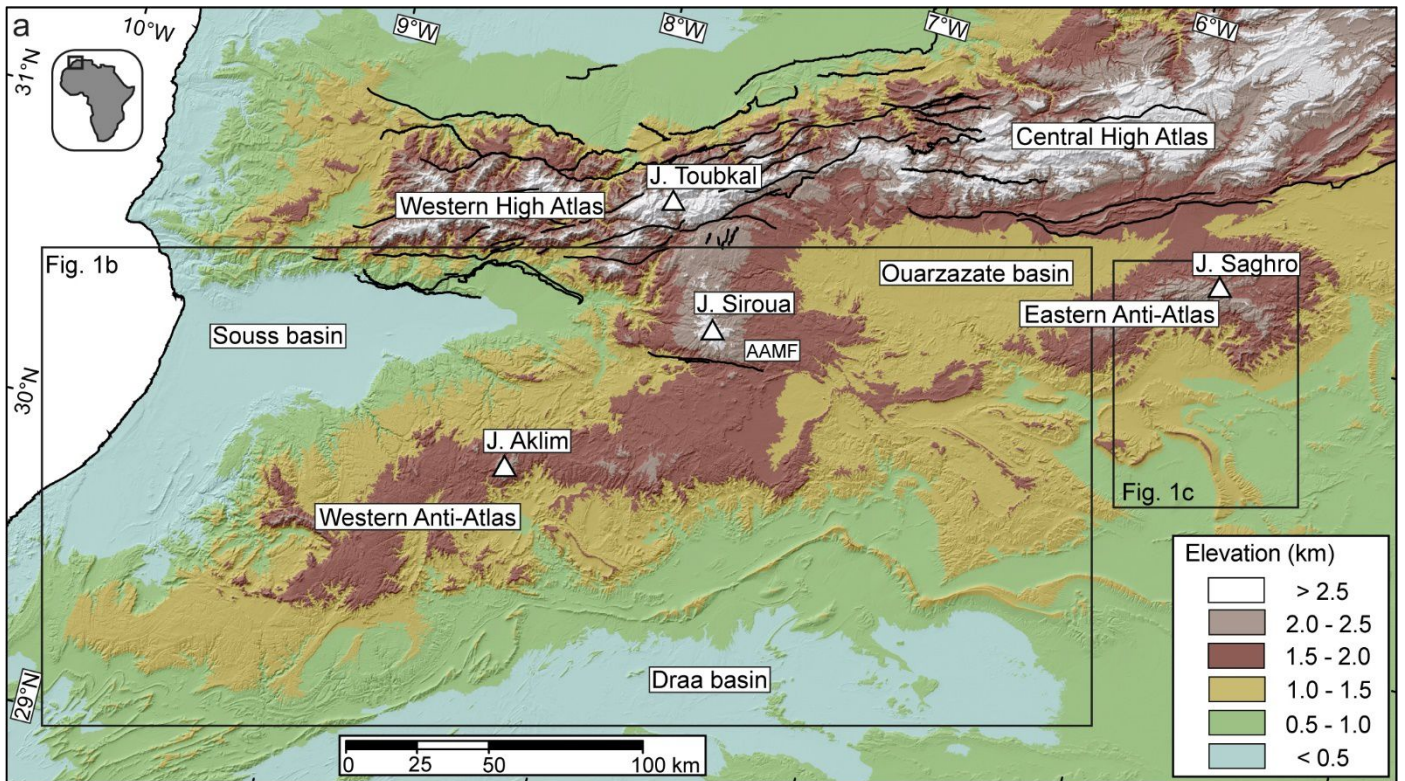


**Figure S7.** (a) Digital elevation model of the High Atlas and the Anti-Atlas Mountains (SRTM DEM, pixel size 90 m). The black lines are the major tectonic lineaments. (b-c) Topographic map of the Anti-

Atlas and the Siroua Massif, with  $^{10}\text{Be}$  sampling locations. The white polygons are the limits of the sampled catchments (Clementucci et al., 2022). The sample ID is used in Table S5 of the supplementary material. AAMF: Anti-Atlas Major Fault.

## References

- Clementucci, R., Ballato, P., Siame, L. L., Faccenna, C., Yaaqoub, A., Essaifi, A., Leanni, L., & Guillou, V. (2022). Lithological control on topographic relief evolution in a slow tectonic setting (Anti-Atlas, Morocco). *Earth and Planetary Science Letters*, 596, 117788. <https://doi.org/10.1016/j.epsl.2022.117788>

***Tectonics***2#2 Supporting Information for**Surface uplift and topographic rejuvenation of a tectonically inactive range: Insights from Anti-Atlas and Siroua Massif (Morocco)**

Clementucci R.<sup>1,2</sup>, Ballato P.<sup>1</sup>, Siame L.<sup>2</sup>, Fox M.<sup>3</sup>, Lanari R.<sup>1,4</sup>, Sembroni A.<sup>1</sup>, Faccenna C.<sup>1,5</sup>, Yaaqoub A.<sup>6</sup>, Essaifi A.<sup>6</sup>

<sup>1</sup> Dipartimento di Scienze, Università Roma Tre, Largo San Leonardo Murialdo 1, 00146 Rome, Italy.

<sup>2</sup> Aix-Marseille Univ., CNRS, IRD, INRAE, Collège de France, CEREGE, Aix-en Provence, France.

<sup>3</sup> Department of Earth Sciences, University College London, Gower Street, London, WC1E 6BT, United Kingdom.

<sup>4</sup> Dipartimento di scienze, Università di Firenze, Italia.

<sup>5</sup> GFZ-German Research Centre for Geosciences, Potsdam, Germany.

<sup>6</sup> Département de Géologie, FSSM, B.P. 2390, Université Cadi Ayyad, Marrakech, Morocco.

**Contents of this file**

Tables S1 to S5

**Introduction**

The supporting information provided in this file (named 2#2) are complemented by additional figures reported in another supporting file (named 1#2). The data reported here comprise:

- Tables S1 and S2 contain the results of the knickpoint and river profiles of the Anti-Atlas.
- Table S3 summarizes the results of the knickpoints celerity model.
- Table S4 summarizes the results of the 1D river projections.

- Table S5 provides the maximum excavation time estimated from basin-wide denudation rates from Clementucci et al., 2022.

**Table S1.** Non-lithological knickpoint and river profile data from log-log of channel slope vs. drainage area.

Stream <sup>a</sup>	Long.	Lat.	Elevation	DFD <sup>b</sup>	DFM <sup>c</sup>	Drainage area	Stream parameters			
							Downstream		Upstream	
	°W	°N	(m)	(m)	(m)	(m <sup>2</sup> )	$k_{sn}$ (m <sup>0.9</sup> ) <sup>f</sup>	$\theta^g$	$k_{sn}$ (m <sup>0.9</sup> )	$\theta$
NCAA1	637465.1	3379132.5	1731	20354	280487	1.58E+08	108 ± 2	0.45 ± 0.15	11.5 ± 2.4	0.27 ± 0.09
NCAA2	613556.8	3372613.8	1424	56831	257482	4.33E+08	113 ± 3	0.47 ± 0.18	32.6 ± 2.9	0.056 ± 0.14
NCAA3	608426.8	3354013.8	1565	23537	266134	1.42E+08	99.8 ± 2.8	0.51 ± 0.13	28.7 ± 1.5	0.32 ± 0.084
NCAA4	596666.8	3351313.8	1492	18508	257691	1.03E+08	104 ± 3	0.42 ± 0.11	44.5 ± 1.2	0.38 ± 0.17
NCAA5	589316.8	3345523.8	1529	11566	266423	2.64E+07	76.5 ± 8	0.28 ± 0.085	34.7 ± 2.6	0.096 ± 0.13
NCAA6	561056.8	3341233.8	1506	13041	185763	3.52E+07	96.4 ± 2.4	0.52 ± 0.092	37.1 ± 2.5	0.25 ± 0.13
NCAA7	555176.8	3340753.8	1324	16987	185931	4.73E+07	98.4 ± 1.6	0.38 ± 0.093	39.7 ± 4.3	0.083 ± 0.11
NCAA8	550076.8	3341713.8	1387	20427	187603	4.69E+07	96.9 ± .7	0.4 ± 0.089	21.8 ± 2.2	0.28 ± 0.11
NCAA9	543836.8	3339913.8	1334	21396	162843	69549300	97.9 ± 2.8	0.53 ± 0.39	30.8 ± 4.8	-0.084 ± 0.14
NCAA10	525536.8	3328513.8	1175	24446	128875	80991900	135 ± 5	0.45 ± 0.34	50.7 ± 3.7	0.15 ± 0.11
Mean NCAA <sup>d</sup>							102.6 ± 4.7	0.44 ± 0.02	33.2 ± 3.5	0.18 ± 0.04
$\sigma^e$							14.8	0.07	11.1	0.14
WAA1	497197.4	3309532.6	1111	15696	137453	54819423	70.1 ± 3.8	1.1 ± 0.3	75.6 ± 3.2	0.55 ± 0.077
WAA2	443907.4	3255074.6	857	25669	106609	1.49E+08	71.7 ± 6.4	0.91 ± 0.3	42.9 ± 4.6	-0.065 ± 0.19
WAA3	433249.4	3252884.6	849	29224	62967	1.11E+08	78.6 ± 2.3	1.1 ± 0.78	19.9 ± 2.8	0.098 ± 0.094
WAA4	422883.4	3241277.6	854	11251	115444	12464531	49.8 ± 1.4	0.6 ± 0.079	25.9 ± 1.2	0.38 ± 0.31
WAA5	428504.4	3236605.6	1012	12228	128546	22472393	55.3 ± 4.1	1.1 ± 0.17	12.9 ± 1.3	0.28 ± 0.2
WAA6	445513.4	3233028.6	982	14909	143614	29352132	74.8 ± 1.1	0.49 ± 0.087	39.8 ± 7.9	0.055 ± 0.13
WAA7	471939.4	3246752.6	1272	10221	206751	30897542	59.7 ± 0.7	0.41 ± 0.037	25 ± 5.6	-0.24 ± 0.41
WAA8	482670.4	3251424.6	1294	11699	208687	33460791	62.5 ± 0.7	0.45 ± 0.057	33.6 ± 5	0.019 ± 0.15
WAA9	483765.4	3234050.6	971	43222	187564	2.55E+08	63.2 ± 0.8	0.63 ± 0.18	23.5 ± 1.8	0.14 ± 0.11
Mean WAA							65.07 ± 3.1	0.75 ± 0.1	33.23 ± 6.1	0.14 ± 0.07
$\sigma$							9.45	0.3	18.5	0.22
SCAA1	497927.4	3246825.6	1181	27564	430725	1.62E+08	81 ± 1.6	0.61 ± 0.19	15.6 ± 2.4	0.22 ± 0.091

SCAA2	520922.4	3281573.6	1628	14831	482538	39338678	79.2 ± 0.8	0.5 ± 0.066	18.5 ± 2.9	0.036 ± 0.19
SCAA4	529390.4	3272156.6	1588	6291	485819	9485620	75.3 ± 2.2	0.66 ± 0.12	8.44 ± 3.8	0.041 ± 0.4
SCAA5	549465.4	3322015.6	1580	12837	592340	32309727	94.3 ± 0.9	0.41 ± 0.065	17.3 ± 1.2	0.41 ± 0.073
SCAA6	564284.4	3324643.6	1448	17885	608379	1.51E+08	83.5 ± 2.2	0.6 ± 0.13	43.7 ± 1.5	0.5 ± 0.1
SCAA7	618961.4	3336542.6	1773	13358	685609	21443896	88.5 ± 2	0.61 ± 0.089	15.4 ± 3.8	0.065 ± 0.17
SCAA8	636992.4	3343550.6	1476	22860	672273	86074008	74.1 ± 2	0.65 ± 0.13	39.9 ± 3.8	0.091 ± 0.11
Mean SCAA							82.2 ± 2.7	0.57 ± 0.03	22.7 ± 5.1	0.17 ± 0.07
σ							7.2	0.09	13.5	0.2
Mean tot							84.1 ± 3.8	0.58 ± 0.04	30.4 ± 2.9	0.17 ± 0.03
σ							19.7	0.22	14.8	0.18

<sup>a</sup> **NCAA**: rivers draining the northern flank of Anti-Atlas; **WAA**: rivers draining the western flank of Anti-Atlas; **SCAA**: rivers draining the southern flank of Anti-Atlas.

<sup>b</sup> Distance from divide.

<sup>c</sup> Distance from river mouth.

<sup>d</sup> Mean and standard error values.

<sup>e</sup> Standard deviation of the data.

<sup>f</sup> Channel steepness of selected river segments, by using a reference concavity of 0.45.

<sup>g</sup> Concavity value calculated by the slope of the line regressed through a log–log plot of channel slope vs. drainage area.

**Table S2.** Non-lithological knickpoint and river profile data from  $\chi$ -plot (data from Clementucci et al., 2022).

Stream <sup>a</sup>	Long.	Lat.	Elevation	DFD <sup>b</sup>	DFM <sup>c</sup>	Drainage area	Stream parameters			
							Downstream		Upstream	
	°W	°N	(m)	(m)	(m)	(m <sup>2</sup> )	$k_{sn}$ (m <sup>0.9</sup> ) <sup>f</sup>	$\theta$ <sup>g</sup>	$k_{sn}$ (m <sup>0.9</sup> )	$\theta$
NCAA1	637465.1	3379132.5	1731	20354	280487	1.58E+08	114.6 ± 0.2	0.42	15 ± 0.3	0
NCAA2	613556.8	3372613.8	1424	56831	257482	4.33E+08	118.5 ± 0.4	0.58	42.6 ± 0.78	0
NCAA3	608426.8	3354013.8	1565	23537	266134	1.42E+08	108.5 ± 0.4	0.43	35.5 ± 0.5	0.25
NCAA4	596666.8	3351313.8	1492	18508	257691	1.03E+08	111.5 ± 0.43	0.41	43 ± 0.4	0.3
NCAA5	589316.8	3345523.8	1529	11566	266423	2.64E+07	90.4 ± 0.5	0.28	30 ± 0.3	0.34
NCAA6	561056.8	3341233.8	1506	13041	185763	3.52E+07	102 ± 0.55	0.49	46 ± 0.7	0.2
NCAA7	555176.8	3340753.8	1324	16987	185931	4.73E+07	105 ± 0.42	0.35	63.7 ± 1	0.38
NCAA8	550076.8	3341713.8	1387	20427	187603	4.69E+07	103 ± 0.43	0.34	39 ± 0.9	-0.1
NCAA9	543836.8	3339913.8	1334	21396	162843	69549300	99.5 ± 0.47	0.56	45.2 ± 1.2	-0.18
NCAA10	525536.8	3328513.8	1175	24446	128875	80991900	136.8 ± 0.44	0.46	57 ± 0.56	0.27
Mean NCAA <sup>d</sup>							109 ± 3.9	0.43 ± 0.03	41.7 ± 4.2	0.15 ± 0.06
$\sigma^e$							12.6	0.09	13.5	0.19
WAA1	497197.4	3309532.6	1111	15696	137453	54819423	61.5 ± 0.2	0.6	37.5 ± 1.17	0.86
WAA2	443907.4	3255074.6	857	25669	106609	1.49E+08	72.16 ± 0.6	0.8	49 ± 1.1	0.1
WAA3	433249.4	3252884.6	849	29224	62967	1.11E+08	79.9 ± 0.4	0.63	35.3 ± 0.75	-0.1
WAA4	422883.4	3241277.6	854	11251	115444	12464531	62.7 ± 0.3	0.33	30.7 ± 0.43	0.02
WAA5	428504.4	3236605.6	1012	12228	128546	22472393	67.8 ± 0.37	0.39	20.24 ± 0.6	-0.18
WAA6	445513.4	3233028.6	982	14909	143614	29352132	66.2 ± 0.37	0.63	45.4 ± 3.44	-0.90
WAA7	471939.4	3246752.6	1272	10221	206751	30897542	66.86 ± 0.17	0.37	25.26 ± 0.85	-0.10
WAA8	482670.4	3251424.6	1294	11699	208687	33460791	68.8 ± 0.14	0.36	18.1 ± 0.47	0.08
WAA9	483765.4	3234050.6	971	43222	187564	2.55E+08	72.5 ± 0.21	0.42	33.6 ± 0.43	0.02
Mean WAA							68.7 ± 1.8	0.5 ± 0.05	32.7 ± 3.5	0 ± 0.14
$\sigma$							5.6	0.16	10.5	0.44
SCAA1	497927.4	3246825.6	1181	27564	430725	1.62E+08	82.56 ± 0.21	0.51	25.9 ± 0.57	0.76
SCAA2	520922.4	3281573.6	1628	14831	482538	39338678	79.58 ± 0.1	0.38	24 ± 0.38	0.04
SCAA4	-	-	-	-	-	-	-	-	-	-
SCAA5	549465.4	3322015.6	1580	12837	592340	32309727	86.4 ± 0.1	0.43	27.86 ± 0.23	0.47
SCAA6	564284.4	3324643.6	1448	17885	608379	1.51E+08	79.85 ± 0.26	0.52	49.15 ± 0.35	0.37
SCAA7	618961.4	3336542.6	1773	13358	685609	21443896	89.76 ± 0.67	0.63	15.7 ± 0.5	-0.03
SCAA8	636992.4	3343550.6	1476	22860	672273	86074008	70.85 ± 0.3	0.63	46.17 ± 0.6	0.20
Mean SCAA							81.5 ± 2.4	0.51 ± 0.03	31.4 ± 5	0.30 ± 0.1

$\sigma$	6.5	0.1	13.2	0.29
Mean tot	87.9 ± 4.07	0.47 ± 0.02	36.01 ± 2.5	0.12 ± 0.07
$\sigma$	20.35	0.12	12.3	0.34

<sup>a</sup> **NCAA**: rivers draining the northern flank of Anti-Atlas; **WAA**: rivers draining the western flank of Anti-Atlas; **SCAA**: rivers draining the southern flank of Anti-Atlas.

<sup>b</sup> Distance from divide.

<sup>c</sup> Distance from river mouth.

<sup>d</sup> Mean and standard error values.

<sup>e</sup> Standard deviation of the data.

<sup>f</sup> Channel steepness of selected river segments, by using a reference concavity of 0.45.

<sup>g</sup> Concavity value calculated by finding the value that minimizes the misfit to the linear relationship between  $\chi$  and elevation.

**Table S3.** Celerity model of non-lithological knickpoints in the NCAA, WAA and SCAA sectors.

Stream <sup>a</sup>	Elevation (m)	DFD <sup>b</sup> (m)	DFM <sup>c</sup> (m)	Drainage area (m <sup>2</sup> )	Model constrains						Model results						
					K		m		Time (Ma)		K	m	Time (Ma)		Model DFM <sup>d</sup>	Misfit	RMSE <sup>e</sup>
					Min	Max	Min	Max	Min	Max	Value	Value	Value	Error	(m)	(m)	
NCAA1	1731	20354	280487	1.58E+08	10 <sup>-7</sup>	10 <sup>-4</sup>	0	0.75	3.8	18.6	5.29E-05	0.66	10.1	4.2	280488	0,392	0.198
NCAA3	1565	23537	266134	1.42E+08	10 <sup>-7</sup>	10 <sup>-4</sup>	0	0.75	3.8	18.6	6.14E-05	0.69	9.9	4.4	266254	0,043	0.065
NCAA6	1506	13041	185763	3.52E+07	10 <sup>-7</sup>	10 <sup>-4</sup>	0	0.75	3.8	18.6	6.33E-05	0.69	9.8	4.3	185763	0,009	0.031
NCAA9	1334	21396	162843	6.95E+07	10 <sup>-7</sup>	10 <sup>-4</sup>	0	0.75	3.8	18.6	5.84E-05	0.69	10.7	4.3	163048	0,001	0.012
NCAA10	1175	24446	128875	8.10E+07	10 <sup>-7</sup>	10 <sup>-4</sup>	0	0.75	3.8	18.6	6.04E-05	0.67	9.3	4.1	129128	0,044	0.066
Mean											5.93E-05	0.68	9.9	4.3			
WAA1	1111	15696	137453	5.48E+07	10 <sup>-7</sup>	10 <sup>-4</sup>	0	0.75	3.8	18.6	5.91E-05	0.64	9.2	4.1	137453	0,026	0.051
WAA2	857	25669	106609	1.49E+08	10 <sup>-7</sup>	10 <sup>-4</sup>	0	0.75	3.8	18.6	5.22E-05	0.61	9.2	4.0	106609	0,190	0.138
WAA3	849	29224	62967	1.11E+08	10 <sup>-7</sup>	10 <sup>-4</sup>	0	0.75	3.8	18.6	5.48E-05	0.58	9.8	4.5	62967	0,082	0.090
WAA5	1012	12228	128546	2.25E+07	10 <sup>-7</sup>	10 <sup>-4</sup>	0	0.75	3.8	18.6	5.53E-05	0.65	9.1	3.9	128547	0,413	0.203
WAA7	1272	10221	206751	3.09E+07	10 <sup>-7</sup>	10 <sup>-4</sup>	0	0.75	3.8	18.6	5.34E-05	0.68	9.0	4.2	206752	0,348	0.186
Mean											5.50E-05	0.63	9.2	4.1			
SCAA1	1181	27564	430725	1.62E+08	10 <sup>-7</sup>	10 <sup>-4</sup>	0	0.75	3.8	18.6	5.47E-05	0.68	10.2	4.2	430725	0,166	0.128
SCAA2	1628	14831	482538	3.93E+07	10 <sup>-7</sup>	10 <sup>-4</sup>	0	0.75	3.8	18.6	6.69E-05	0.71	10.8	4.0	482538	0,136	0.116
SCAA4	1588	6291	485819	9.49E+06	10 <sup>-7</sup>	10 <sup>-4</sup>	0	0.75	3.8	18.6	7.00E-05	0.72	11.0	3.8	485819	0,005	0.022
SCAA5	1580	12837	592340	3.23E+07	10 <sup>-7</sup>	10 <sup>-4</sup>	0	0.75	3.8	18.6	6.63E-05	0.71	9.8	3.8	592340	0,216	0.147
SCAA6	1448	17885	608379	1.51E+08	10 <sup>-7</sup>	10 <sup>-4</sup>	0	0.75	3.8	18.6	6.42E-05	0.70	10.2	4.3	608379	0,119	0.109
Mean											6.44E-05	0.70	10.4	4.0			
Mean tot											5.96E-05	0.67	9.9	4.1			

<sup>a</sup> **NCAA**: rivers draining the northern flank of Anti-Atlas; **WAA**: rivers draining the western flank of Anti-Atlas; **SCAA**: rivers draining the southern flank of Anti-Atlas.

<sup>b</sup> Distance from divide.

<sup>c</sup> Distance from river mouth.

<sup>d</sup> Modelled distance from river mouth.

<sup>e</sup> **Root** mean square error.

**Table S4.** Reconstructed relict stream profile and 95% confidence interval.

Stream <sup>a</sup>	m/n	Drainage divide elevation <sup>b</sup>	Paleo-relief <sup>c</sup>	Elevation knickpoint	$\Delta Z$ <sup>d</sup>	Error (2 $\sigma$ )
		(m)	(m)	(m)	(m)	(m)
NCAA1	0.45	1900	738.2	1731	1161.8	18.3
NCAA2	0.45	1900	916.1	1424	983.9	22.3
NCAA3	0.45	1900	1047.1	1565	852.9	17.4
NCAA4	0.45	1900	782.7	1492	1117.3	8.4
NCAA5	0.45	1900	903.2	1529	996.8	11.1
NCAA6	0.45	1900	1055.1	1506	844.9	42.5
NCAA7	0.45	1900	1024.1	1324	875.9	28.3
NCAA8	0.45	1900	1139.8	1387	760.2	38.4
NCAA9	0.45	1900	1054.2	1334	845.8	29.1
NCAA11	0.45	1900	1077.4	1175	822.6	36.5
Mean <sup>e</sup>			973.8		926.2 $\pm$ 42.1	
$\sigma^f$					133.15	
WAA1	0.45	1400	879.5	1111	520.5	31.8
WAA3	0.45	1400	846.8	849	553.2	15.1
WAA4	0.45	1400	941.2	854	458.8	9.1
WAA5	0.45	1400	644.9	1012	755.1	15.7
WAA6	0.45	1400	760.1	982	639.9	13.9
WAA7	0.45	1400	527.9	1272	872.1	28.8
WAA9	0.45	1400	808.6	971	591.4	10.0
Mean			772.7		627.3 $\pm$ 54.1	
$\sigma$					143.17	
SCAA1	0.45	1900	1025.8	1181	874.2	5.9
SCAA2	0.45	1900	783.3	1628	1116.7	18.3
SCAA4	0.45	1900	1089.1	1588	810.9	117.7
SCAA6	0.45	1900	822.9	1448	1077.1	12.7
SCAA7	0.45	1900	824.3	1773	1075.7	58.4
SCAA8	0.45	1900	806.9	1476	1093.1	20.9
Mean			892		1008.0 $\pm$ 53.3	
$\sigma$					130.5	

<sup>a</sup> **NCAA**: rivers draining the northern flank of Anti-Atlas; **WAA**: rivers draining the western flank of Anti-Atlas. **SCAA**: rivers draining the southern flank of Anti-Atlas.

<sup>b</sup> Mean drainage divide elevation.

<sup>c</sup> Difference between mean drainage divide elevation and surface elevation ( $\Delta Z$ ).

<sup>d</sup> Estimated surface uplift from reconstructed relict stream profiles.

<sup>e</sup> Mean and standard error values.

<sup>f</sup> Standard deviation of the data.

**Table S5.** Maximum excavation time estimated from basin-wide denudation rates of Anti-Atlas watersheds in Clementucci et al. (2022).

Stream	Basin area <sup>a</sup>	Eroded material <sup>b</sup>	Ratio V/A <sup>c</sup>	Denudation rate <sup>d</sup> (m/Myr)		Excavation time <sup>e</sup> (Myr)	
ID	(km <sup>2</sup> )	(km <sup>3</sup> )	(km)	Value	Error	Value	Error
11	1200.6	148.1	0.12	7.53	0.51	16.37	0.64
10	480.1	58.6	0.12	8.10	0.55	15.07	0.59
12	842.7	117.4	0.14	12.46	0.95	11.18	0.50
9	1905.1	260.0	0.14	11.34	0.77	12.04	0.47
7	74.1	7.0	0.09	10.72	0.71	8.79	0.34
8	195.8	15.9	0.08	21.32	1.47	3.81	0.15
4	1828.1	314.7	0.17	9.25	0.65	18.61	0.76
3	558.3	56.0	0.10	5.78	0.39	17.36	0.68
5	1438.9	229.5	0.16	9.38	0.64	17.00	0.67

*Note.* <sup>a</sup> Basin area extracted from ArcGIS. <sup>b</sup> Estimated missing volume of eroded material between a smooth surface fitting the preserved summit and present-day topography (e.g., Siame et al., 2015). <sup>c</sup> Ratio between volume of eroded material and basin area. <sup>d</sup> Denudation rate from Clementucci, et al. 2022 (<sup>10</sup>Be - derived denudation rate). <sup>e</sup> Ratio between eroded material from river basin and denudation rate. The values are maximum time using the denudation relative only to the relict portion of the landscape, which providing quartz grains

## References

- Clementucci, R., Ballato, P., Siame, L. L., Faccenna, C., Yaaqoub, A., Essaifi, A., Leanni, L., & Guillou, V. (2022). Lithological control on topographic relief evolution in a slow tectonic setting (Anti-Atlas, Morocco). *Earth and Planetary Science Letters*, 596, 117788. <https://doi.org/10.1016/j.epsl.2022.117788>
- Siame, L. L., Sébrier, M., Bellier, O., Bourlès, D., Costa, C., Ahumada, E. A., Gardini C. E., & Cisneros, H. (2015). Active basement uplift of Sierra Pie de Palo (Northwestern Argentina): rates and inception from  $^{10}\text{Be}$  cosmogenic nuclide concentrations. *Tectonics*, 34(6), 1129-1153. <https://doi.org/10.1002/2014TC003771>